INTERACTIONS BETWEEN FLUID FLOW, HEAT TRANSFER, AND PARTICLE TRANSPORT IN THE PRESENCE OF JET-AXIS SWITCHING AND REALISTIC FLUID MOVERS

A DISSERTATION
SUBMITTED TO THE FACULTY OF
UNIVERSITY OF MINNESOTA
BY

John Michael Gorman

IN PARTIAL FULFILLMENT OF THE REQUIREMENTS
FOR THE DEGREE OF
DOCTOR OF PHILOSOPHY

Advisor
Professor Ephraim M. Sparrow

December 2014

Acknowledgements

To begin with, I would like to express my deepest gratitude towards Eph Sparrow, the most sagacious professor and engineer I have ever met. Because of him, I decided to continue furthering my education and it has been fun. It is also necessary to acknowledge another highly-exalted person, Professor John Abraham at the University of St. Thomas, for all of his support over the years.

Furthermore, it is necessary to thank the people working in MENET (ENET) for their non-technical support in making this whole experience much more entertaining (Hokan, Ray Muno, Paul Markfort). Along the same lines, I would like to thank Michael Reeves (Facilities Management) for his services and for the amusement he provided.

Moreover, I would like to thank my family for their support during this endeavor.

Dedication

This thesis is dedicated to the entire field of Mechanical Engineering.

Abstract

The overarching goal of this thesis is to identify and quantify new processes and phenomena related to fluid flow, heat transfer, and particle transport interacting in unique modes. The research can be categorized into three modes of interaction: (a) heat transfer processes governed by the complex patterns of fluid flow provided by real-world fluid-moving devices, (b) heat transfer processes which are governed by a naturally occurring, extraordinary fluid-flow phenomenon, and (c) interacting fluid flow, particle transport, and heat transfer all of which are governed by the aforementioned extraordinary fluid-flow phenomenon. These categories are respectively treated in individual chapters of the thesis.

The traditional approach to convective heat transfer is virtually devoid of realistic fluid flow models. As a consequence, traditional convective heat transfer analysis is oversimplified to the point of being out of step with reality. This assertion is proven here, and a new fundamentals-based model of high fidelity involving realistic fluid movers of is created.

Next, the extraordinary fluid flow phenomenon designated as jet-axis switching is introduced and illustrated quantitatively. This phenomenon occurs whenever a non-circular jet passes into and through an unrestricted space. When the jet is involved in a process called jet-impingement heat transfer, the zone of jet incidence is highly altered due to the axis-switching process. The ignoring of the switching process, which has been standard in all previous work on non-circular-jet impingement heat transfer, has been shown here to be highly error prone.

The major part of the thesis encompasses jet-axis-switching fluid mechanics, convective heat transfer, and particle transport. An all-encompassing simulation model was created which took account of fluid-particle, particle-particle, fluid—impingement plate, and particle—impingement plate interactions, all with heat transfer. It was found that jet-axis

switching exerted a major effect on the trajectories of the particles, with a corresponding impact on the particle collection efficiency of the impactor plate. The transfer of heat between the fluid and the impingement plate was little affected by any alterations in the pattern of fluid flow caused by the presence of particles. On the hand, direct particle-to-plate heat transfer is substantial.

Table of Contents

List of Tables

List of Figures

Chapter 1

INTRODUCTION

1.1 Overview

The overarching goals of this thesis research are twofold: (a) to identify incorrect traditional models and create new, logic-based models and (b) to free a recently recognized phenomenon from its narrow base and to implement its involvement in physical processes of broad diversity. Underlying all facets of the research is flow fluid and heat transfer, with particle transport also playing a significant role. These models and processes will now be amplified.

(a) Consideration will first be given here to identifying the erroneous models inherent in traditional heat transfer approaches and to creating alternative logic-based, first-principles methodologies. In long-enduring fields such as heat transfer, analysis approaches and solution methodologies were created in the distant past when experimentation and the concomitant instrumentation were relatively crude and understanding of the participating physical processes was primitive. For the most part, these practices have persisted to the present day by means of vehicles such textbooks which are only modestly different reproductions of past editions. The foregoing general characterizations require amplification by means of specific illustrations. Perhaps the most appropriate among these are well- known convective heat transfer applications where both misapplied fluid flow and thermal models have been joined to produce significant departures from reality.

These issues will be explored in depth and amplified in Chapter 2. The first issue to be addressed are practices related to the role of fluid mechanics in convective heat transfer research and practice. In that regard, it is relevant to recall that both axial fans and centrifugal blowers operate within the framework of fan and blower curves. Such curves relate the magnitudes of the two products of the fluid mover: the volumetric flowrate and the pressure rise. There is a large body of published convective heat transfer research in

which the flowrate (or velocity) is prescribed arbitrarily without regard to whether or not it is compatible with a realistic fan/blower curve.

When use is made of a fan/blower curve, it is very often without regard for the realities of how the exhibited information was obtained. As will demonstrated in detail in Chapter 2, the flow produced by an axial fan is by no means neither unidirectional nor uniform. In that state, determination of the volumetric flowrate cannot be implemented. Instead, the unruly flow is passed through an array of screens and/or homogenizers to create a measurable flow magnitude. It is that information which is used to construct published blower curved. If the fan in question were to be employed without an identical or equivalent flow transforming system, the information conveyed by the blower curve with be inappropriate.

Additional causes for error occur when a blower curve interpreted as providing a uniform and unidirectional flow is applied in an application where the inlet cross section of the device consists of a multitude of parallel passages. An example of such a situation is the array of flow passages that correspond to the inter-fin spaces in a longitudinal array of straight fins. If the exit face of an axial fan were to be placed in the plane of the inlets of the flow passages, and if identical flowrates were assumed to be delivered to each passage, a massive departure from reality would have been committed. In practice, blockages due to portions of the fan structure, swirl created by fluid rotation, cross-sectional non-uniformities, and back flow attributable to local low pressure zones all occur. As a consequence, any heat transfer results extracted from such a fluid mechanic model would have little practical relevance.

The improper use of fan/blower curves and the total neglect of pressure rise issues have major impacts in crucial applications such as in the thermal management of electronic equipment. Thermal management of such equipment is a dominate issue in the drive toward compaction that is of major importance for electronic-based devices. It remains an open

question, to be explored here, as to whether improper treatment of the fluid flow in heat exchanger devices gives rise to optimistic or pessimistic outcomes.

The common practice in current engineering design may be classified into two categories. One of these can be best characterized as Edisonian, so named to acknowledge the procedure used by Thomas Alva Edison to select the most appropriate filament for his invention of the electric light bulb. The selection process involved the world-wide collection of approximately 6,000 candidate filament media and the trial of each. By the same token, different geometrical arrangements and air-source locations are repetitively tried until a workable device is created. Once this has been achieved, it is rare that further steps are taken to increase the effectiveness of the device beyond that first judged to be satisfactory. The other common practice is to tweak an existing working arrangement to make small changes to accommodate a new application.

In this light, Chapter 2 of this thesis has accepted the goal of demonstrating the technical shortcomings of current practice in the design of contemporary heat transfer devices. That goal is the first step in the establishment of a new logic-based, first-principles modality for the attainment of excellence in the design of such devices.

Although these goals will be demonstrated to have been achieved in Chapter 2, the writer is concerned about whether the great weight of tradition and intellectual sluggishness will block the practical adaptation of the new ideas that are set forth here. Textbook writers appear to be a fraternity of copycats, freely borrowing from previous texts. Notwithstanding these barriers, the writer will encourage others to follow the lead that has been demonstrated here.

(b) Attention will now be directed to the substance of Chapters 3 and 4. Both of these chapters continue the theme of interactive heat transfer and fluid flow, and another physical process, the transport of solid particles by a flowing fluid, is incorporated into Chapter 4. The core novelty of Chapters 3 and 4 is a phenomenon designated as jet-axis switching.

That phenomenon is encountered when non-circular jets enter a free space downstream of the jet exit. As will be demonstrated in Chapter 4, a large-aspect-ratio slot jet with its long cross-sectional axis disposed horizontally will undergo a change of orientation as it proceeds downstream from the jet exit. At sufficient downstream distances, the initial rectangular cross-sectional shape of the jet is transformed to near circularity and subsequently is further transformed to a flat rectangular jet whose long axis is vertical.

The existence of such a phenomenon is documented in the literature but only in the context of highly erudite fluid mechanics, where the stated motivation is fluid mechanics for its own sake. No regard whatsoever is given to any engineering issues. For example, nowhere in the literature is a definitive sequence of the evolving cross-sectional shapes documented. Furthermore, all of the published literature is confined to jets passing into free spaces without impingement on other surfaces. In addition, no concern has been given to heat transfer nor particle transport.

Here, the multiple foci of the work are directed to impingement, to heat transfer, and to particle transport. All of these are of direct interest and relevance to present-day engineering applications. It is relevant to elucidate some of these applications. One is the high current interest in the creation of special coatings by the deposition of particles carried by gas jets.

An entire field, termed Rapid Expansion of Supercritical Solutions with the abbreviation RESS, is based on the impingement of particle-laden gas flows on target surfaces. The RESS process is widely used in the manufacture of well-known pharmaceuticals such as aspirin and ibuprofen among many others. Other applications of the RESS methodology produce specialty chemicals.

The RESS process is based on the dissolution of chemicals in the form of solid particles in a supercritical medium, with carbon dioxide being a favorite. The thus-produced homogeneous mixture is accelerated as it flows through a straight tube, and is purported to

reach the end of the tube in the sonic state. The tube exit is either open or partially blocked by a slotted orifice plate. The slot, if present, is commonly in the form of a high-aspect-ratio rectangle. After passing through the tube exit, the produced jet enters a large free space where a change of state occurs from the supercritical to the gaseous. Also occurring in the rapid expansion is a sequence of shocks of different strengths. These phenomena occur upstream of a target plate. The gas delivers the particles to the target where they are collected to form a hoped-for uniform coating.

A careful study of the RESS literature with particular focus on processes which incorporate slotted exit orifices failed to unearth any mention of the jet-axis-switching behavior.

A somewhat more immediate application of slotted orifices is encountered in the deposition of nanoparticles on target surfaces. Here again, there appears to be no recognition of the axis-switching phenomenon. Many other current applications utilize slot jets, but the writer has not encountered any mention of axis-switching in the relevant literature.

Particle sorting by size is commonly encountered by a sequence of surfaces called impactors. A particle-laden gas stream is conveyed through a sequence of flow passages along which the impaction surfaces are deployed. The cross sections of the flow passages may be of various shapes that are not necessarily circular. To achieve the desired impaction configuration, a free jet is created just upstream of each impactor surface. To achieve the free jet, the flow passage that delivers the particle-laden gas to the impactor in question is terminated at the inlet of a free space which is bounded below by the impactor. The thus-created free jet is able to change shape provided its cross section is non-circular. The jet-axis switching phenomenon has apparently not yet been recognized by investigators of particle technologies. It is expected that the results of the present investigation, to be reported in Chapter 4, will prove to be an impetus to future advances in particle size sorting.

It is universally recognized that the largest magnitudes of convective heat transfer coefficients are provided by jet impingement. Whereas the most common jet cross sections

used in heat transfer applications are circular, there is considerable used of slot jets as well. For example, in manufacturing processes based on the use of a continuous conveyor belt, heated air is provided by slot jets that span the entire width of the belt. Another example in a field that is highly contrasting with the foregoing, slot jets are standard equipment for the drying of potato chips. Both of these situations are examples of jet-based heat transfer. In neither application, no notice has been taken and possible advantage obtained from the recognition of the jet-axis switching phenomenon.

The foregoing discussion was intended to place the present research in the various contexts to which its outcomes are applicable. Now, attention will be turned to a brief outline of the contents of the thesis.

₪ ₪ ₪

1.2 Chapter 2 Insights

Chapter 2 is devoted to the issue of demonstrating the inappropriateness and error-proneness of numerous venerable approaches to heat transfer analysis and predictions. The methodologies in question were given birth in past eras where naiveté as to the nature of fluid flow and heat transfer was dominant. For example, there is considerable evidence of confusion about whether measured pipe-flow heat transfer coefficients should be regarded as average or fully developed value. In fact, neither fluid flow development nor the concomitant development of heat transfer in pipes was understood.

The main reason for the insufficient depth of understanding was the absence of means for probing the internal processes which governed convective heat transfer. The only instrumentation available at the time was limited to gross phenomenon. In parallel to the paucity of experimental-based information was the total absence of computational capability, aside from enhanced adding machines. It was in such an environment that analysis tools for heat transfer were first developed. It is remarkable that these tools are still in common use today.

Even the celebrated boundary layer of Prandtl, set forth in 1904, proved to be a drag on the physical understanding of fluid flow and heat transfer processes. The net outcome of the boundary layer theory was the dismissal of diffusion in the streamwise direction. When properly implemented, diffusion is a three-dimensional phenomenon. When the streamwise component is suppressed, downstream events can never affect upstream behavior of both fluid flow and heat transfer.

In light of the foregoing, there is ample motivation to expose the weaknesses of still-practiced venerable methodology. Such an exposition is part of the focus of Chapter 2. The breath of an all-facets exposure of the entirety of the insufficiencies would require dedication of the entire thesis to this issue. Since other issues are also of interest to the writer, two specific cases of practical importance were chosen for the exposition of the flawed methodologies. To replace those methodologies with others that truly represent the physical processes is the second focus of Chapter 2. Both of the selected cases are related to heat transfer enhancements that incorporate the use of fins, with particular attention to the thermal management of electronic equipment. This burgeoning field of activity is developing hand-in-hand with the electronics revolution that is now sweeping the world.

The new methodologies advanced here are based on models whose implementation is achieved by numerical simulation. Computer resources of sufficient capability are now widely available and should become even more so in the future. It is the belief of the writer that the developed methodologies will be readily incorporated into standard engineering practice.

₪ ₪ ₪

1.3 Chapter 3 Insights

Chapter 3 broadens the forefront fluid flow and heat transfer theme of the thesis by incorporating a recently uncovered, but insufficiently explored, phenomenon. That phenomenon is termed jet-axis switching. Whenever a jet of non-circular cross section expands from the jet exit into a large free space, the cross section undergoes a change of

shape. The published literature on jet-axis switching is completely dedicated to theoretical fluid mechanics as is carefully noted in the introductory material in the papers themselves. This declaration of highly focused interest has, in effect, placed blinders on those who have contributed to this area of research activity. Furthermore, the phenomena that are spawned by jet impingement on solid surfaces have been completely eschewed. In total contrast to the just-described attitude of anti-practice erudition, the attitude adopted here is to focus on the engineering realities and impacts of this phenomenon.

In Chapter 3, the major focus is on the distortion of impinging jets by the jet-axis switching phenomenon. In particular, an exhaustive investigation is made of the variables that control the magnitude and the rapidity of the onset of the process. Once these variables are established, they are parametrically varied with a view to discovering how the process can be controlled as a means of augmenting heat transfer. There is a concerted current activity to discover new means of heat transfer augmentation that depart from the heavy-handed approaches of the past. From this standpoint, the control of the jet-axis switching offers a fertile new concept.

In addition to the thorough quantification of the heat transfer response to jet-axis switching, the resulting shape variations of free non-circular jets is documented for the first time since all prior published work has been occupied with minutia.

₪ ₪ ₪

1.4 Chapter 4 Insights

The focus of Chapter 4 brings into play the interaction of jet-axis switching with particles being transported by means of particle-laden gas flows. The combined impacts of the switching and the presence of particles on jet-impingement heat transfer is another focus of this chapter.

Particle transport is broadly encountered in the entire range of human and natural activities. Despite this truism, it appears that no previous work has been done on the effect of the

switching phenomenon on the trajectories of gas-transported particles. Here, several features of this interaction are explored, both for particle trajectories in free space as well as on the impingement sites of particles on surfaces. A special feature of the investigation is to probe the combined effects of gravity and axis switching, both for free space particle motion and impingement patterns.

There are several types of interactions that may occur whenever fluids and particles are in proximity and in motion. Two types of fluid-particle interactions are considered here: one-way and two-way. In the case of one-way interactions, the fluid forces are allowed to modify particle motions but the presence of the particles does not affect fluid motion. For two-way interactions, both media mutually affect each other. Another natural type of interaction are those between particles. When particle-particle interactions are facilitated, two-way fluid-particle interactions occur simultaneously.

The modeled flow was vertically downward, thereby permitting gravity to play a role. For all the cases when gravity was activated, all of the aforementioned interactions occurred.

Special consideration was given to the pattern of particle impingement on a flat plate positioned normal to the nominal streamwise direction. This focus was motivated by the well-known method of inertial-impactor particle size sorting. As previously described, particle sorting is accomplished by the use of jet-like, particle-laden gas flows impinging on flat plates. The collection efficiency of the impactor-like plates was evaluated taking account of jet-axis switching.

A careful diagnostic approach was followed in assessing the response of the heat transfer at the impingement plate to the various phenomena discussed in the preceding paragraphs. In one of the selected scenarios, the heat transfer response to the disturbance of the fluid flow due to fluid-particle interactions, particle-particle interactions, and gravity was determined. In that scenario, direct heat transfer between the particles and the impingement

surface was purposely excluded. In a second scenario, the phenomena inherent to the first scenario were included, but direct particle-to-surface heat transfer was taken into account.

Another thermal interaction that was investigated was the convective heat transfer between the particles and the fluid. The results conveyed in the form of Nusselt numbers can be utilized for mass transfer analyses by transforming the Nusselt numbers to Sherwood numbers and matching the values of the Prandtl and Schmidt numbers. In particular, the nature of the fluid flow in the presence of particles that was investigated in Chapter 4 can be regarded as a model of a fluidized bed.

Chapter 2

FLUID FLOW AND HEAT TRANSFER PHENOMENA IN THE PRESENCE OF AXIAL FANS

2.1 INTRODUCTION

As with any long-established discipline, heat transfer analysis and design suffers from a plethora of misconceptions and over simplifications that have been codified by frequent use and by their propagation in textbooks. The acceptance of these erroneous approaches has led to predictions of heat- transfer-device performance that are far from reality. In this chapter, irrefutable evidence of this situation is presented.

As an example of the textbook propagation syndrome of erroneous concepts, the case of fin heat transfer is appropriate. In particular, it may be noted that the same fin model is set forth in the voluminous Heat Transfer Notes authored by the Berkeley Heat Transfer Group in 1942 and in the 2015 edition of the Cengel and Ghajar textbook, Heat and Mass Transfer. The Berkeley notes set forth the total knowledge of heat transfer existent at the time. The Cengel and Ghajar heat transfer textbooks are the most used in the United States.

Among the oversimplifications that are contained in the standard textbook fin model, the one that is highly relevant to the present research is the total neglect of the way that a coolant fluid is delivered to the inlet of the fin array. In fact, the nature of the delivered coolant fluid is treated as a non-issue. The overwhelming majority of fin-related papers that have appeared in the published literature since time immemorial have followed the pattern of avoidance of the means of coolant fluid delivery by imposing a uniform flow at the inlet of the fin array. Many of the textbook simplifications have persisted as well.

The research plan for the chapter is built on the selection of real-world heat transfer devices whose proper design is critical to effective thermal management. In particular, the two devices selected for study both include extended surfaces (fins) because (a) such devices

suffer from extremely erroneous modeling and (b) such devices are used extremely frequently in practice in connection with critical applications.

The approach used here is to subject each of the chosen devices to two modalities of analysis: (a) performance predictions using the best of the traditional approaches and (b) performance predictions based on impeccably valid physical models implemented by numerical simulation. For modality (a), the use of the most-used rather than the best of the traditional approaches would have not been honest with respect to the aims of this research.

2.2 BACKGROUND

The focus of this portion of the chapter is to describe in some detail the methodologies that are and have been practiced in heat exchanger design. In this context, the heat exchangers of relevance are those of moderate size which are employed in the thermal management of specific equipment of modest dimensions, such as electronic equipment. As noted in the foregoing, it is common practice to use extended surfaces as a means of enhancing the compactness and efficiency of such management approaches.

The presently standard methodology in the quantification of heat transfer capability in the context of heat exchangers is characterized by an arm's-length approach. In particular, the overwhelming majority of the papers in the relevant literature has primarily stemmed from academicians who have had limited interactions with actual real-world heat transfer device experience. In this light, it can be understood that little or no attention was paid to the means by which the participating fluid flow was created. In [1], it was assumed that the flow entering the fin array was the fully developed laminar parabolic profile, where as in [2], the fluid flow within the array was taken to be fully developed and unchanging along the streamwise direction. Although an advanced optimization theory was used to optimize fin geometries in [3, 4], the velocity profile at inlet was arbitrary chosen to be uniform. The tendency to focus on novel fin geometries and ignore the nature of the flow delivered to the array is found in several publications, for example [5-8]. To altogether avoid the issue

of the inlet velocity profile, a periodic fully developed fluid-flow model was adopted for the flow passages in a fin array [9]. The issue of how fluid was delivered to a fin array was mute in the analysis described in [10].

Even more astonishing, the analysis of [11, 12] assumed an arbitrary swirl component appended to a uniform axial velocity as a means of describing the flow provided by a muffin fan. The postulated swirl components were of different magnitudes in the two referenced papers. Experiments described in [13-15] utilized a muffin fan to deliver flow to the fin-array inlet, but the nature of the thus-provided flow was not understood. In the experiments of [16], fluid was delivered to the fin-array inlet by means of a duct, but the actual inlet velocity profile was not measured. The experimental work reported in [17, 18], the fin array was situated in a wind tunnel. In the former, the cross section of the tunnel was larger than the cross section of the array, thereby allowing the fluid to bypass the fins. In recognition of the irregular nature of the fluid flow provided by an axial fan, partial blockages were used to breakup vortices [19]. Almost without exception, no effort was made to relate the rate of fluid flow with the pressure drop by means of the capabilities of actual fluid movers except in [20, 21]. The absence of any attempt to connect the pressure drop and flow rate relevant to a particular heat exchanger can be regarded as an impractical approach.

Although the analytical approaches cited in the foregoing literature search are the most common encountered, they are by no means the best among the traditional methods. A seemingly superior approach is to make use of a blower curve [22, 23], a typical representation of which is illustrated in Fig. 2.1. The graph conveyed in that figure displays the pressure rise affected by the fluid mover as a function of the fluid flowrate that is produced. Note that the highest pressure rise achievable corresponds to the no-flow condition. The counterpart maximum flowrate condition is achieved when there is no pressure rise. Individual fluid movers display various departures from the relatively ideal shape set forth in the figure. In particular, a saddle is a common feature.

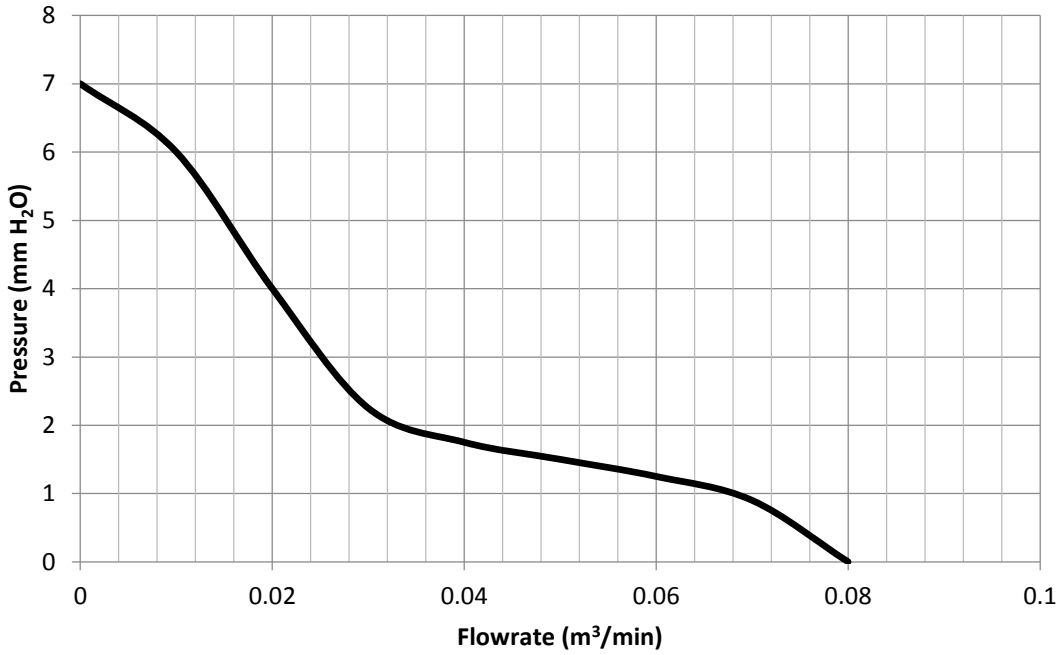

Fig. 2.1. Typical representation of a small axial-fan blower curve.

Blower curves are a product of experimentation. However, it is necessary to recognize the conditions under which such curves are obtained. In this context, it is convenient to focus specifically on various blower types. For axial fans/blowers, the flow exiting the fluid mover possess a strong swirl as well as zones of backflow embedded in the expected forward flow. It is extremely difficult to determine the true mass flowrate under such conditions. As a consequence, it is standard practice to condition the flow downstream of the exit of the fluid mover by means of homogenizers such as screens and perforated plates. The number of such homogenizers is not standardized. Furthermore, the homogenization of the flow is necessarily connected with a pressure drop. The flowrate that appears on the horizontal axis of a blower curve for an axial fan/blower is that measured for the homogenized state.

On the other hand, when axial fans are used in practice, it is uncommon to make use of homogenizers. Instead, the flow that leaves the exit plane of the fluid mover is used in its natural state. The dichotomy between the flow represented by the blower curve and that

used in practice casts a shadow over the use of a blower curve for analysis of a heat exchanger that utilizes such blowers.

Notwithstanding the foregoing reservations, the use of a blower curve for the analysis of heat transfer performance is a somewhat common procedure as an alternative to the arbitrary assignment of mass flowrates that is the most common approach to heat exchanger design. When a blower curve is used as a design tool, its fluid flow output is usually regarded as spatially uniform. This model is at great variance with respect to reality and, as demonstrated shortly, gives rise to significant errors in the predicted performance of heat exchangers.

2.3 PLAN OF RESEARCH

Two frequently encountered heat exchanger situations were selected for study here: (a) a pin-fin array thermally managed by air passing into the array through a plane encompassing the tips of the fins and (b) a longitudinal array of straight fins whose air flow is provided by a fluid source at its upstream end. Schematic diagrams of these physical situations are conveyed in Figs. 2.2 and 2.3 respectively.

In the first of these figures, a small axial fan, commonly designated as a *muffin fan*, is positioned in intimate contact with the plane of the tips of the fins. The fan will be modeled realistically in that the blades rotate at the actual RPM and the produced fluid flow corresponds to reality. The modeled fan also possesses a traditional blower curve. For contrast with the results corresponding to the aforementioned actual fan-driven fluid flow analysis, a separate analysis will be made using the blower curve. The model for the latter analysis envisions the blower as being removed. Instead, a uniform airflow governed by the characteristics of the blower curve is imposed. The heat source which is to be thermally managed consists of electronic components in intimate contact with the backside of the fin base.

Figure 2.3 shows an array of straight longitudinal fins whose tips define a plane on which a shroud is overlaid. In practice, shrouded fin arrays are used whenever possible to bound the flow channels defined by the interfin spaces.

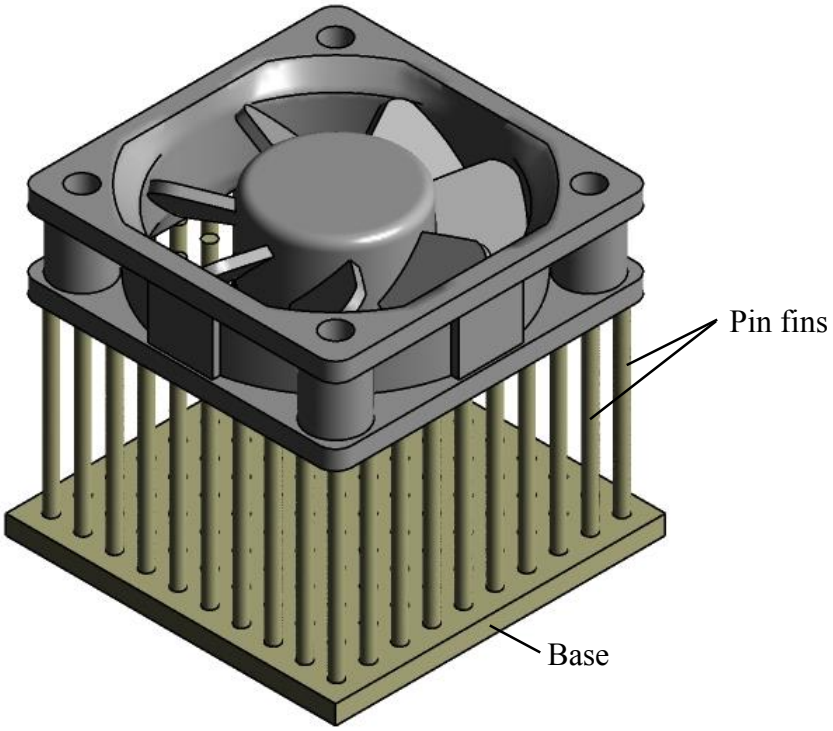

Fig. 2.2. A pin-fin array cooled by a muffin fan whose exit cross section lies in the plane of the fin tips. Electronic components are attached to the backside of the fin base but are not visible in the figure. The figure also serves as a model for a heat transfer analysis based on the characteristics of a blower curve. For that analysis, the physical blower displayed in the figure is replaced by a uniform flow.

As seen in the figure, airflow is provided to the fin array by suitably sized muffin fans deployed along the inlet face of the array. The size of each muffin fan is selected so that its vertical dimension is equal to the fin height. Since muffin fans present a square planform, the width of the array serviced by the fan is thereby fixed. The figure shows a physical situation where three muffin fans are deployed across the inlet face of the array. In practice, there is commonly a larger number of fans to service the selected width of the array.

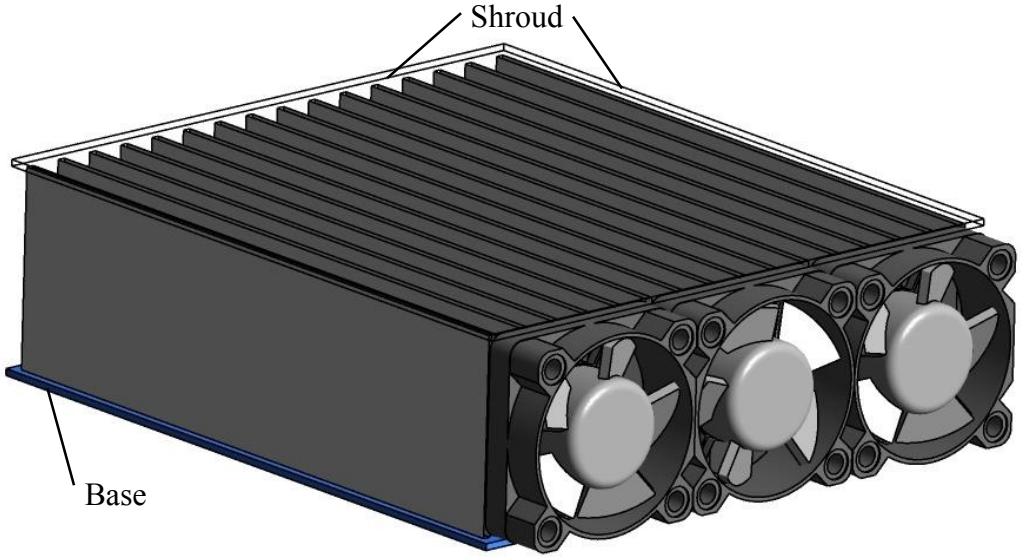

Fig. 2.3. A shrouded straight-fin array cooled by muffin fans that deliver air to the inlet cross section of the array. The figure also serves as a model for a heat transfer analysis based on the characteristics of a blower curve. For that analysis, the physical blowers displayed in the figure are replaced by a uniform flow.

The ingredients of the research plan are as follows:

(a) For each of the selected heat exchangers, an assumption-free heat transfer analysis based on fluid flow delivered by the actual fan rotation will be performed and relevant results extracted.

(b) In the case of the pin-fin array, two fin heights are considered to achieve a close coincidence with reality.

(c) For each of the considered heat exchangers, a system curve is created and note is taken of the crossing of that curve with the blower curve. That crossing defines the operating point.

(d) With the use of the fluid flow magnitude at the operating point of the blower curve, it is assumed, in concert with the traditional approach, that the air flow delivered to the selected heat exchangers is uniform.

(e) Consideration was given to a variety of thermal boundary conditions.

    a. The limiting case of isothermal fins

    b. The realistic case of heat conducting fins

2.4 NUMERICAL SIMULATION

In all of the considered physical situations, the fluid flow is three-dimensional and turbulent. The fluid flow produced by the rotating fan blades is highly complex and truly unsteady. Therefore, an unsteady model was adopted for the solutions. The three-dimensional unsteady model was also used for cases where the delivered flow is based on a blower curve. To resolve the enormous complexity of the flow field, the numerical simulation is performed with as many as 15 million nodes. To accomplish the totality of the numerical simulations, about nine months of real time was required.

The simulation software is ANSYS CFX 14.0. This software is based on discretization by means of the finite-volume method. The choice of a turbulence model was made on the basis of several years' experience with the modeling of highly complex fluid flow situations validated in many cases by experimental data. The chosen model is the Shear Stress Transport turbulence model. A major feature of this model is its hybrid nature. It bring together the venerable κ-ε model and the relatively newer κ-ω model. The former has been demonstrated to give rise to accurate results away bounding surfaces whereas the latter has been shown to be high effected in the near neighborhood of the bounding surfaces. The quantity κ is the turbulence kinetic energy, ω is the specific rate of turbulence dissipation, and ε is rate of dissipation.

A necessary part of any investigation based on numerical simulation is a demonstration of mesh independence. Although the literature favors comparisons of results corresponding to different numbers of nodes, it is the view of the writer that this is a shallow point of view. Of equal or greater importance is the deployment of the nodes. Here, both numbers and deployment were used to investigate mesh independence. Inasmuch as nodal deployment is difficult to quantify in simple terms, the mesh independence achieved by means of node numbers. In particular, the rate of heat transfer was used as the metric to judge mesh independence. For cases selected for mesh independence study, it was found

that increasing the node number from 11.5 million to 14.5 million nodes gave rise to variations of the heat transfer rate no greater than 0.2%.

The relevant physical principles that govern the flow and heat transfer are: momentum conservation (Reynolds Average Navier-Stokes equations), mass conservation, and the First Law of Thermodynamics. These equations are written for incompressible, constant property flow.

The RANS equations, as written in Cartesian tensor form, are

$$\rho\left(u_i\frac{\partial u_j}{\partial x_i}\right) = -\frac{\partial p}{\partial x_j} + \frac{\partial}{\partial x_i}\left((\mu + \mu_{turb})\frac{\partial u_j}{\partial x_i}\right) \quad i = 1,2,3 \;\; j = 1,2,3 \tag{2.1}$$

and the mass conservation equation is

$$\frac{\partial u_i}{\partial x_i} = 0 \tag{2.2}$$

The quantity μ_{turb} is designated as the turbulent viscosity. For the RANS model, it is defined as

$$\mu_{turb} = \rho\overline{u_i' u_j'} \tag{2.3}$$

Where the u_i' represent the fluctuating component of u_i.

The equations of the SST model are

$$\frac{\partial(\rho u_i \kappa)}{\partial x_i} = P_\kappa - \beta_1\rho\kappa\omega + \frac{\partial}{\partial x_i}\left[\left(\mu + \frac{\mu_{turb}}{\sigma_\kappa}\right)\frac{\partial \kappa}{\partial x_i}\right] \tag{2.4}$$

$$\frac{\partial(\rho u_i \omega)}{\partial x_i} = A\rho S^2 - \beta_2 \rho \omega^2 + \frac{\partial}{\partial x_i}\left[\left(\mu + \frac{\mu_{turb}}{\sigma_\omega}\right)\frac{\partial \omega}{\partial x_i}\right] + 2\rho(1 - F_1)\frac{1}{\sigma_{\omega 2}\omega}\frac{\partial \kappa}{\partial x_i}\frac{\partial \omega}{\partial x_i} \quad (2.5)$$

The solution of Eqs. (2.4) and (2.5) yields the values of κ and ω, which give the turbulent viscosity μ_{turb} from

$$\mu_{turb} = \frac{\alpha\rho\kappa}{\max(\alpha\omega, SF_2)} \quad (2.6)$$

A more thorough review of these equations can be found in [24].

The symbols that appear in the foregoing equations are defined as

A	model constant
F_1, F_2	blending functions in the SST model
P_k	production term for the turbulent kinetic energy
S	absolute value of the shear strain rate
u	local velocity
x_i	tensor coordinate direction
α	SST model constant
β_1, β_2	SST model constants
ω	specific rate of turbulence dissipation
μ	molecular viscosity
μ_{turb}	turbulent viscosity
σ	diffusion coefficient
ρ	fluid density

The heat transfer problem is governed by the First Law of Thermodynamics. For incompressible, constant property flow, the First Law can be written as

$$\rho c_p \frac{\partial(u_i T)}{\partial x_i} = \frac{\partial}{\partial x_i}\left[(k + k_{turb})\frac{\partial T}{\partial x_i}\right] \quad (2.7)$$

in which T is the temperature and c_p and k are, respectively, the specific heat and thermal conductivity. The quantity k_{turb} is designated as the turbulent thermal conductivity. Its value is closely linked to that of the turbulent viscosity by means of the turbulent Prandtl number

$$Pr_{turb} = \frac{c_p \mu_{turb}}{k_{turb}} \tag{2.8}$$

Extensive experience has shown that a constant value of $Pr_{turb} = 0.9$ gives rise to highly accurate heat transfer results.

2.5 FLOW FIELD PRODUCED BY AN AXIAL FAN OPERATING IN FREE AIR

The flow field that is produced by an axial fan is of interest in its own right in addition to the interactions of that flow field with the geometry of downstream devices. It is for this reason that the first part of the presentation of the results is focused on the fan operating in a fully open environment without other obstructing devices. Figure 2.4 illustrates the nature of the fluid motion produced by a muffin fan by means of a vector diagram. It is relevant to note that the lengths of the vectors have been normalized to be identical so that the common connection between vector length and velocity magnitude does not apply to Fig. 2.4. That connection will be demonstrated shortly. The view displayed in the figure lies in a vertical plane that is cut through the axis of rotation.

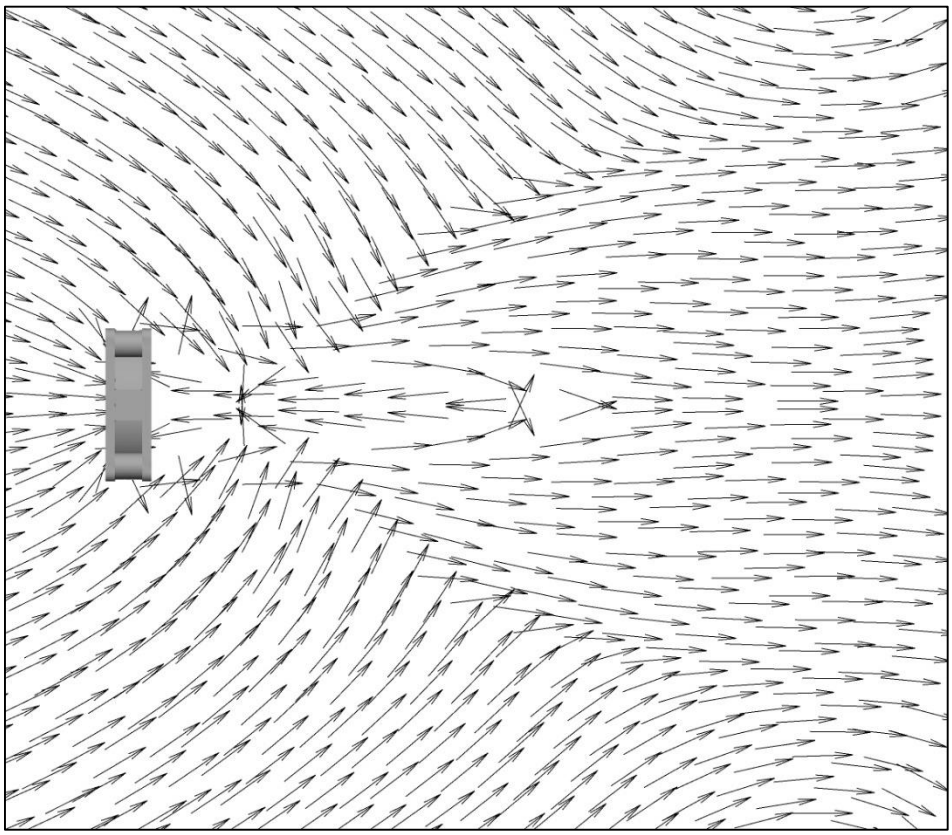

Fig. 2.4. Flow field depiction by means of vectors showing the directions of flow. The lengths of the vectors have been normalized to a single common value. The displayed view lies in a vertical plane cut through the axis of the fan.

One of the noteworthy features seen in the figure is the regions of backflow just downstream of the exit cross section of the fan. The backflow is caused by the tornado effect. It is well known that at the core of a rotating tornado-flow, the pressure may be much lower than that of the distance ambient. That low pressure works to induce flow toward it. The backflow which envelopes the axis is induced by this pressure depression. Another noteworthy feature is the inflow of the sheath of ambient fluid which surrounds the core of the fan driven flow. That inflow is also caused by the low pressure that exists in the core. Downstream of the termination of the backflow core, the flow exhibits a tendency to develop a more structured distribution characterized by straight parallel vectors. With further downstream distances, the structured region widens.

The flow upstream of the fan is drawn from a region that is considerably wider than the fan proper. The flow accelerates as it enters the inlet face of the fan. A portion of that acceleration can be attributed to the rotation of the hub. The fluid impinging on the hub is endowed with a strong swirl that is created by the no-slip boundary condition at the hub's surface. The strong swirl induces a low pressure which tends to invite upstream fluid toward it.

Another rendering of the information displayed in Fig. 2.4 is exhibited Fig. 2.5. The difference between the two figures is that the first shows vectors that are of the same length, as explained in the foregoing, while the vectors in the second figure have lengths that are keyed to their respective magnitudes. Inspection of the latter figure shows that small velocity magnitudes occur in the downstream core flow and in the fluid envelope that wraps around the main forward flow.

Another approach to the presentation of the velocity magnitudes is a color contour diagram, Fig. 2.6, in which the respective colors are keyed to a color strip at the left of the figure. It is clear from the figure that the highest velocities occur both upstream and downstream of the rotating blades. The zones of negative velocity are also clearly exhibited.

The pressure distribution corresponding to the velocity magnitudes of Fig. 2.6 are shown in Fig. 2.7. Not unexpectedly, negative pressures are encountered in the portion of the solution domain where fan-based fluid rotation exists. As explained previously, fluid rotation gives rise to the tornado effect and to the low pressures corresponding thereto.

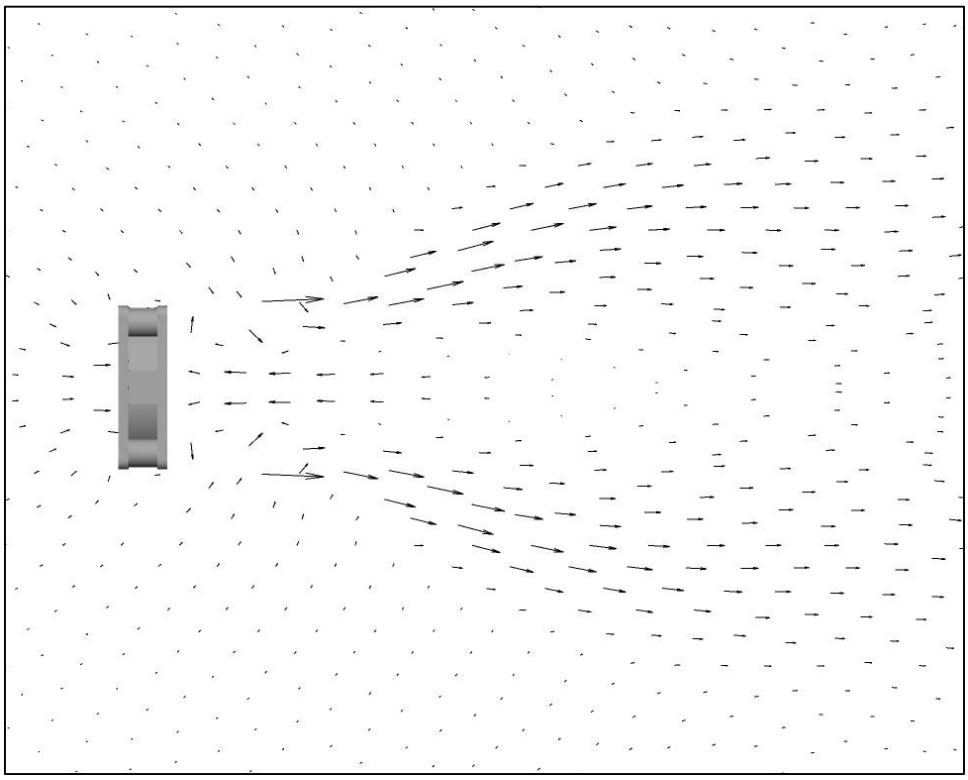

Fig. 2.5. Flow field depiction by means of vectors showing the directions of flow. The lengths of the displayed vectors correspond to the velocity magnitude at the location of the vector. The displayed view lies in a vertical plane cut through the axis of the fan.

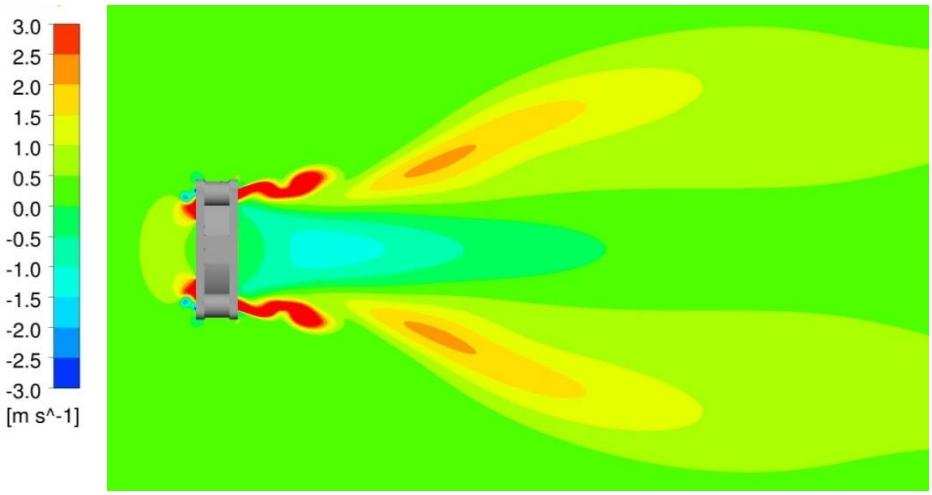

Fig. 2.6. Color contour diagram showing the velocity magnitudes.

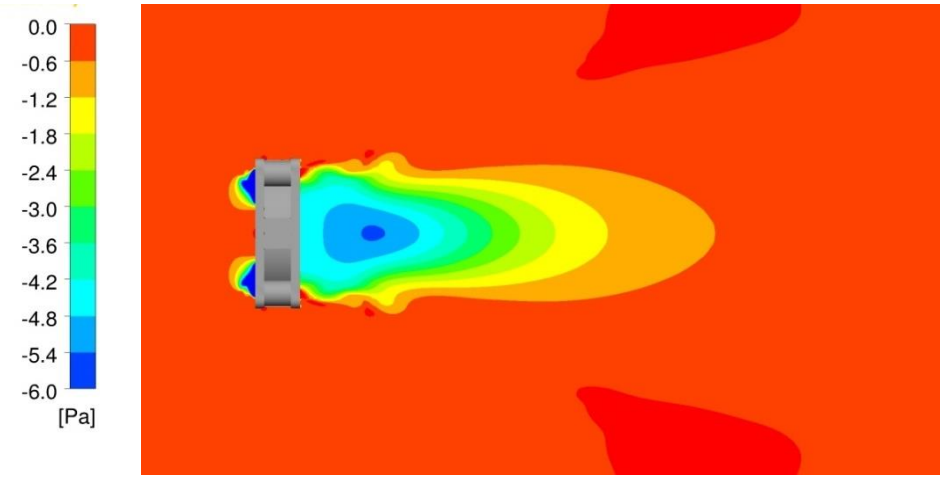

Fig. 2.7. Pressure field engendered by the fan-based velocity distribution.

The lowest pressures are encountered just upstream of the fan proper where the flow is accelerating and from the rotating hub causing strong swirl.

The preceding figures featured longitudinal cuts. Focus is now shifted to a succession of planes that are parallel to the fan exit. The first of these figures is Fig. 2.8, which shows velocity distributions in color contour form at four such planes downstream of the exit cross section. The series of disks chronicles an evolution of the magnitude of the velocity from highly dispersed to axisymmetric.

The information conveyed in Fig. 2.8 is elucidated in Figs. 2.9 to 2.13. Each of these figures is a color contour diagram with vectors superimposed in a plane situated at a selected distance downstream of the fan exit. The first of these figures, Fig. 2.9, corresponds to the exit plane itself. The colors displayed in the figure are keyed to the velocities perpendicular to the exhibited plane, while the vectors lie in the plane and are normalized to convey the direction of the in-plane velocity directions. The square region outlined in the figure is the approximate projection of the frame of the fan.

The forward flow is described by the outer interrupted ring situated in the annular space occupied by the rotating blades. On the contrary, the nearby internal ring depicts a strong

backflow which can be attributed to the tornado effect. The vector diagrams indicate an inflow toward the fan, thereby corroborating the information exhibited in Fig. 2.4.

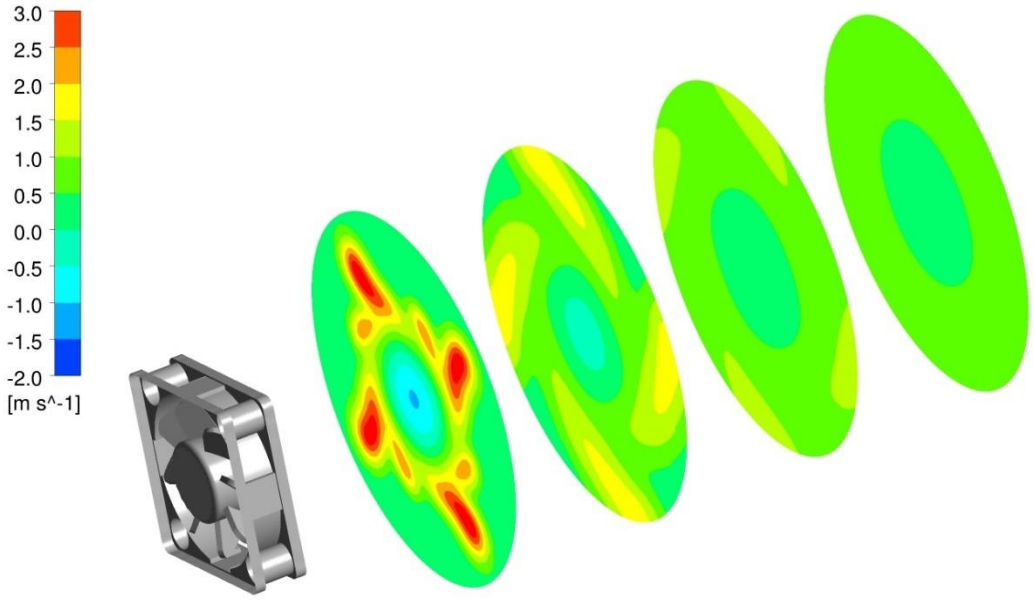

Fig. 2.8. Contour diagrams of the velocity magnitude in a succession of planes that are parallel to the exit cross section of the fan. The displayed view is an instantaneous snapshot of the flow.

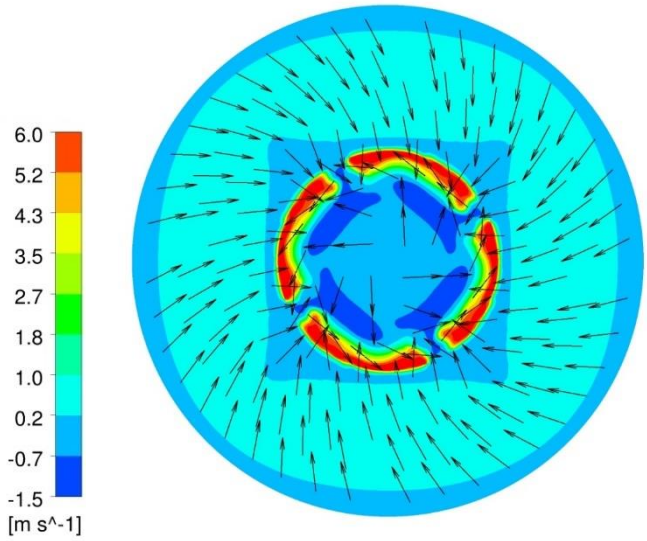

Fig. 2.9. Velocities in a plane parallel to and superimposed on the exit plane of the fan. The vectors show the flow direction in the plane while the colors indicate the magnitudes of the velocities perpendicular to the plane.

Focus is now directed to the next figure, Fig. 2.10, in the sequence. That figure is situated a distance of two centimeters downstream of the exit plane of the fan. There are some noteworthy differences that can be identified when comparing Figs. 2.9 and 2.10. With increasing downstream distance, the region of rotation expands radially, and the high velocity forward flow displays the same trend. The inflow region is forced outward, while the low pressure core is enlarged.

The trends identified in Fig. 2.10 are continued as the plane of observation moves farther downstream from the exit to a distance of four centimeters. As seen in Fig. 2.11, the zone of rotation further expands radially, and the highest forward flow velocities also move outward. However, the magnitude of the forward flow velocities clearly diminishes. The low pressure core contracts as friction works to decrease the rotational velocity.

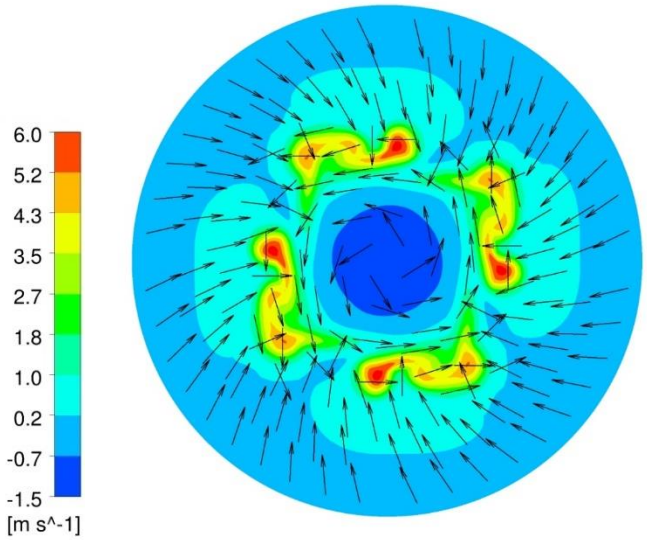

Fig. 2.10. Velocities in a plane parallel to the exit plane of the fan that is displaced two centimeters downstream from it. The vectors show the flow direction in the plane while the colors indicate the magnitudes of the velocities perpendicular to the plane.

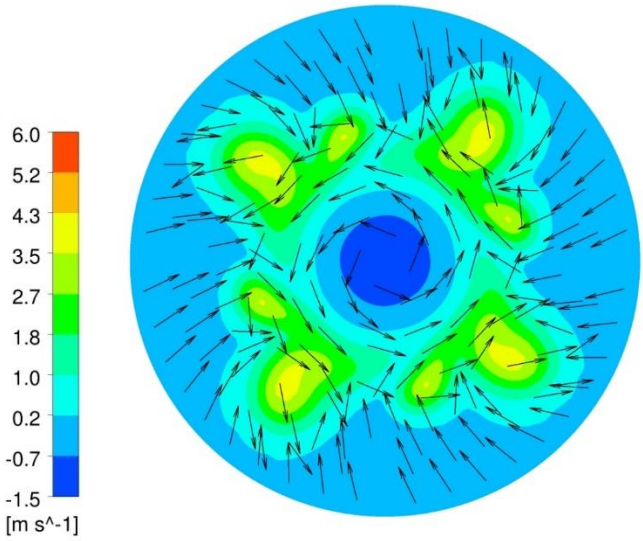

Fig. 2.11. Velocities in a plane parallel to the exit plane of the fan that is displaced four centimeters downstream from it. The vectors show the flow direction in the plane while the colors indicate the magnitudes of the velocities perpendicular to the plane.

In Fig. 2.12, which corresponds to a plane situated six centimeters downstream of the fan exit, the most noteworthy feature is the accelerated reduction of the forward flow velocities and the continuing weakening of the low-pressure core. At eight centimeters, Fig. 2.13, the forward flow further diminishes in magnitude and the pressures in the core are barely negative, corresponding to the near cessation of rotation.

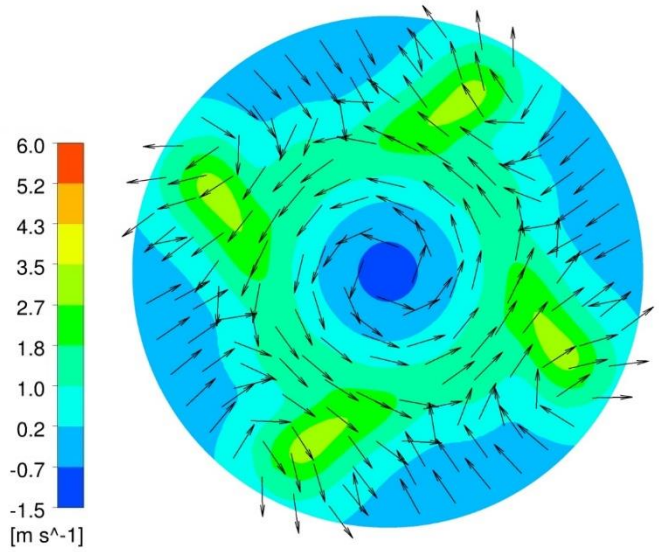

Fig. 2.12. Velocities in a plane parallel to the exit plane of the fan that is displaced six centimeters downstream from it. The vectors show the flow direction in the plane while the colors indicate the magnitudes of the velocities perpendicular to the plane.

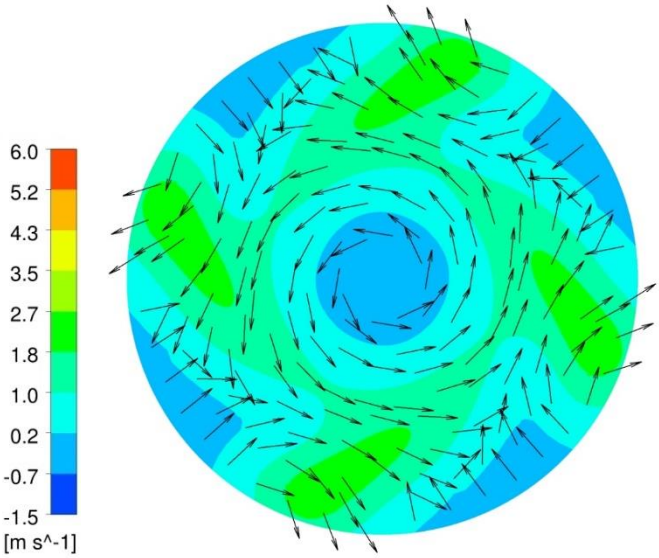

Fig. 2.13. Velocities in a plane parallel to the exit plane of the fan that is displaced eight centimeters downstream from it. The vectors show the flow direction in the plane while the colors indicate the magnitudes of the velocities perpendicular to the plane.

2.6 FLOW FIELD PRODUCED BY AN AXIAL FAN INTERACTING WITH A PIN-FIN ARRAY

When an axial fan interacts with a flow resistance such as a pin-fin array, the resulting flow field has a drastically different characteristic from that when the fan is operating in free air. As was described earlier, the interaction of the fan with the pin-fin array will be analyzed for two distinct situations: (a) the actual fan with rotating blades blowing into the array and (b) a uniform flow corresponding to the blower curve of the fan in question. The latter situation requires a preliminary numerical simulation to determine the operating point on the blower curve corresponding to the flow resistance of the array.

The specific muffin fan used for the investigation was chosen on the basis of its capability to deliver the flow rate and pressure rise suitable for the application. The chosen fan is d5015, which has an external frame of dimensions of 50 × 50 mm. For the fin dimensions listed in Table 2.1, the height and width of the fan subtended 676 pin fins.

Table 2.1. Dimensions of the pin-fin array and related information

Component	**Dimension**
Fin diameter	0.5 mm
Center-to-center distance	2.2 mm
Fin height	15 or 25 mm
Base width and height	56 mm
Base thickness	0 mm

To initiate the determination of the operating point, the first step is to display the blower curve. The relevant blower curve for the fan in question is exhibited in Fig. 2.14 as a solid line. The other curves in the figure, shown as dashed lines, represent pressure drops experienced by uniform flows passing into the fin array at the plane of the fin tips. The two such lines, designated as system curves, correspond to the two different fin heights. Each line was obtained by imposing a sequence of uniform volumetric flow rates and determining the resulting pressure drops. The intersections of the system curves with the blower curve are the operating conditions for the respective fin heights. It is noteworthy

that the array composed of taller fins gives rise to a smaller pressure than does an array of shorter fins. This outcome can be attributed to the greater outleakage available when longer fins are used. The operating points for the two distinct arrays favor the taller-fin array, 0.48 vs. 0.39 m^3/min.

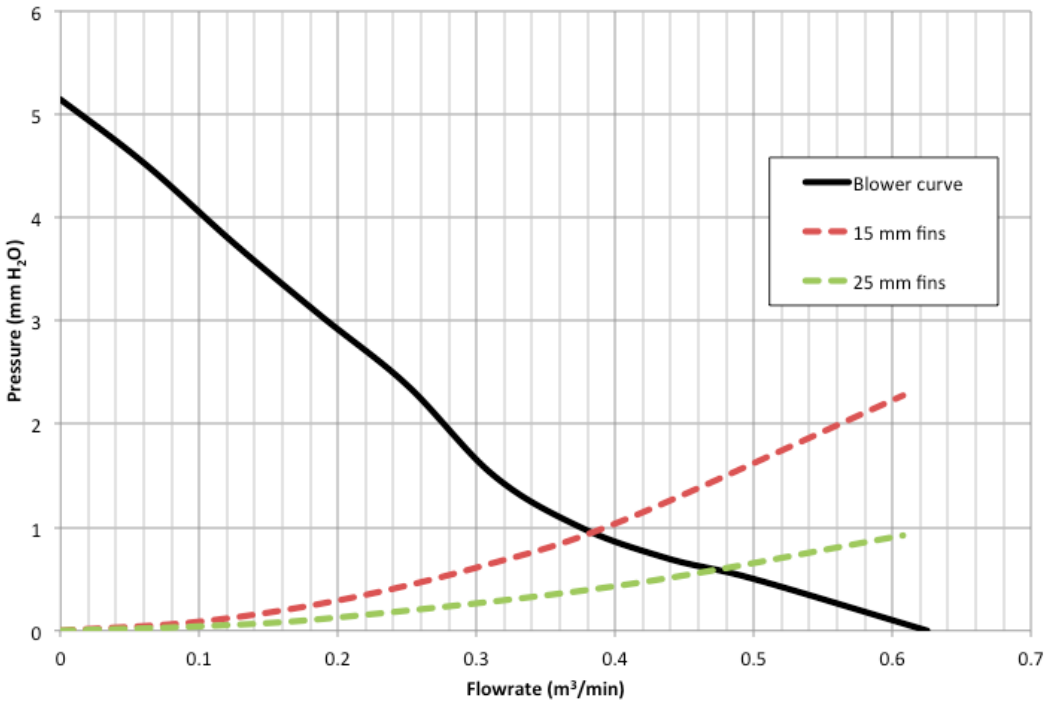

Fig. 2.14. Blower curve for fan model d5015 with superimposed system curves for pin-in arrays consisting of 15 and 25 mm fin heights.

The displays of the flow fields corresponding respectively to blower-curve-based uniform inlet flow and the rotating-fan-based inlet flow are presented in Figs. 2.15 and 2.16. Owing to symmetry, the displayed information corresponds to one-quarter of the fin array, with the center of the array being at the lower right-hand corner. Each figure consists of six panels. The leftmost column of panels conveys information by means of normalized same-length vectors, whereas vectors whose lengths correspond to velocity magnitudes are displayed in the right-hand column. Each horizontal row of panels applies to the velocity field in a plane parallel to the inlet plane and displaced from it by the indicated distances.

Attention is first directed to Fig. 2.15. An overall appraisal of the figure reveals a very strong outflow of fluid through the outboard edges of the array. At the uppermost plane, the normalized vectors in the left panel appear to convey faulty information in that a strong inflow is also seem. However, when the true velocity-magnitude vector lengths are exhibited in the right panel, it is seen that the magnitude of the inflow is vanishingly small. Of note is the general regularity of the flow field portrayed by the vector diagrams.

This regularity is to be contrasted with the almost random patterns displayed is the panels that constitute Fig. 2.16. These patterns reflect the irregularities in the air that is produced by the fan rotation. Of particular note with respect to Fig. 2.16 is the significant different in the appearance of the vectors in the left-hand and right-hand panels corresponding to the same geometrical distance from the fin tips. This situation can be attributed to the randomness of the flow field produce by the rotating fan.

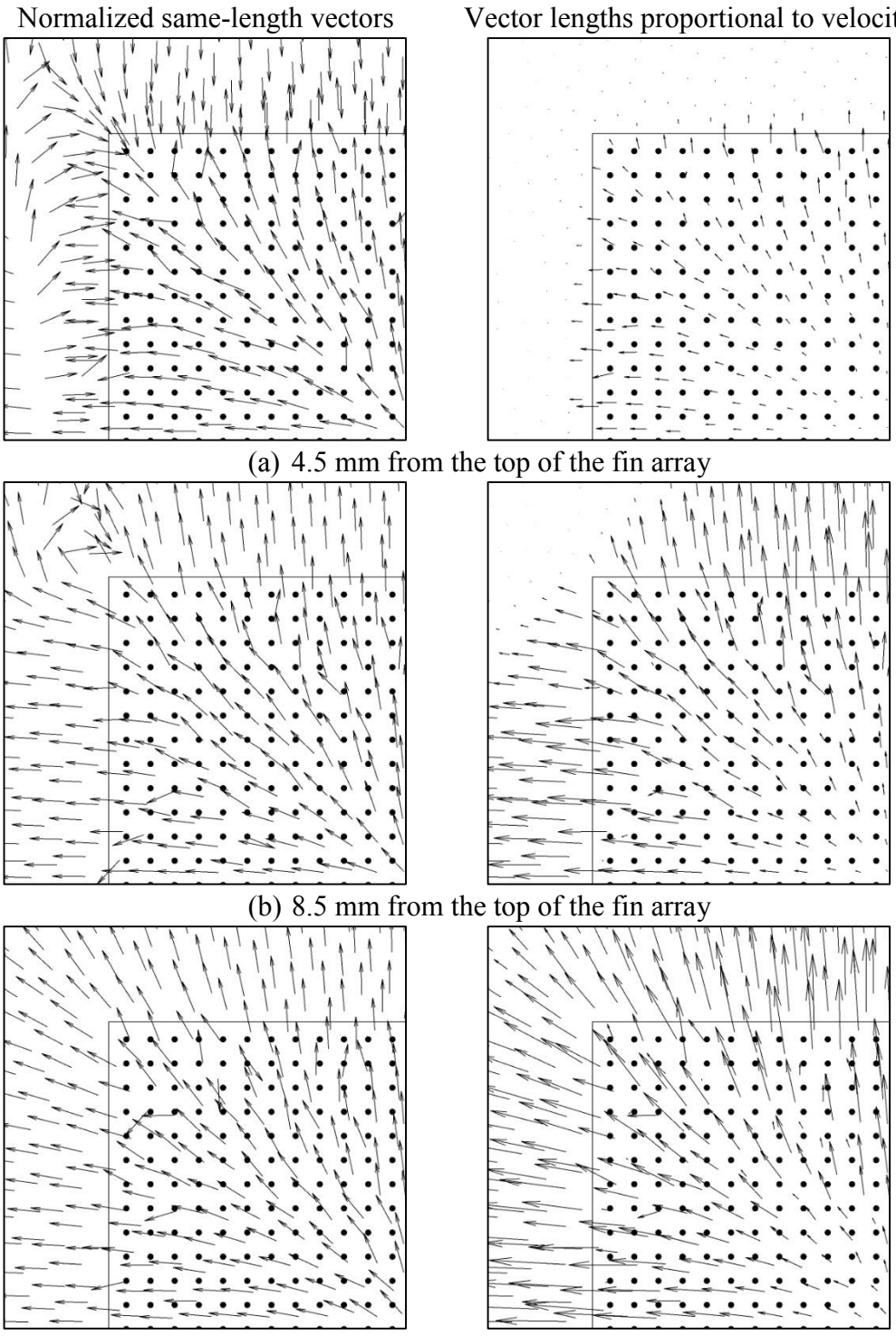

(a) 4.5 mm from the top of the fin array

(b) 8.5 mm from the top of the fin array

(c) 13 mm from the top of the fin array

Fig. 2.15. Vector velocity plots in planes parallel to the flow inlet plane at various distances from that plane. Uniform inlet flow in accordance with the operating point on the blower curve. The presented diagrams correspond to one-quarter of the 15 mm fin array.

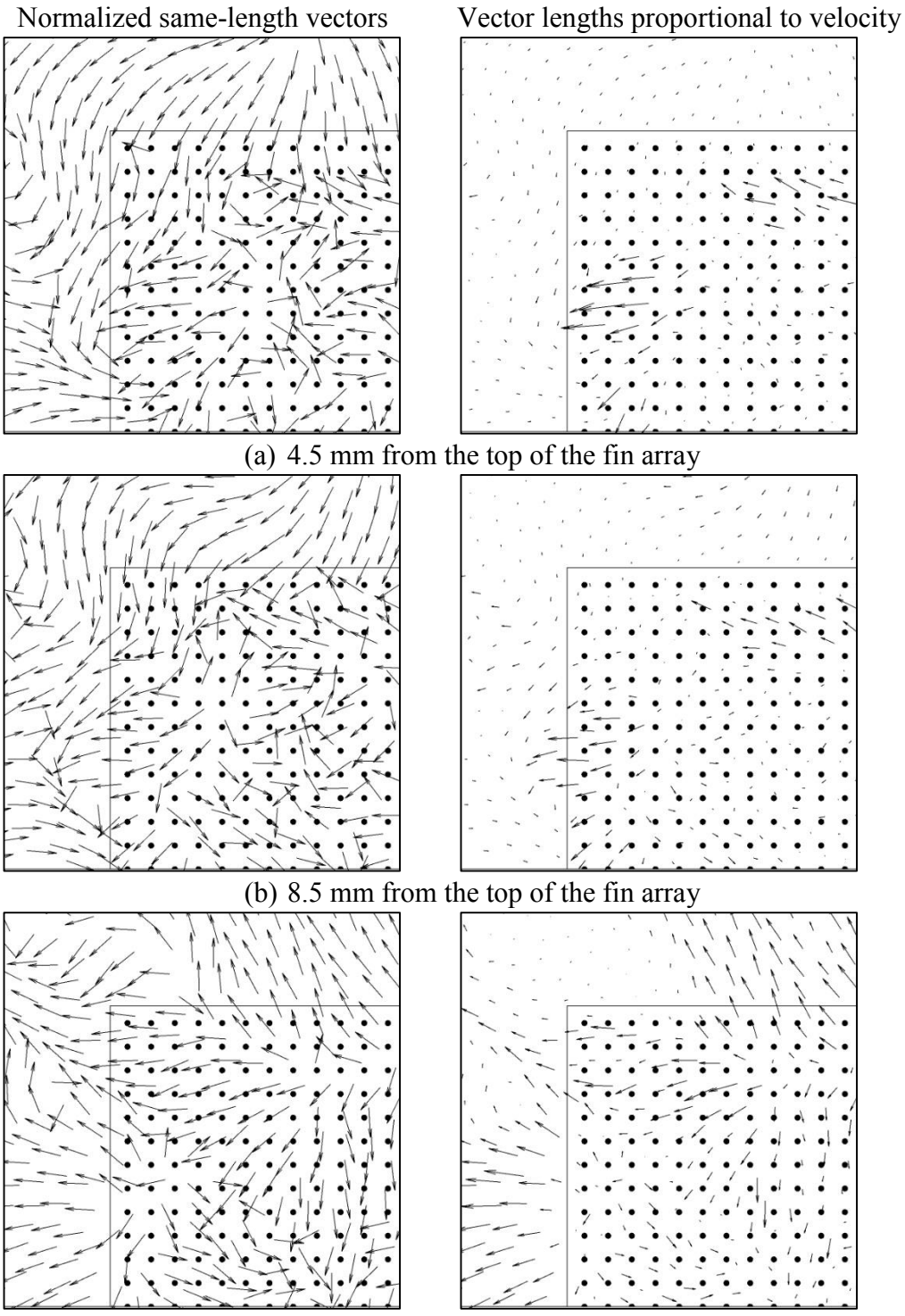

(a) 4.5 mm from the top of the fin array

(b) 8.5 mm from the top of the fin array

(c) 13 mm from the top of the fin array

Fig. 2.16. Vector velocity plots in planes parallel to the flow inlet plane at various distances from that plane. Airflow supplied by fan rotation. The presented diagrams correspond to one-quarter of the 15 mm fin array.

A different perspective on the flow field is conveyed in Fig. 2.17(a) and (b). The view displayed there is the environment surrounding the fin array. The (a) part of the figure shows vectors that are normalized and of the same length, whereas the (b) part exhibits vectors that are keyed to the fluid velocity. The information in Fig. 2.17 pertains to the fan-delivered fluid flow.

The vector field shown in Fig. 2.17(a) displays a large eddy flanked by downflows. The eddy is driven by tip leakage from the fan. The downflow at the right is the flow that is drawn into the rotating fan, whereas the downflow at the left is driven by the eddy. It would appear that there is a physically unacceptable discontinuity between the direction of the eddy and the right-hand downflow. In reality, the flow is three-dimensional, and the out-of-plane flow activity cannot be portrayed in the figure. A different perspective is conveyed in the (b) part of the figure. It can be seen from the (b) part that the dominate flow is that which is drawn into the fan by the low pressure that it creates.

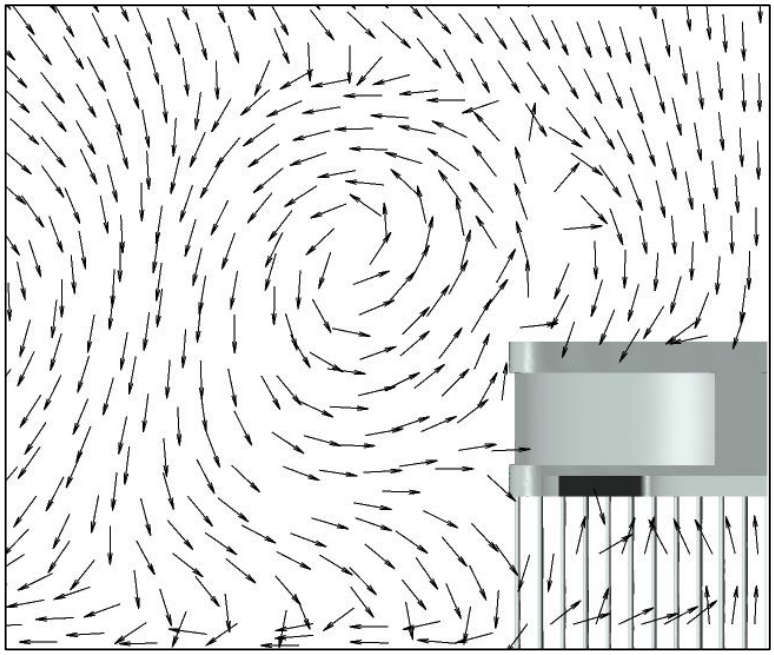

(a)

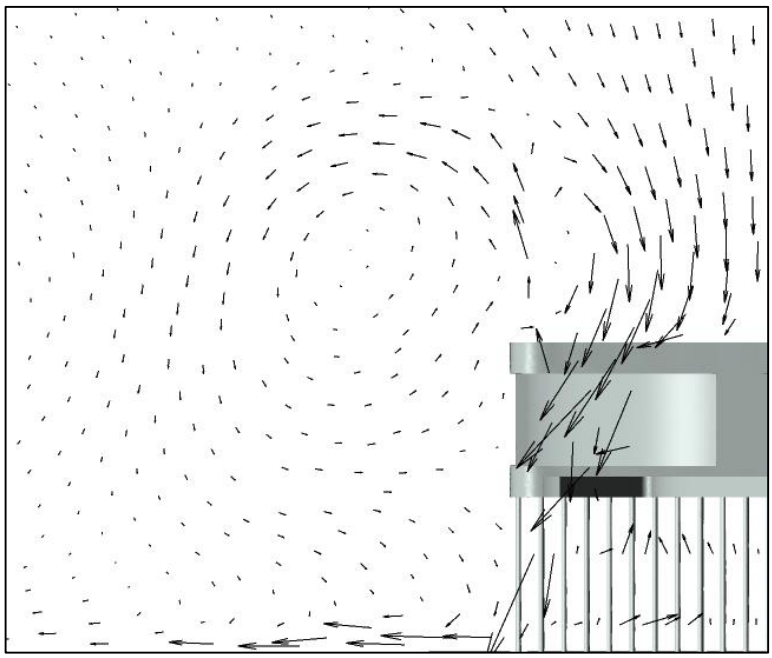

(b)

Fig. 2.17. Vector diagrams displaying the pattern of fluid flow in the space surrounding the 15 mm pin-fin array: (a) normalized same-length vectors; (b) vectors lengths keyed to velocity magnitudes.

Up to now, the presented information has been focused on the directions of the velocities. Now, attention is turned to the velocity magnitudes, and Fig. 2.18 has been prepared for this purpose. The layout of the figure is arranged to show contrasts between the two inlet conditions, uniform velocity and fan driven velocity. As in the previous figures, planes have been cut at three distances from the fin-tip plane. Also, the center of the array continues to be at the lower right-hand corner.

In the (a) part of the figure, which corresponds to the plane nearest to the fin tips, the uniform inlet velocity gives rise to near-uniform velocities in that plane. In sharp contrast, the fan-driven flow is marked by islands of both high and low velocity. With increasing distance from the inlet plane, parts (b) and (c), the uniform inlet velocity case develops strong wakes downstream of the pin fins. In contrast, for the fan-driven case, the flow pattern at the distance of 8.5 mm is only moderately different from that at a distance of 4.5 mm from the fin tips, but wakes are seen to develop at the 13 mm distance.

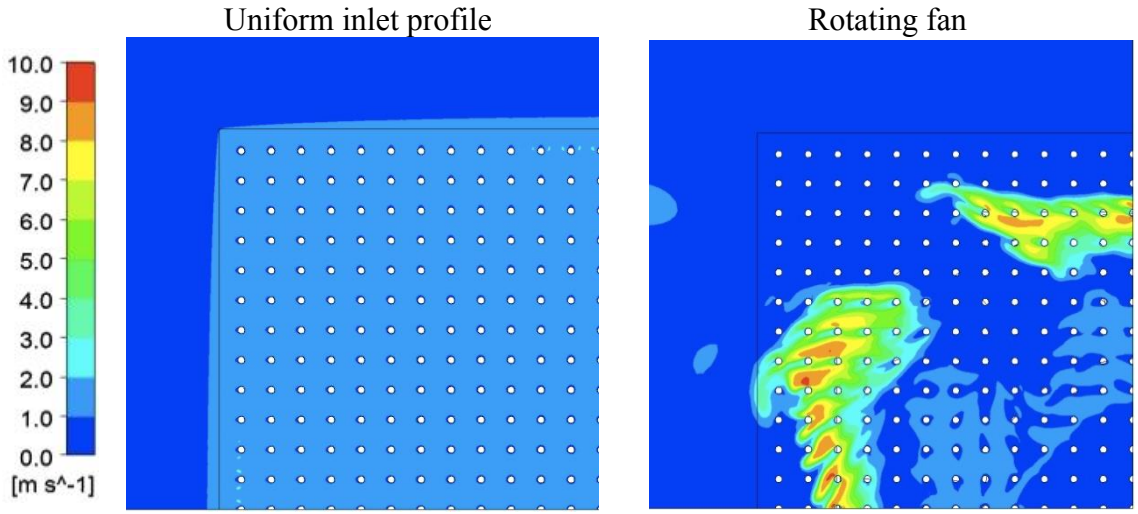

(a) 4.5 mm from the top of the fin array

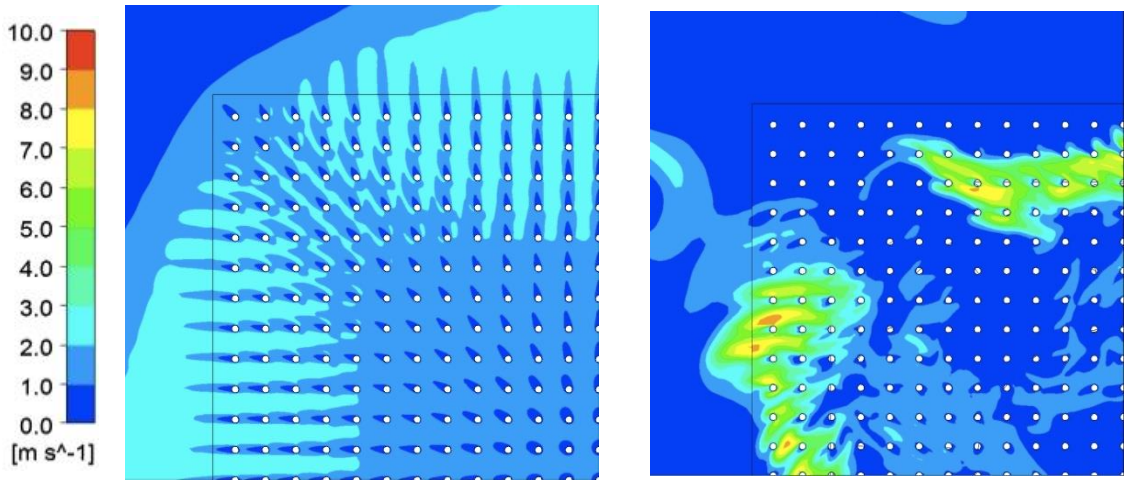

(b) 8.5 mm from the top of the fin array

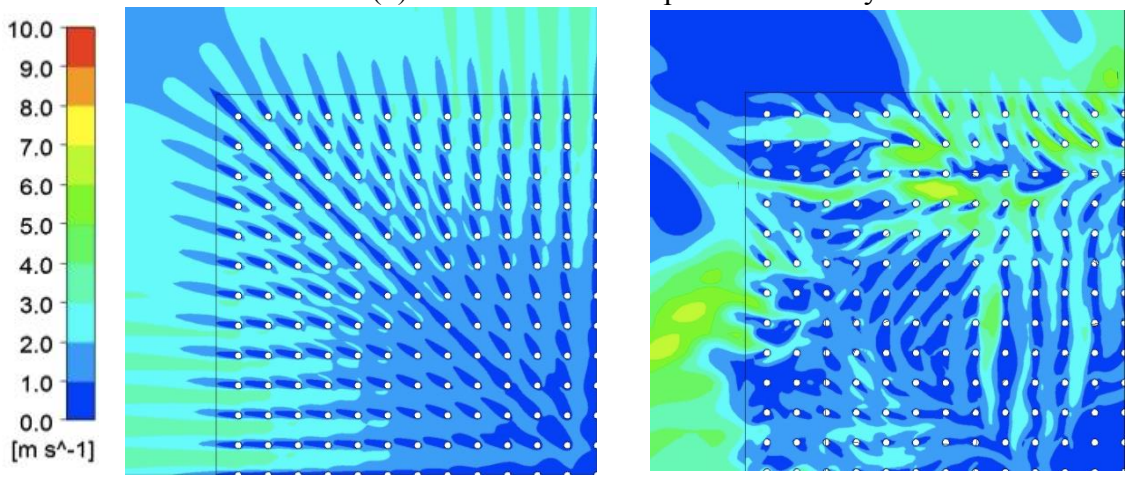

(c) 13 mm from the top of the fin array

Fig. 2.18. Color contour diagrams of velocity magnitudes for both the uniform and fan-delivered inlet flows at three planes within the 15 mm pin-fin array.

2.7 FLOW FIELD PRODUCED BY AN AXIAL FAN INTERACTING WITH A STRAIGHT-FIN ARRAY

Attention will next be turned to the patterns of fluid flow that occur in the interfin passages of an array of straight fins. A schematic diagram of the investigated situation is exhibited in Fig. 2.3. Although the diagram displays three modules, it is common practice for such setups to encompass a larger number. In the presence of a large number of modules, end effects can be neglected when focus is directed to a typical models far removed from the

ends. In accordance with common practice, the fin array is capped by a shroud which lies in a plane defined by the tips of the fins.

As in the case of the foregoing pin-fin-array study, two modes of flow delivery to the array inlet are to be considered. One mode is a muffin fan with rotating blades as pictured in Fig. 2.3. The other is based on the blower curve for the fan in question. For the latter, the postulated uniformly distributed flow provided by the fan is prorated uniformly among the flow passages serviced by the blower.

The specific muffin fan used for the investigation was chosen on the basis of its capability to deliver the flow rate and pressure rise suitable for the application. The chosen fan is d2510, which has an external frame of dimensions of 32 × 32 mm. For the fin dimensions listed in Table 2.2, the width of the fan subtended 26 fins and 25 interfin flow passages. The fin height of 32 mm matched the fan external frame height.

Table 2.2. Dimensions of the straight-fin array and related information

Component	**Dimension**
Fin thickness	0.4 mm
Interfin flow passage	1.0 mm
Fin height	32 mm
Fin length	127 mm
Base thickness	0 mm

The blower curve corresponding to the selected muffin fan is displayed in Fig. 2.19. Also appearing in the figure is the system curve corresponding to the situation in which the same uniformly distributed flow is delivered to the inlets of the 25 interfin flow passages.

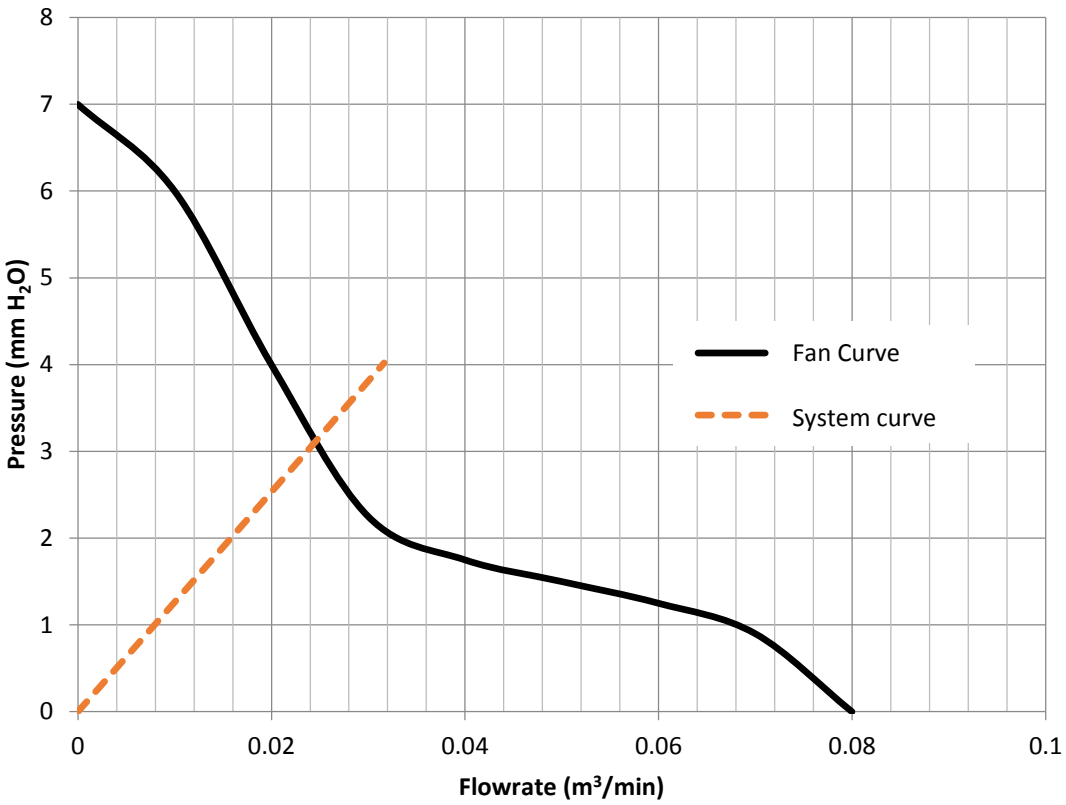

Fig. 2.19 Blower curve for fan d2510 with a superimposed system curve for a straight-fin array consisting of 25 flow channels.

For this case, the patterns of fluid flow in each of the flow passages are the same. Furthermore, that flow pattern is already well established in the literature because it corresponds to the classical case of a uniformly distributed fluid flow entering a flat rectangular duct. In this light, there is little to display with respect to the patterns of fluid flow for the case of the uniformly distributed blower-curve-based inflows.

On the other hand, for the case in which a muffin fan with rotating blades delivers air to the fin array, there are large variations both of magnitude and direction of the respective flows in the 25 flow passages serviced by the fan. Consequently, complex patterns of fluid flow are to be expected. The narrowness of the individual flow passages creates difficulties in mounting a presentation similar to that Figs. 2.15 to 2.18 for the pin-fin array.

The first set of results for the fan-delivered flow to the straight-fin array is displayed in Fig. 2.20. The figure provides a display of the distribution of mass flow rates at the downstream ends of the respective flow passages of the array. Note that the displayed

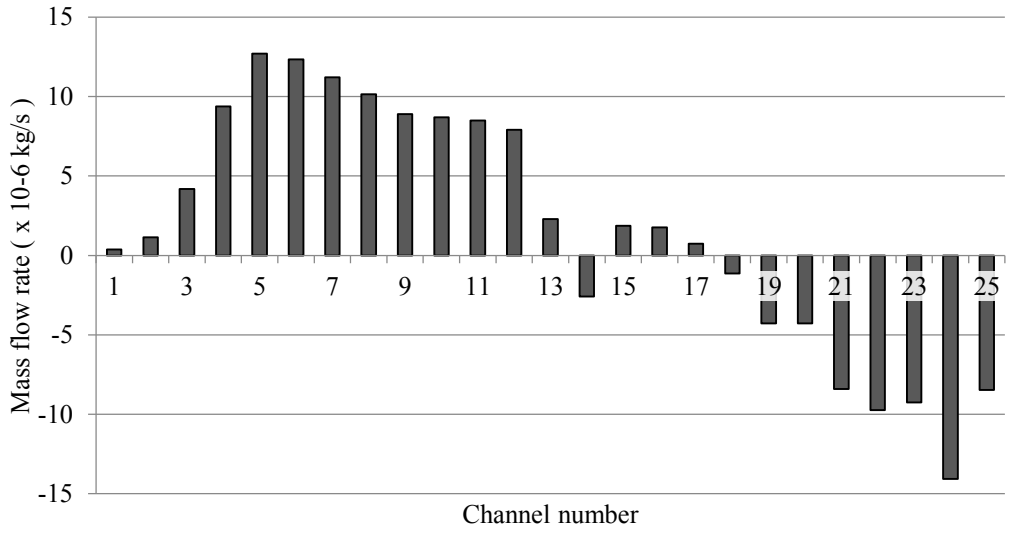

Fig. 2.20. Instantaneous distribution of the mass flow rates at the downstream ends of the flow passages of the straight-fin array.

results pertain to a particular moment of time inasmuch as the flow is unsteady. The numbers deployed along the horizontal axis indicate the flow channel numbers running from 1 to 25. It is seen from the figure that not only are the channel-to-channel flow rates highly non-uniform, but also that certain channels convey forward-moving flow and other channels convey backward-moving flow. The direction of the conveyed flow is strongly dependent of the direction of rotation of the fan.

The run time of the simulation was extended over many revolutions of the fan with a view toward clarifying the timewise variation of the mass flow rates. Figure 2.21 displays the variations of the mass flow rates at the downstream end of each passage as a function of the number of revolutions that were tracked. For context, each revelation of the fan requires 0.04 seconds. The figure contains 25 curves, one for each of the flow passages. Since overall trends are being tracked, the individual curves are not keyed to the specific passages. It can be seen from the figure that there are major changes in the per-passage

flow rates, both in magnitude and direction, as the fan rotation proceeds. There is a clear trend for early-time negative mass flows to become positive. There is no indication that a steady state will be achieved.

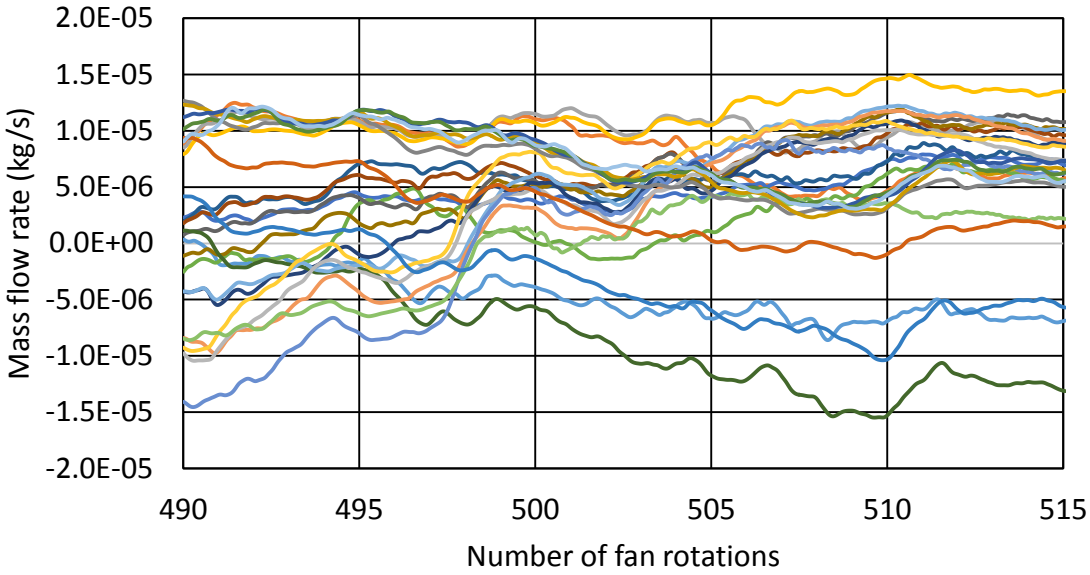

Fig. 2.21. Variation of the flow rates at the downstream ends of the individual flow passages as a function of the number of fan rotations.

Another perspective on the patterns of fluid flow can be obtained from velocity color contour diagrams. Such diagrams have been created by cutting vertical planes parallel to the plane that encompasses to the upstream face of the straight-fin array. The first such color contour display, Fig. 2.22, is at the upstream face itself. The information conveyed in the figure corresponds to the streamwise velocities at the downstream face of the fan (which is coincident with the upstream face of the array). Worthy of note is that the fan provides both forward flow and back flow to the inlet of the fin array. The latter may be attributed to the low pressure associated with a tornado-like swirl.

Another perspective on the patterns of fluid flow in the various flow passages is set forth in Fig. 2.22 (a)-(d). These figures correspond to cross-sectional planes situated at a succession of downstream distances from the inlet of the fin array. In this regard, it is relevant to recall that the inlet face of the array corresponds to the downstream face of the

rotating fan. The first of the figures, part (a), is for the array inlet section. The color contours correspond to the footprint of the air velocity provided by the fan. It can be seen from the figure that there is a circular core of virtually zero-velocity fluid. The zone of negative velocities adjacent to the core is due to the low pressure caused by the fan rotation. The annulus of high velocities that is wrapped around the negative-velocity zone reflects the interaction between the rotating blades and the fluid.

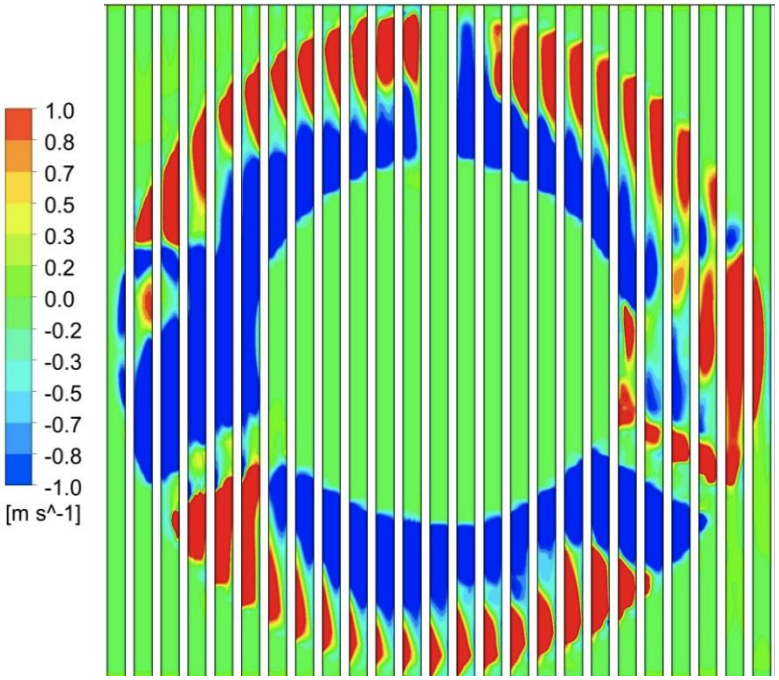

(a) 0 cm from inlet

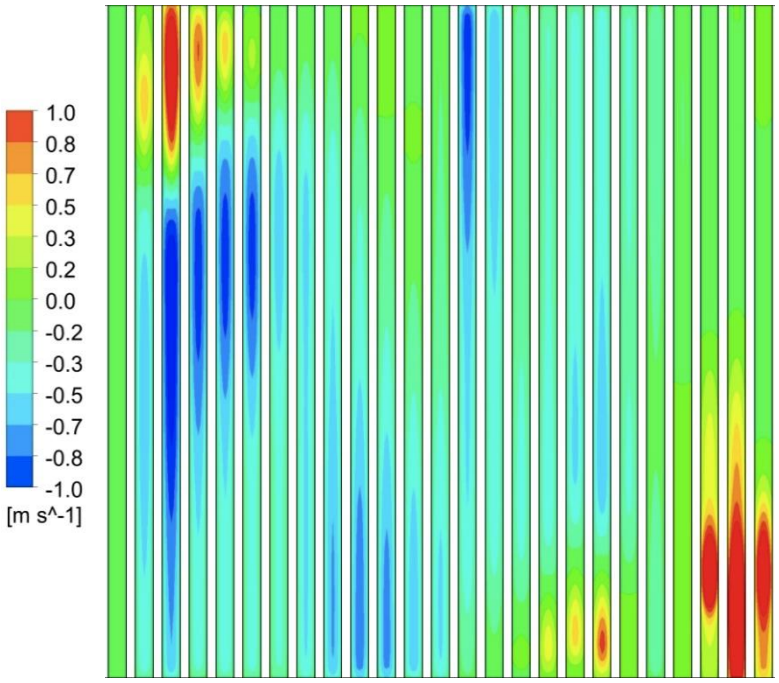

(b) 1 cm from inlet

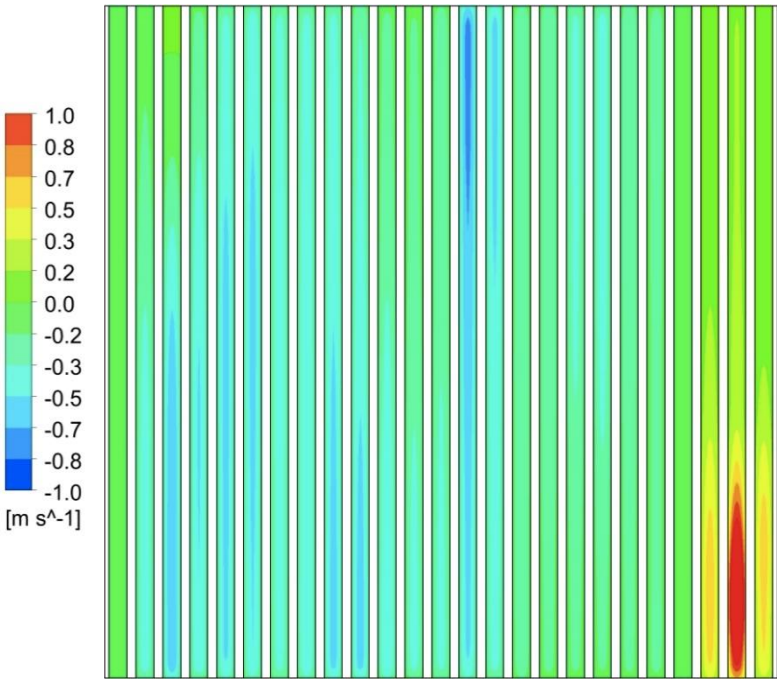

(c) 2 cm from inlet

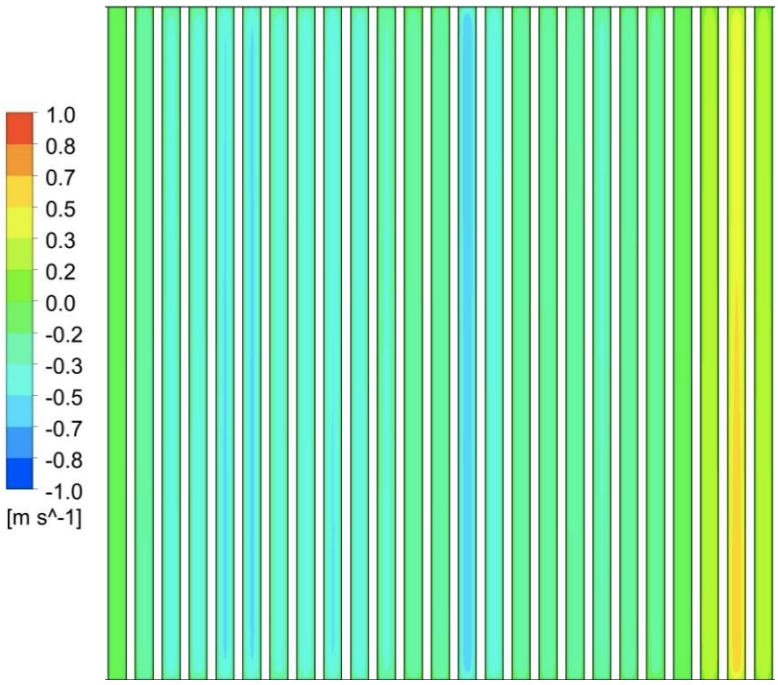

(d) 4 cm from inlet

Fig. 2.22. Color contour diagrams of velocity magnitude at a succession of cross-sectional planes situated at different distances from the inlet face of the straight-fin array.

The (b) part of the figure corresponds to a plane situated one centimeters from the inlet cross section. As seen from the figure, the flow pattern imposed by the fan at array inlet has totally dissolved at the small downstream distance of part (b). In some of the passages, the flow is all in the positive direction; in others, it is all in the negative direction; and in still others, there are both positive- and negative-direction flows.

At two centimeters downstream of the inlet, part (c), further transformations of the flow patterns are in evidence. There is some evidence of a legacy from the flow pattern displayed at one centimeter, but there is also some parts of the flow pattern that are quite altered.

The last figure in this set is part (d) which corresponds to a distance of four centimeters from the inlet. Careful inspection of parts (c) and (d) indicates a tendency toward considerably slower change.

2.8 HEAT TRANSFER RESULTS FOR AN AXIAL FAN INTERACTING WITH A PIN-FIN ARRAY

As a necessary prelude to the presentation of the heat transfer results for the pin-fin array, a listing of the investigated cases is appropriate. That information is conveyed in Table 2.3.

Table 2.3. Investigated cases for heat transfer for a pin-fin array

Fin length	**Blower curve**		**Rotating fan**
15 mm	isothermal fins isothermal base	aluminum fins isothermal base	aluminum fins isothermal base
25 mm	isothermal fins isothermal base	aluminum fins isothermal base	aluminum fins isothermal base

The first focus of the presentation of results is local pin-fin information. To this end, the heat transfer rates at all of the fins in the array were linearly averaged as a baseline. Then, per-fin ratios of the fin heat transfer rate to the averaged heat transfer rate were prepared and displayed on a matrix that is conveyed in Fig. 2.23. The presented matrix is actually one-quarter of the entire array. The results for all other quadrants are identical to that shown in the figure. The exact center of the array is at the midpoint of the fin at the location (1, 1). A symmetry line runs vertically upward through the midpoints of the fins which from a column at the left-hand edge of the display. Correspondingly, another symmetry line runs horizontally through the midpoints of the fins that form the bottom row of the display. The upper edge of the displayed array is open to the environment as is the rightmost edge.

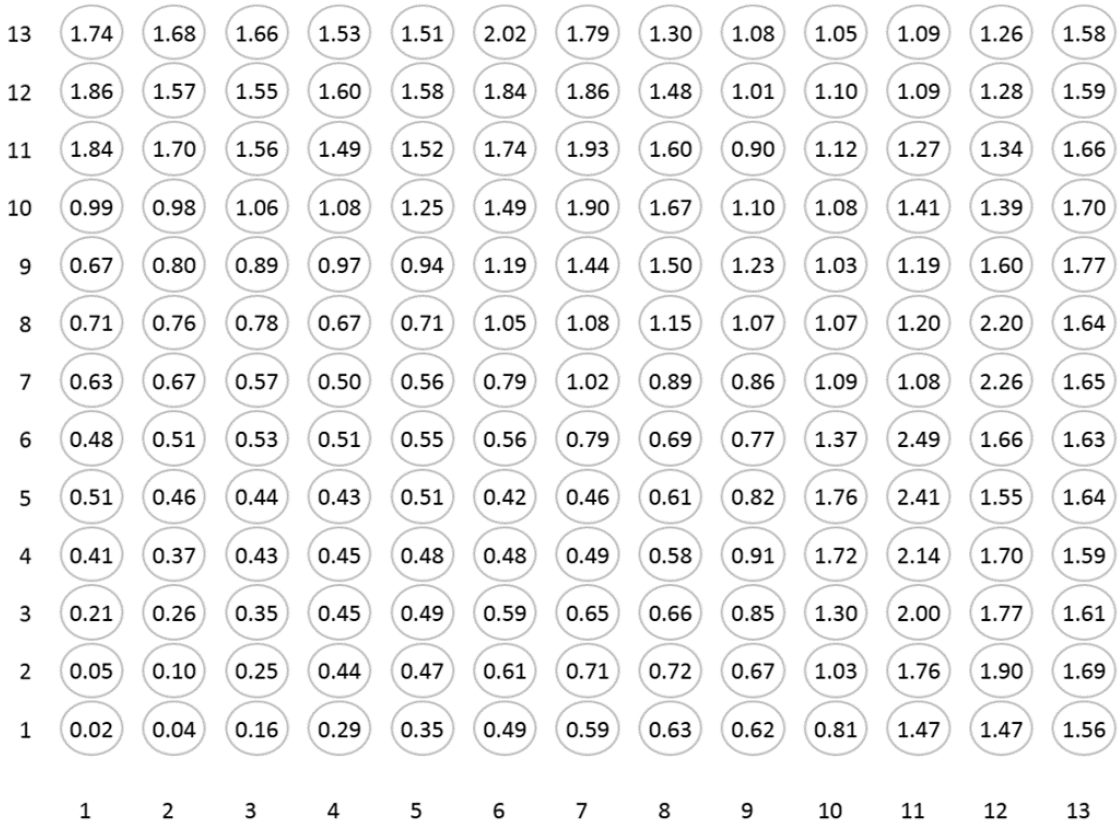

Fig. 2.23. For the fan-driven airflow: per-fin ratio of the fin heat transfer rate to the heat transfer rate averaged over all fins. The displayed matrix corresponds to one-quarter of the entire fin array. The center of the full array is at the location (1, 1). The results correspond to the array in which the fin height is 15 mm.

It can be seen from the figure, that there is an enormous variation in the heat transfer rates among individual fins in the array. Compared with the averaged per-fin heat transfer, the ratios range from 0.02 to 2.49. The higher heat transfer rates occur at pin fins that are located at greater distances from the center. In the central region of the array, relatively low heat transfer rates are encountered.

An alternative view of the spatial variation of the per-fin heat transfer rates is presented in Fig. 2.24 in the form of a three-dimensional bar diagram. This presentation reinforces the extreme variation that was already identified in Fig. 2.23 but calls special attention to the valley adjacent to the central region of the array.

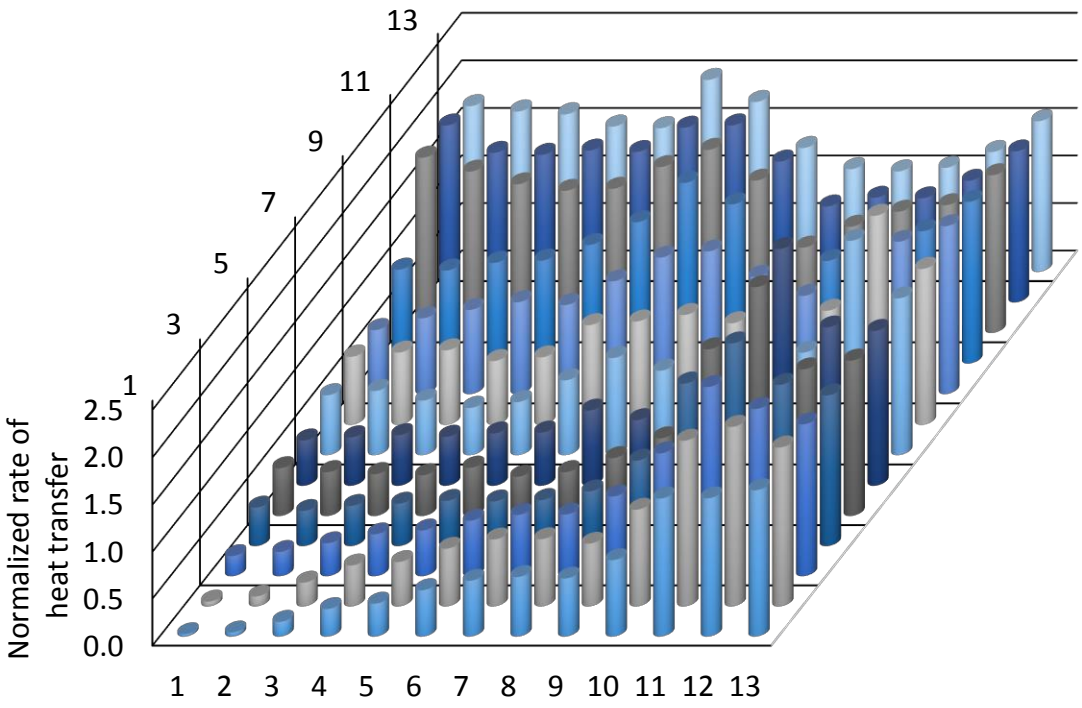

Fig. 2.24. Three-dimensional representation of the normalized heat transfer produced by fan-driven airflow for a one-quarter section of a 15 mm pin-fin array. The center of the fin array is at (1, 1).

The heat transfer results for the blower-curve-delivered airflow are set forth in Fig. 2.25. In connection with these results, it is worthy to note that the delivered flow is uniformly distributed across a plane that encompasses the fin tips. Consequently, it is not surprising that the per-fin heat transfer rates are relatively uniform. Inspection of Fig. 2.25 reveals a overall variation of the normalized per-fin heat transfer from 0.49 to 1.22. If the extremely low value at the center of the array were to be excluded, the range would extend from 0.70 to 1.22.

The dichotomy between the results for fan-delivered and uniform blower-curve airflow is of great practical significance. It is clear that significant errors would be made if design were based on the latter model.

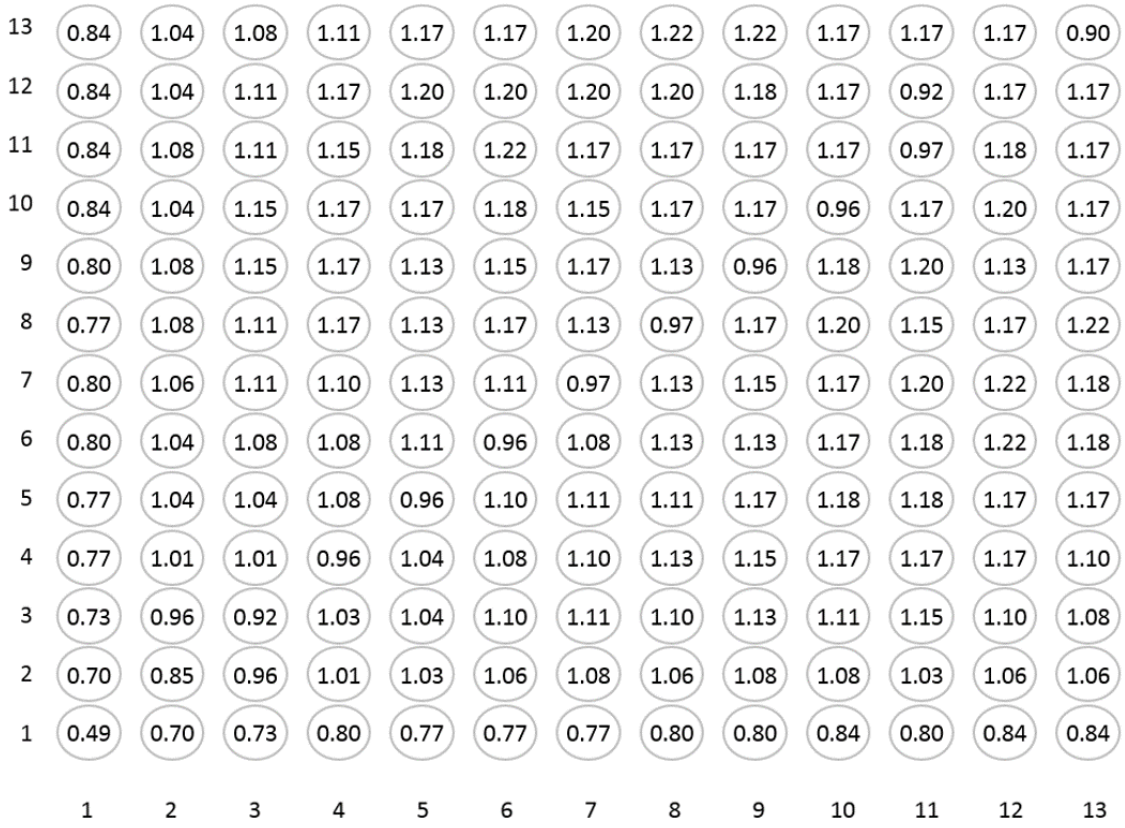

Fig. 2.25. For blower-curve-driven flow: per-fin ratio of the fin heat transfer rate to the heat transfer rate averaged over all fins. The displayed matrix corresponds to one-quarter of the entire fin array. The center of the full array is at the location (1, 1). The results correspond to the array in which the fin height is 15 mm.

A bar-graph display that corresponds to Fig. 2.25 is conveyed in Fig. 2.26. The striking feature of the latter display is the uniformity of the heights.

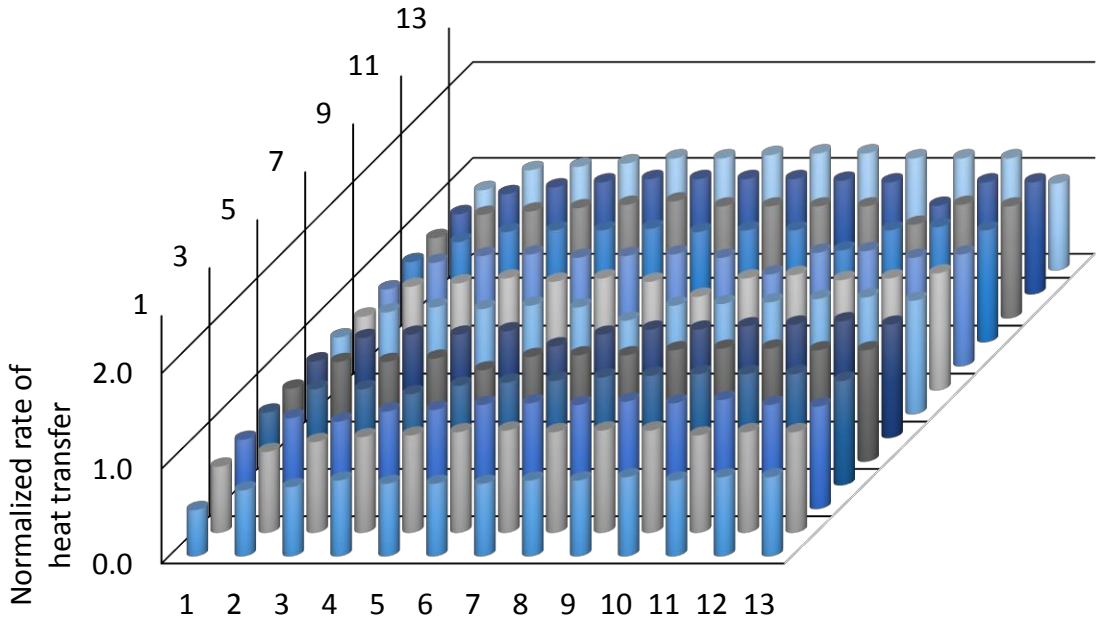

Fig. 2.26. Three-dimensional representation of the normalized heat transfer produced by uniform blower-curve-based airflow for a one-quarter section of a 15 mm pin-fin array. The center of the fin array is at (1, 1).

From the standpoint of practical utility, the overall rate of heat transfer from the array as a whole is of major significance. The results for this quantity is presented in Table 2.4 in which the rotating-fan-delivered-airflow case is contrasted with those for the blower-curve-based-airflow case. In section of the table reveals an enormous difference between the results for the two cases. Also contrasted in the table is the difference between the results for the isothermal fin model, often utilized for approximate analysis, with those for the non-isothermal aluminum fins.

Attention is first turned to the comparison between the blower-curve-based results and the rotating-fan-based results. For the 15-mm height fins, the former heat transfer rate is 51% higher than the actual, while for the 25-mm height fins, the over prediction is 59%. These errors are of great practical importance and underscore the fallacy of the longstanding traditional design model. From the standpoint of practice, the numerical simulation to

implement the latter model is, in itself, not very likely to occur because the mindset of current practitioners.

Table 2.4. Overall pin-fin heat transfer results contrasting rotating-fan-delivered air with uniform blower-curve-based air flow.

Fin length	Heat transfer (W)		
	Blower curve, isothermal fins	Blower curve, aluminum fins	Rotating fan, aluminum fins
15 mm	55.0	40.6	26.8
25 mm	97.4	53.9	33.8

A second comparison that follows from the table is the contrast between the idealized-isothermal-fin and the aluminum-fin cases, both based on the blower-curve, air-delivery model. For the 15-mm fin height, the isothermal model overestimates the rate of heat transfer by 35%; for the 25-mm fin height, the over prediction is 81%.

The third comparison relates to the effect of fin height. The ratio of the heat transfer rate for the taller fin height to that for the shorter fin height is 26% for the rotating-fan case, 33% for the blower-curve case with aluminum fins, and 77% blower-curve case with isothermal fins. Of particular note with respect to the latter finding is that the geometric ratio of the two fin heights is 67%. Once again, the use of a uniform inlet velocity leads to substantial errors with respect to those for the rotating fan.

2.9 HEAT TRANSFER RESULTS PRODUCED BY AN AXIAL FAN INTERACTING WITH AN ARRAY OF STRAIGHT FINS

The presentation of results for the straight fin array is initiated by a comparison of the per-fin heat transfer rates. Let the symbol $Q_{fin,i}$ denote the rate of heat transfer at fin i in the array, where i runs from 1 to 26. Additionally, let $Q_{fin,avg}$ be the average of the 26 values of $Q_{fin,i}$. The ratio of $Q_{fin,i}$ to $Q_{fin,avg}$ is displayed in Fig. 2.27 for the array serviced by a rotating fan. If the two outboard fins are neglected, the ratios range from a minimum of 0.67 to a

maximum of 1.59. The two outboard fins experience heat transfer at only one of their two faces, so that the displayed ratios are not worthy of direct comparison with the other fins in the array. The lowest heat transfer value occurs at the fin aligned with the axis of the fan. This outcome can be attributed with the presence of a tornado-like low pressure zone which resists the forward-directed fluid flow. There are local maxima which correspond to the forward flow created in the open annulus situated between the outer diameter of the hub and the frame of the fan.

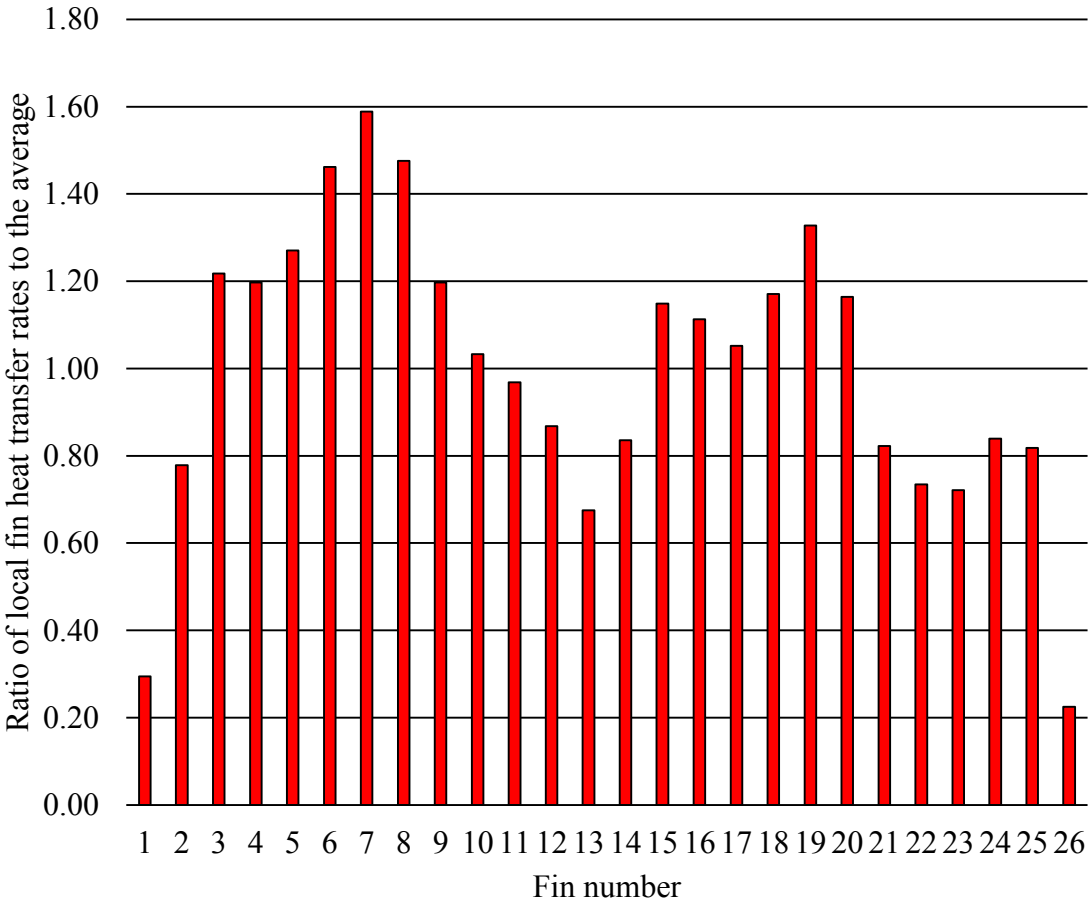

Fig. 2.27. Ratios of the local fin heat transfer rates to the average for the fan-driven airflow.

For the case of the uniform blower-curve-based airflow, the heat transfer rate for all 26 fins is identical. Therefore, the ratio of the local fin heat transfer rate to the average is one.

It is also relevant to compare the average heat transfer rates for the two modes of air delivery. This comparison may be expressed by the ratio

$$\frac{(Q_{fin,avg})_{blower\ curve}}{(Q_{fin,avg})_{rotating\ fan}} = 1.93 \tag{2.9}$$

This outcome indicates that the simple use of the blower curve gives rise to an over prediction of almost a factor of two in the heat transfer rate.

Another relevant modeling issue, never before quantified, relates to the standard practice of ignoring the heat transfer rates at the front and back faces of a straight fin situated in a large array. The quantification of this issue has been extracted from the numerical solutions for the rotating-fan-delivered air flow. The results are presented in ratio form as

$$\frac{Q_{front\ face}}{Q_{total\ fin}} \tag{2.10}$$

and

$$\frac{Q_{back\ face}}{Q_{total\ fin}} \tag{2.11}$$

The first of these ratios is presented in Fig. 2.28 for each of the 26 fins in the array. It can be seen from the figure that the maximum front-face heat transfer rate is 1% of the heat transfer rate from the entire fin. The majority of the fins display front-face heat transfer ratios that are on the order of 0.5%. The distribution of the ratio as a function of fin number is remarkably similar to that of Fig. 2.27. The similarity between the two distributions suggest that the higher the total fin heat transfer rate, the higher is the front face rate as well.

Focus will now be directed to the display of the back-face heat transfer rate. This information is conveyed in Fig. 2.29 by the ratio set forth in Eq. (2.11). The results are displayed in a manner that is identical to the display of Fig. 2.28. The comparison of the two figures indicates that the back-face heat transfer rates are generally higher than those for the front-face. This difference can be attributed to the fact that the frame of the fan creates a partial blockage of the air that would otherwise be freely delivered to the front face. Such a blockage is not present for the back face. Notwithstanding the slightly larger back-face heat transfer, it is still a small fraction of the total per-fin heat transfer rate.

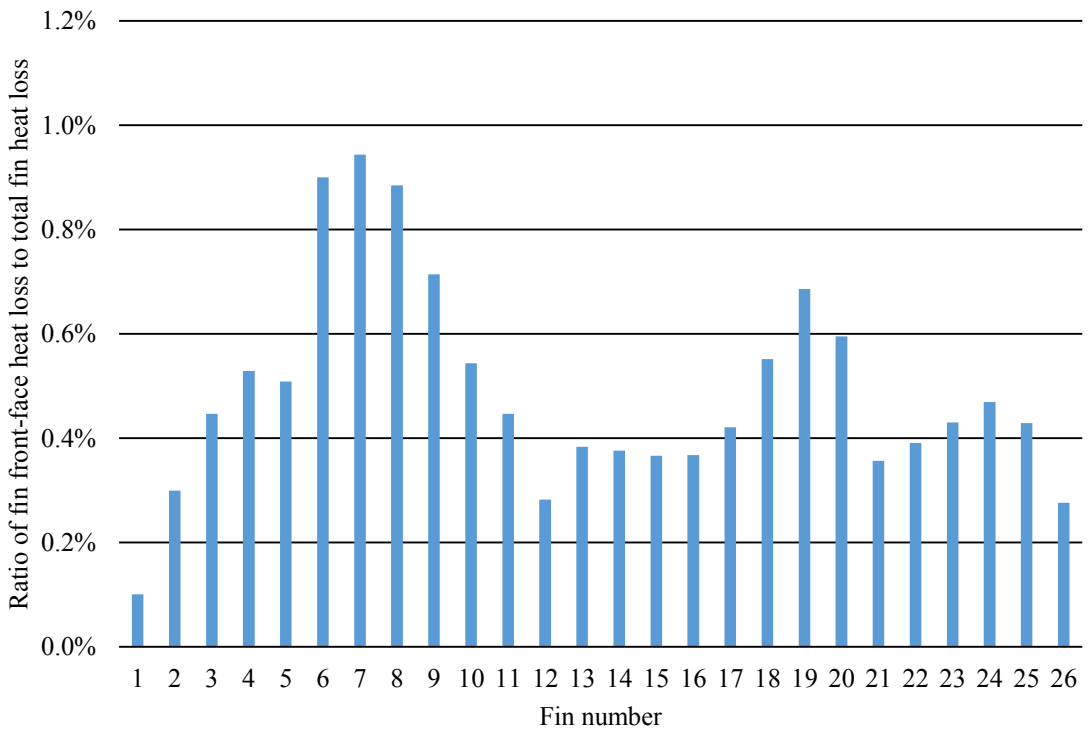

Fig. 2.28. Fin front-face heat loss relative to fin total heat loss for rotating-fan-delivered airflow.

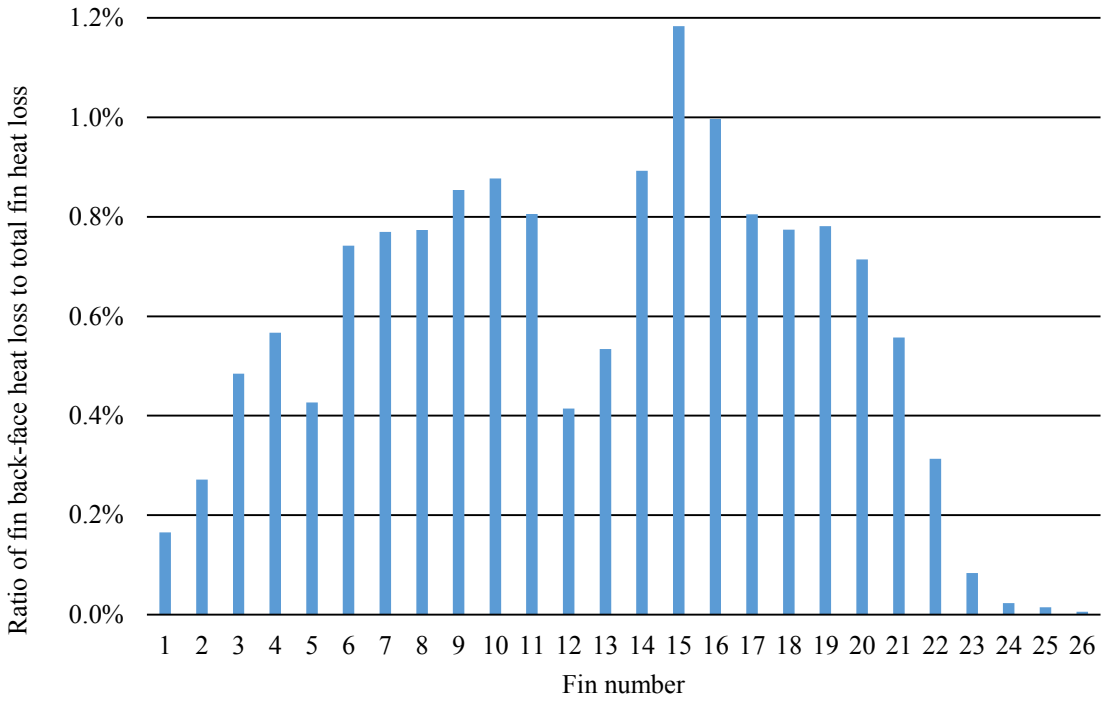

Fig. 2.29. Fin back-face heat loss relative to fin total heat loss for rotating-fan-delivered airflow.

The final and most practically relevant outcome is the comparison of the total array heat transfer rates between the rotating-fan case and the blower-curve-based case. This information is conveyed in Table 2.5 by comparing the second and third columns. That comparison shows that the blower-curve-based model over predicts the rate of heat transfer relative to that predicted by the rotating-fan model. This outcome serves to discredit the use of the blower-curve-based model for practical calculations. The latter model is readily implemented in practice since it gives rise to the same heat transfer rate for each fin in the array. However, this simplification is purchased at a very high cost of accuracy.

Table 2.5. Overall straight-fin heat transfer results contrasting rotating-fan-delivered air with uniform blower-curve-based air flow.

Heat transfer (W)		
Blower curve, isothermal fins	Blower curve, aluminum fins	Rotating fan, aluminum fins
15.1	9.59	4.98

2.10 RETROSPECTIVE FOR CHAPTER 2

The underlying motivation for this chapter is to confront the legacy of traditional heat transfer analysis and demonstrate its relevance to contemporary heat transfer design. To place this critique in context, it must be remembered that the venerable approaches were created many decades ago, before the availability of modern instrumentation and before the advent of digital computers. As a consequence, the understanding of the fundamental processes underlying the transfer of heat was modest. In particular, the fluid mechanics which underlies and governs convective heat transfer was often misunderstood and/or improperly applied. In this light, the theme of this chapter is not intended as raw criticism. Rather, it is the present purpose to identify the error-causing weaknesses of the traditional methodologies and to replaces these methodologies with new approaches that incorporate the realities of the participating physical processes.

It was deemed appropriate to perform the dual tasks of diagnosis of traditional methodologies and the development of new methodologies of high fidelity by means of specific case studies. Two specific case studies of immediate practical relevance to the thermal management of electronic equipment were selected. These case studies also are relevant to other practical applications. One case study is focused on convective heat transfer from a pin-fin array to a coolant air flow, with the flow entering the array through a plane encompassing the fin tips. The other case study is an array of air-cooled straight rectangular fins. The fins are arranged parallel to each other, and air flows longitudinally through the interfin spaces. The latter case is universally encountered in all heat transfer textbooks extending from the first ever-written text to the present. In this context, the outcomes presented here for this case are expected to have a strong pedagogical message.

In order to create a setting in which to make suitable comparisons between the traditional and the new, a common protocol was devised for both case studies. Specifically, for the traditional approach, the best possible version was selected. That version was based on the use of a blower curve. An alternative version, the arbitrary selection of a flowrate without

any consideration of pressure drop constraints, was regarded as being prone to lesser accuracy. However, as pointed out in the body of the chapter, the use of a blower curve is not without faults. Blower curves are based on data collected after the output of the fluid mover had been straightened and homogenized. In practical applications, it is rare that such pains are taken.

For the first case study, the volumetric flow from the blower curve was assumed to be uniformly distributed over a plane that encompassed the tips of the pin fins. In the case of the array of straight fins, the volumetric flow output given by the blower curve was uniformly prorated among the participating interfin spaces.

The new approach set forth here is based on the use of axial fans whose blade rotation was simulated with high precision. An appropriate fan size and capacity was chosen for each of the case studies. For the first case study, the exit cross section of the fan coincided with the plane that encompassed the fin tips. In the second case, the exit plane was congruent with the plane that included the upstream faces of the fins.

The comparison of the fluid flow results for the pin fin array, respectively from the traditional and new approaches, revealed remarkable differences. For example, whereas the traditional approach predicted fluid outflow from one of the external-facing sides of the array, the new rotating-fan simulation approach predicted a fluid inflow through that same side. The patterns of fluid flow within the array predicted by the respective approaches were drastically different. For the traditional model, the flow pattern was well organized and orderly. In contrast, for the rotating-fan model, islands of higher disordered flow were randomly dispersed.

The local per-fin heat transfer results were true reflections of the just-described patterns of fluid flow. For the rotating-fan-driven flow, the lowest to the highest per-fin heat transfer rates ranged from 2 to 249% of the average per-fin heat transfer rate. In contrast, for the case of uniform inflowing fluid, the corresponding range is from 49 to 1.22% of the

average. This enormous difference is strong testimony of the inappropriateness of the traditional uniform-fluid -inflow model.

Further supporting evidence of the foregoing conclusion is supplied by a comparison of the overall heat transfer rates for the pin-fin array as a whole. In that regard, the uniform fluid inflow model over predicted the overall rate by 51 to 60%, depending on the fin height.

The outcome of the comparison between rotating-fan-driven inflow and uniformly distributed inflow for the array of straight parallel fins displays the same trends as were enunciated for the pin-fin array. Among the 25 parallel fluid-flow channels that spanned the array, there were no common fluid flow rates for the case of fan-driven flow. In fact, some of the passages displayed reverse flow. In contrast, the uniform inflow case was characterized by the same flow rate in all of the flow passages.

The local per-fin heat transfer rates varied over a considerable range in the presence of the rotating fan-driven flow. The low-to-high variation ranged from 22 to 159% of the per-fin average. For the uniformly distributed inflow, all fins experience the same heat transfer rate.

The outcomes set forth in the preceding paragraphs provide strong arguments against the further use of the traditional heat transfer model.

Chapter 3

FLUID FLOW PHENOMENA AND HEAT TRANSFER IN THE PRESENCE OF JET-AXIS SWITCHING

3.1 INTRODUCTION

Jet impingement is widely recognized as the most effect way to achieve high rates of local heat transfer. Although jets are often associated with circular cross sections, there are many applications for non-circular jets. In the case of the latter, a large number of studies have been published about a unique phenomenon designated as *jet-axis switching*. The literature on jet-axis switching, while extensive, is totally focused on erudite fluid mechanic phenomena which have been published in journals where applications are never a concern. In particular, no engineering applications have been treated in that literature. For present purposes, there is nothing in the literature that relates to the research performed here aside from the fact that jet-axis switching exists. To confirm that existence, reference may be made to [26-33].

Jet-axis switching can be described by making reference to rectangular or elliptical jets. These jets can be characterized by their aspect ratios. Envision a rectangular jet emerging from a nozzle with its long dimension in a horizontal plane. As the jet flows in the downstream direction, the long dimension may, depending on the operating conditions, switch from its original horizontal lay to a vertical lay. The literature dealing with the switching phenomenon has been totally focused on the involved micro fluid processes without regard to applications.

A major issue with the published literature relates to the means by which the jet is produced. In several papers, for example [34-37], all related to jets of rectangular cross section, no consideration was given to the means by which the jet was created. Specifically, it was assumed that flow having a given velocity profile exited a rectangular slit. The

majority of the published work was concerned with turbulent jets [34, 35, 38-40], with much less attention having been accorded to laminar jets [36, 37]. Elliptical jets were the focus of a recent review paper [41].

In contrast to the literature cited in the foregoing, the present investigation is concerned with the engineering aspects of the fluid flow and, importantly, with the impact of jet axis switching on heat transfer. The jets in question were created by laminar flow in a rectangular duct whose exit cross section was partially blocked by an orifice plate with a rectangular slot. The fluid exiting the duct becomes turbulent, and the accompanying change of flow regime has to be properly accounted. Two aspect ratios of the duct cross section were considered, as were the aspect ratios of the slots. Several blockage ratios, the ratio of the slot cross-sectional area to the cross-sectional area of the duct, were investigated. The Reynolds number was also varied.

3.2 PHYSICAL MODEL

The description of the physical model is facilitated by reference to Fig. 3.1(a). That figure is a perspective view of a rectangular duct of constant cross section through which a fluid passes in laminar flow. The exit cross section of the duct may be partially blocked by an orifice plate or may otherwise be unobstructed. In either situation, the exiting fluid expands into a large open space. The fluid entering the space may flow either freely without blockage or impinge on a flat surface where heat transfer occurs. A side view of the physical situation is displayed in Fig. 3.1(b).

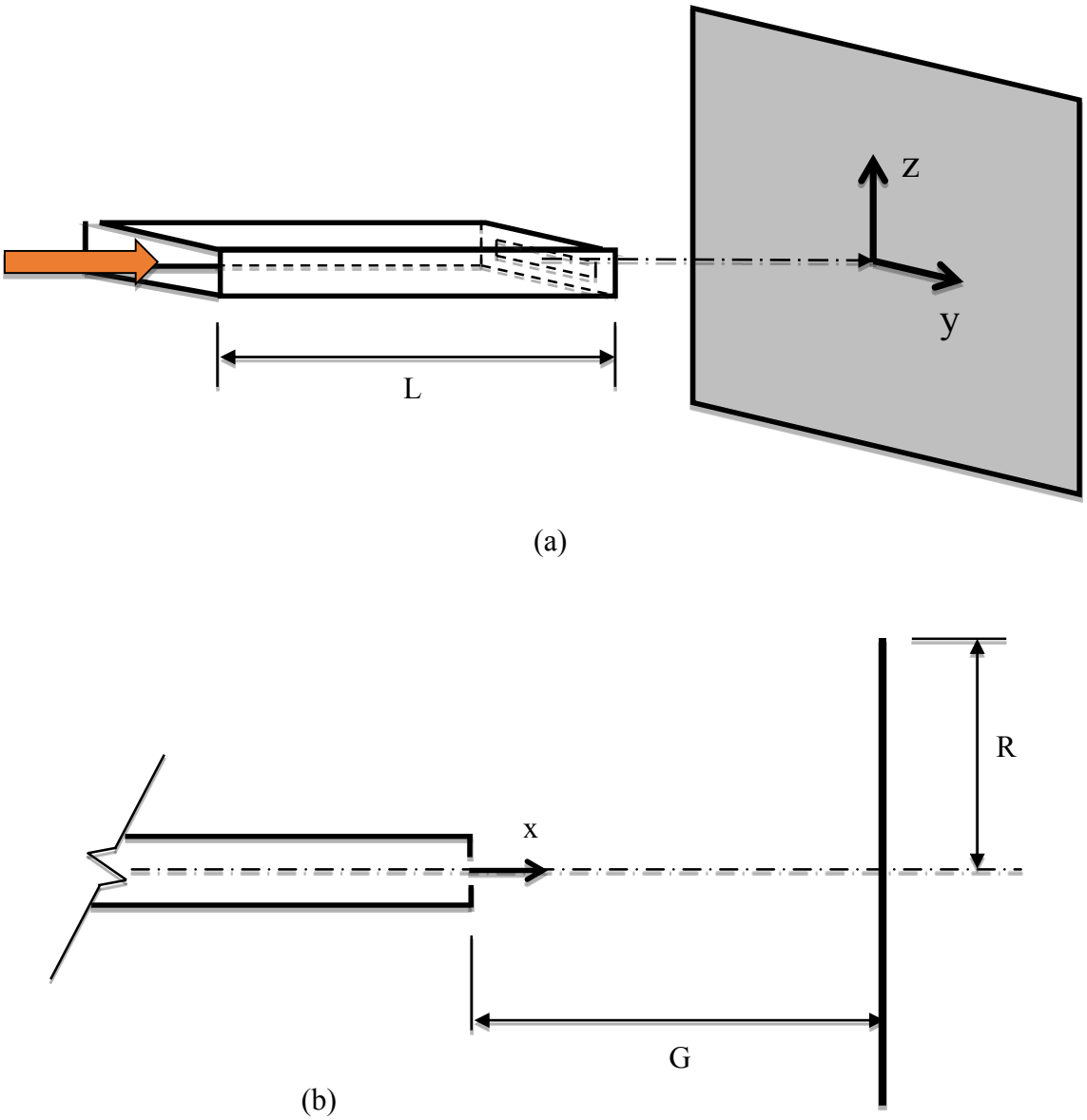

Fig. 3.1. Pictorial view (a) and side view (b) of the physical situation.

Details of the exit plane of the rectangular duct and the orifice plate slot are illustrated in Figs. 3.2(a) and (b). The (a) part of the figure displays both the rectangular cross section and the centered positioning of the slot opening. The aspect ratio of the duct proper is W/H while the aspect ratio of the slot is *a*/*b*. The figure also displays the necessary dimensional nomenclature.

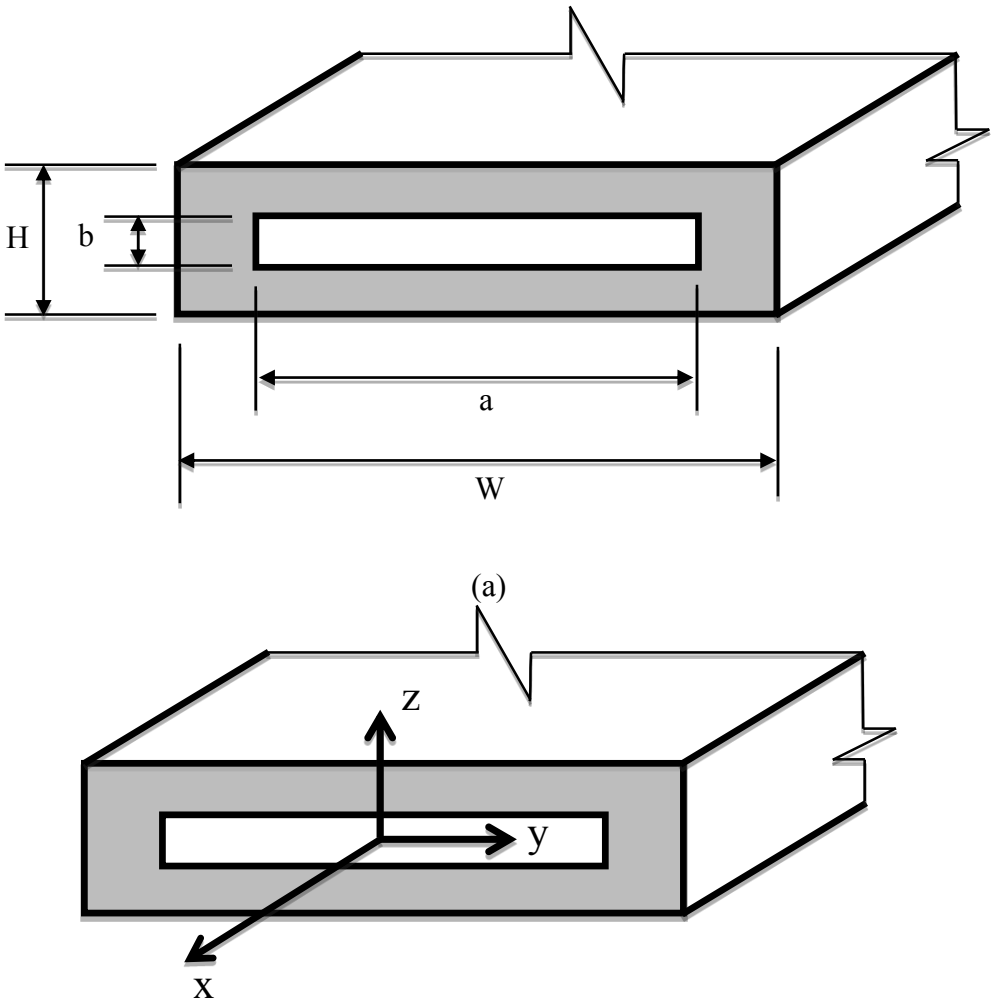

Fig. 3.2. Details of the exit plane of the duct. (a) nomenclature and (b) coordinates.

The (b) part of the figure shows the coordinate system. The flow direction is *x*, while the cross-sectional coordinates are *y* and *z*.

3.3 GOVERNING EQUATIONS

The solution to the physical problem defined in the preceding section was achieved by means of numerical simulation. The simulation model was developed to take account of

the possible change in the flow regime that may occur in the duct proper and in the downstream expansion space. To accommodate such an event, the governing equations are written for turbulent flow, and a turbulence model that reduces to the laminar regime when appropriate is selected. The relevant physical principles that govern the flow and heat transfer are: momentum conservation (Reynolds Average Navier-Stokes equations), mass conservation, and the First Law of Thermodynamics. These equations are written for incompressible, constant property flow, but no restrictions are placed on the type of fluid.

The RANS equations, as written in Cartesian tensor form, are

$$\rho\left(u_i\frac{\partial u_j}{\partial x_i}\right) = -\frac{\partial p}{\partial x_j} + \frac{\partial}{\partial x_i}\left((\mu + \mu_{turb})\frac{\partial u_j}{\partial x_i}\right) \quad i = 1,2,3 \;\; j = 1,2,3 \tag{3.1}$$

The mass conservation equation is

$$\frac{\partial u_i}{\partial x_i} = 0 \tag{3.2}$$

The quantity μ_{turb} is designated as the turbulent viscosity. For the RANS model, it is defined as

$$\mu_{turb} = \rho u_i' u_j' \tag{3.3}$$

where u_i' represents the fluctuating component of u_i. For the turbulence model, it is necessary to select a model for which the ratio μ_{turb}/μ reduces to a value ≤ 0.01 in the laminar flow regime. It has been demonstrated in [42] that the Shear Stress Transport turbulence model (SST) displays this characteristic. It represents a blending of two previously developed models, the κ-ε and κ-ω models. The quantity κ is the turbulence kinetic energy, and ω is the specific rate of turbulence dissipation. The κ-ε model has been demonstrated to give satisfactory descriptions of the velocity field at locations that are

distant from bounding walls, and the κ-ω model provides a good characterization of velocities in the near neighborhood of the wall.

The equations of the SST model are

$$\frac{\partial(\rho u_i \kappa)}{\partial x_i} = P_\kappa - \beta_1 \rho \kappa \omega + \frac{\partial}{\partial x_i}\left[\left(\mu + \frac{\mu_{turb}}{\sigma_\kappa}\right)\frac{\partial \kappa}{\partial x_i}\right] \tag{3.4}$$

$$\frac{\partial(\rho u_i \omega)}{\partial x_i} = A\rho S^2 - \beta_2 \rho \omega^2 + \frac{\partial}{\partial x_i}\left[\left(\mu + \frac{\mu_{turb}}{\sigma_\omega}\right)\frac{\partial \omega}{\partial x_i}\right] + 2\rho(1 - F_1)\frac{1}{\sigma_{\omega 2}\omega}\frac{\partial \kappa}{\partial x_i}\frac{\partial \omega}{\partial x_i} \tag{3.5}$$

The solution of Eqs. (3.4) and (3.5) yields the values of k and ω, which give the turbulent viscosity μ_{turb} from

$$\mu_{turb} = \frac{\alpha \rho \kappa}{\max(\alpha\omega, SF_{2)}} \tag{3.6}$$

Inspection of the foregoing equations reveals a set of six simultaneous non-linear partial differential equations. It is these characteristics that requires numerical solution.

The symbols that appear in the foregoing equations are defined as

A	model constant
F_1, F_2	blending functions in the SST model
P_k	production term for the turbulent kinetic energy
S	absolute value of the shear strain rate
u	local velocity
x_i	tensor coordinate direction
α	SST model constant
β_1, β_2	SST model constants

ω	specific rate of turbulence dissipation
μ	molecular viscosity
μ_{turb}	turbulent viscosity
σ	diffusion coefficient
ρ	fluid density

The heat transfer problem is governed by the First Law of Thermodynamics. For incompressible, constant property flow, the First Law can be written as

$$\rho c_p \frac{\partial(u_i T)}{\partial x_i} = \frac{\partial}{\partial x_i}\left[(k + k_{turb})\frac{\partial T}{\partial x_i}\right] \tag{3.7}$$

in which T is the temperature and c_p and k are, respectively, the specific heat and thermal conductivity. The quantity k_{turb} is designated as the turbulent thermal conductivity. Its value is closely linked to that of the turbulent viscosity by means of the turbulent Prandtl number

$$Pr_{turb} = \frac{c_p \mu_{turb}}{k_{turb}} \tag{3.8}$$

Extensive experience has shown that a constant value of $Pr_{turb} = 0.9$ gives rise to highly accurate heat transfer results.

3.4 NUMERICAL SIMULATION

The solution of the foregoing equations was facilitated by the use of ANSYS CFX 14.0 software. A necessary prerequisite for the numerical simulation is the selection of the space in which the solution is to be sought. That space is normally referred to as the solution domain. In the present instance, the upstream portion of the solution domain extends from the inlet of the rectangular duct to the cross section of the slot in the orifice plate situated at the exit of the duct. The solution domain also extends into the expansion space.

To illustrate that portion of the solution domain, Figs. 3.3(a) and (b) have been prepared. Part (a) of the figure is a side view of the solution domain in the expansion space. The downstream end of the domain coincides with the front face of the heat transfer plate when such a plate is in place. For those cases in which fluid flow only was investigated, the downstream end was situated at a value of *x*/*b* specified for each such case. Note that the solution domain is extended back from the plane of the duct exit. This extension was made based on the expectation at the emerging jet would entrain upstream fluid. A pictorial view of the downstream portion of the solution domain is exhibited in Fig. 3.3(b).

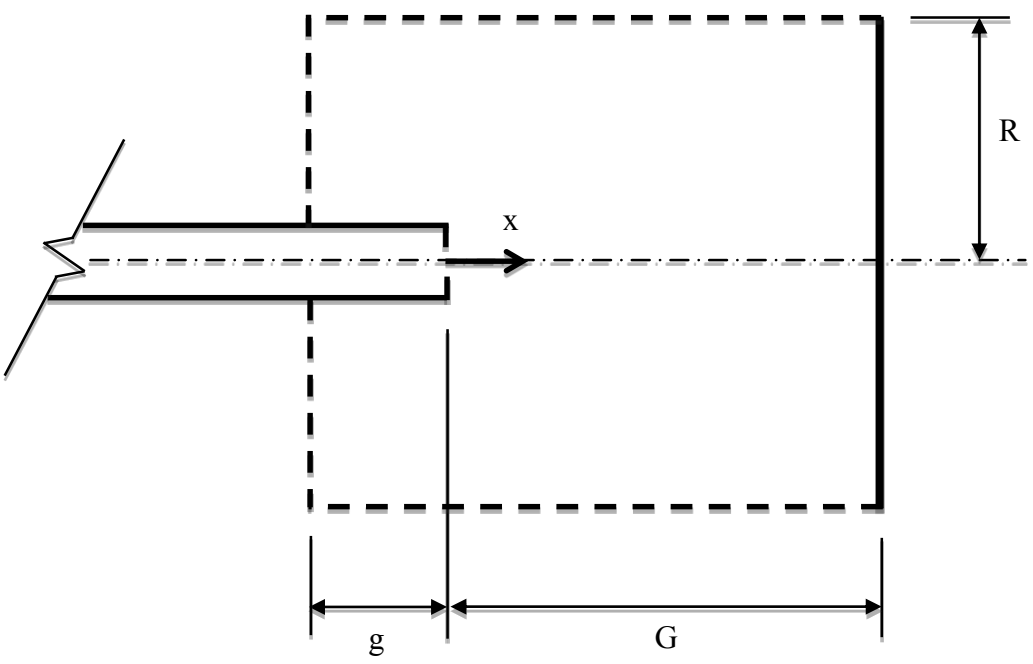

(a)

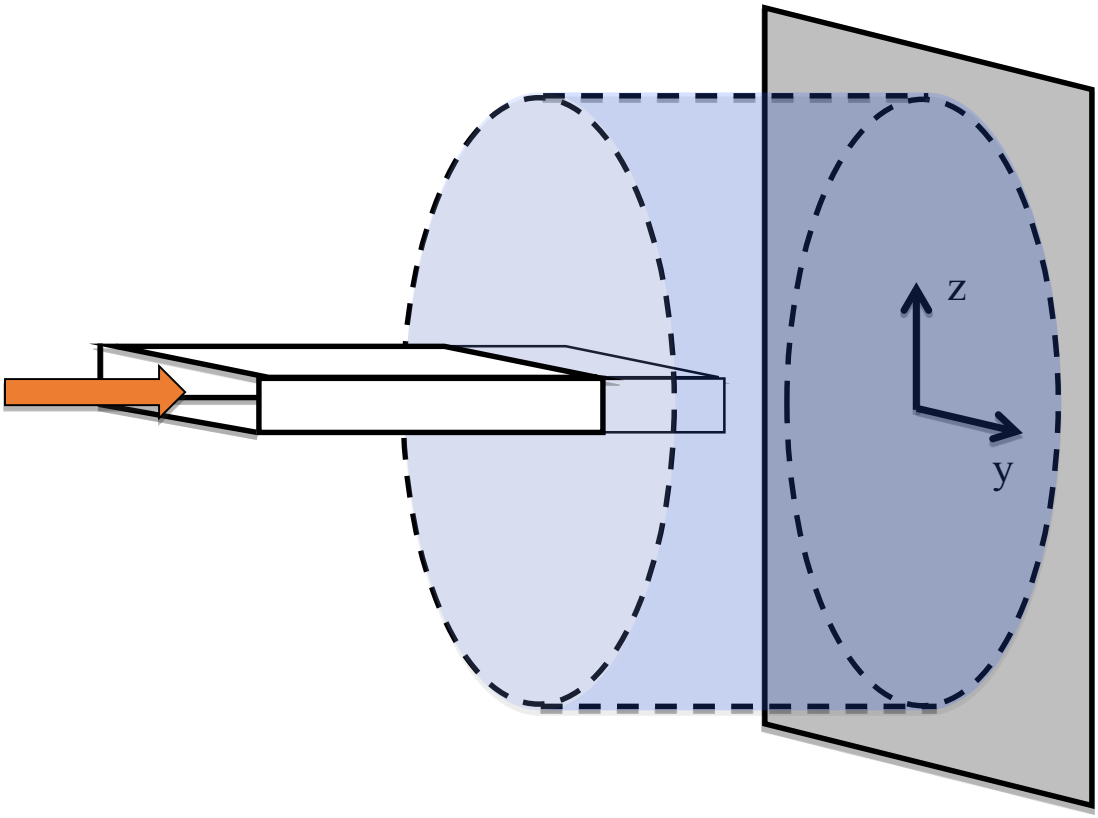

(b)

Fig. 3.3. Views of the solution domain: (a) side view and (b) pictorial view.

Since there is no heat transfer to or from the fluid passing through the duct, the thickness of the duct walls is immaterial. Therefore, the walls and the orifice plate are modeled as surfaces of zero thickness.

The discretization of the partial differential equations was achieved by means of the finite-volume method as embodied in ANSYS CFX 14.0 software. A key issue with regard to the accuracy of the numerical solutions is mesh independence. In this context, independence refers both to the number of nodes and to their deployment. An all-encompassing figure, Fig. 3.4(a)-(f), has been prepared to display various features of the mesh. That figure exhibits the mesh corresponding to the least populated (~eight million nodes) of the various meshes that were employed. This choice was made because the more populated meshes (14, 20, and 24 million nodes) are so dense as to be difficult to display.

The (a) part of Fig. 3.4 is a silhouette of the mesh as a whole, so dense that it appears as a continuum. Part (b) of the figure displays a representative longitudinal cross section of the mesh encompassing the downstream portion of the duct and the expansion space. An enlarged view of the mesh in the expansion space that is downstream of the duct exit is shown in Part (c). Mesh independence was achieved using the various nodal populations mentioned in the foregoing.

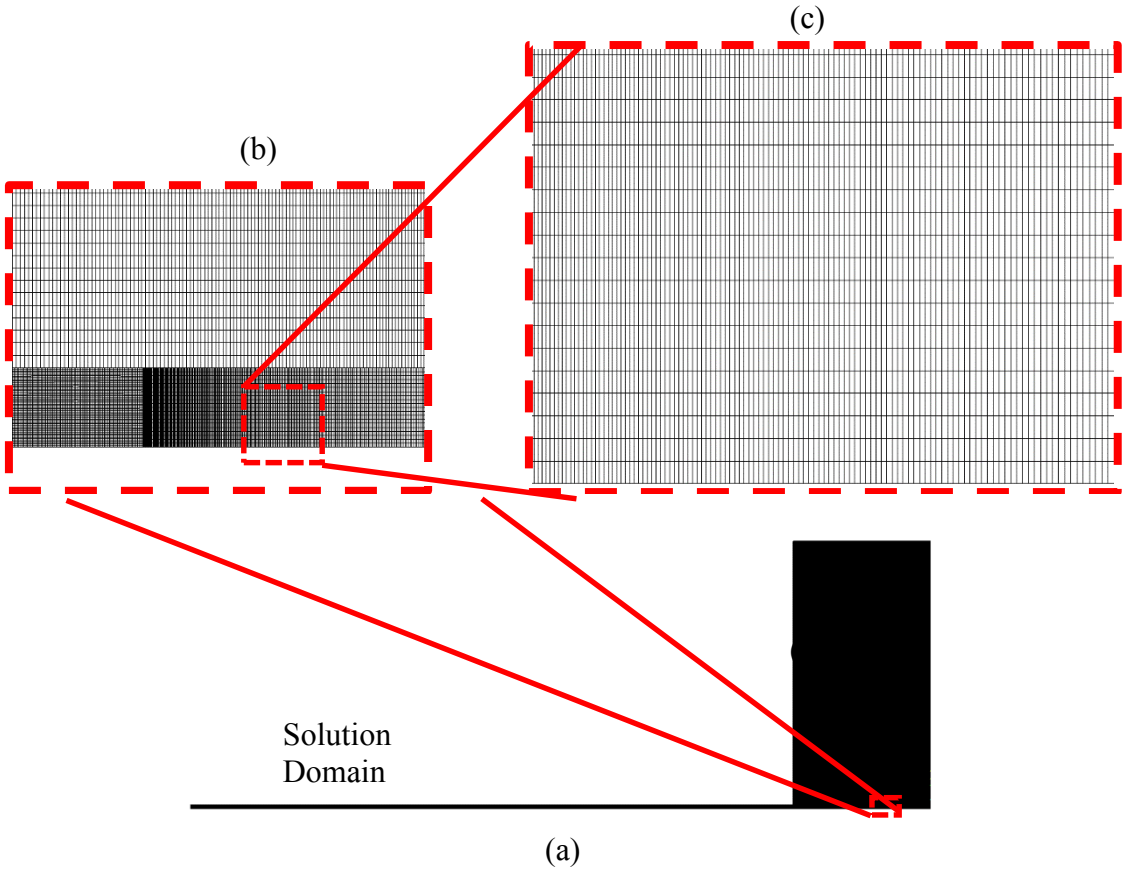

Fig. 3.4. Illustrative views of the numerical mesh.

To enhance the generality of the results, the governing equations were recast in to non-dimensional form. This was accomplished by employing the definitions

$$x', y', z' = \frac{x,y,z}{b} \tag{3.9}$$

$$u', v', w' = \frac{u,v,w}{U}$$

$$L', S', s', \ldots = \frac{L,S,s}{b}$$

$$\rho = 1$$

$$Re = \frac{Ub}{\nu}$$

$$\mu = \frac{1}{Re}$$

$$p' = \frac{p}{\rho U^2}$$

$$\theta = \frac{T - T_{Inflow}}{T_{Plate} - T_{Inflow}} \tag{3.10}$$

$$Pr = \frac{c_p \mu}{k}$$

$$c_p = 1$$

$$k = \frac{1}{RePr}$$

To elucidate the foregoing notation, it is convenient to separately focus on the fluid flow equations and the heat transfer equation. In their transformed versions, Eqs. (3.1), (3.2), and (3.7) become

$$u_i' \left(\frac{\partial u_j'}{\partial x_i'}\right) = -\frac{\partial p'}{\partial x_j'} + \frac{1}{Re}\frac{\partial}{\partial x_i'}\left[\left(1 + \frac{\mu_{turb}}{\mu}\right)\frac{\partial u_j'}{\partial x_i'}\right] \tag{3.11}$$

$$\frac{\partial u_j'}{\partial x_i'} = 0 \tag{3.12}$$

$$\frac{\partial}{\partial x_i'}(u_i'\theta) = \frac{1}{RePr}\frac{\partial}{\partial x_i'}\left[\left(1 + \frac{k_{turb}}{k}\right)\frac{\partial \theta}{\partial x_i'}\right] \tag{3.13}$$

To complete the problem definition, it is necessary to specify the boundary conditions. For the velocity problem, all components are zero on all solid surfaces. At the duct inlet,

$$u' = 1 \tag{3.14}$$

The other boundaries of the solution domain are treated either as openings or symmetry planes. An opening is a surface across which a fluid may pass in either direction, in or out. The pressure on the outfacing side of an opening must be specified. In the present instance, the gauge pressure was specified as zero. On the other hand, a symmetry plane precludes fluid flow across it, and pressure need not be specified. With regard to heat transfer, the dimensionless temperature θ at the duct inlet is zero. For those cases involving a heat transfer plate, the plate temperature is $\theta = 1$. The duct walls, as well as the orifice plate, were specified as adiabatic. At surfaces that are designated as openings, different thermal boundary conditions are appropriate depending on whether fluid passes from the interior of the solution domain to the exterior and vice-versa. If the fluid is passing out of the solution domain, the weakest reasonable thermal boundary condition is applied, which is $\partial^2 T/\partial n^2$, where n is in the normal direction. On the other hand, if fluid passes into the solution domain, it is necessary to specify the temperature just outside of the surface. In the present instance, that temperature is $\theta = 0$.

3.4.1 Fluid Flow Cases

The results can be categorized as those which relate strictly to fluid flow and those which are strictly related to heat transfer. The fluid flow results will be presented first, followed by those for heat transfer. To organize the presentation of the results, Tables 3.1 and 3.2 have been prepared to display totality of the considered cases. The first of these tables defines the operating parameters for those cases which were investigated in the absence of

the heat transfer plates, while the second table corresponds to the cases where the plates were in place. All told, solutions were obtained for 48 discrete cases.

Table 3.1. Listing of fluid flow cases in the absence of heat transfer plates

Case	**Re**	**Aspect Ratio**	**Blockage Ratio**					
1	600	5	0	0.1	0.2	0.3	0.4	0.5
2	1200	5	0	0.1	0.2	0.3	0.4	0.5
3	550	10	0	0.1	0.2	0.3	0.4	0.5
4	1100	10	0	0.1	0.2	0.3	0.4	0.5

Table 3.2. Listing of fluid flow cases in the presence of heat transfer plates

Case	**Re**	**Aspect Ratio**	**Blockage Ratio**			x_{plate}/b	
5	550	10	0	0.3	0.5	10	25
6	1100	10	0	0.3	0.5	10	25
7	600	5	0	0.3	0.5	10	25
8	1200	5	0	0.3	0.5	10	25

In the tables, the quantities aspect ratio and blockage ratio are defined as

$$Aspect\ Ratio = \frac{H}{W} = \frac{a}{b} \tag{3.15}$$

$$Blockage\ Ratio = 1 - \frac{ab}{HW} \tag{3.16}$$

Where the geometric quantities are defined in Fig. 3.2(a).

The first set of fluid flow results are focused on the axis-switching phenomenon.

3.4.2 Images of Evolving Velocity Field

The evolution of the velocity field downstream of the jet exit is displayed in a succession of cross sections. Each such display consists of a color contour diagram. The displayed diagram is actually a quarter of the cross section in question and reflects the symmetry of the situation. The color contour diagrams exhibit values of the dimensionless quantity u/U, where u is the x-direction velocity and U is the mean velocity in upstream duct from which the jet emerges.

Each case was defined by a Reynolds number, an aspect ratio, and a blockage ratio. For each such case, velocity contour diagrams were extracted from the numerical solutions at locations x/b = 1, 2, …, 10, 15, 25, …, 65. This assemblage of information, if fully presented, would have required a minimum of 48 pages even after the omission of half of the indicated x/b locations. It was deemed unreasonable to use so much space for these results when there are other types of important results which need to be presented. In finding a suitable balance between the presentation of the most important information and the realistic use of space, it was decided to select the minimum number of x/b locations that would convey the essential trends.

3.4.2.1 Case 1: Evolving velocity field

The starting point of the presentation follows the order of the listing in Table 3.1, specifically for Re = 600 and aspect ratio = 5. These results are displayed in Fig. 3.5(a)-(f), respectively for blockage ratios of 0, 0.1, …, 0.5. For each blockage ratio, three images are

shown in a horizontal strip. The unblocked case is regarded as a baseline against which the various partially blocked cases are compared. The three images in each horizontal strip correspond to *x*/*b* values = 1, 10, and 35, from left to right. For reference purposes, each of the images contains an outline of the slot from which the jet emerged.

An overall inspection of Figs. 3.5 shows that the shape of the jet metamorphoses from a rectangular slot to a circle. This process is generally characterized by the term *axis switching*. In all cases, this geometric switch is virtually complete at the distance *x*/*b* = 10. As expected, the jet spreads continuously and experiences a decrease in its velocity.

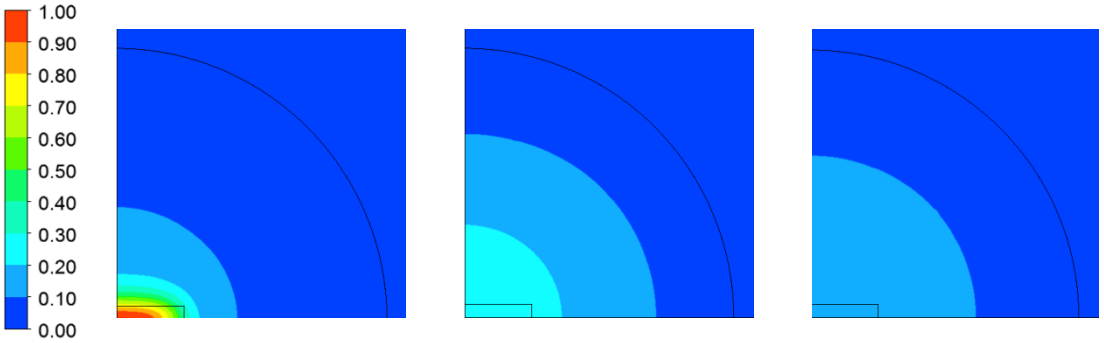

1 *x*/*b* 10 *x*/*b* 35 *x*/*b*

(a) Re = 600, aspect ratio of 5, 0% blockage

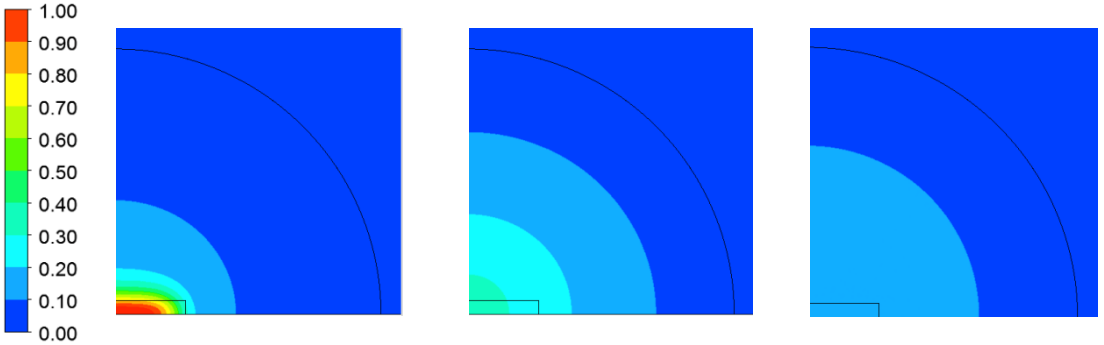

1 *x*/*b* 10 *x*/*b* 35 *x*/*b*

(b) Re = 600, aspect ratio of 5, 10% blockage

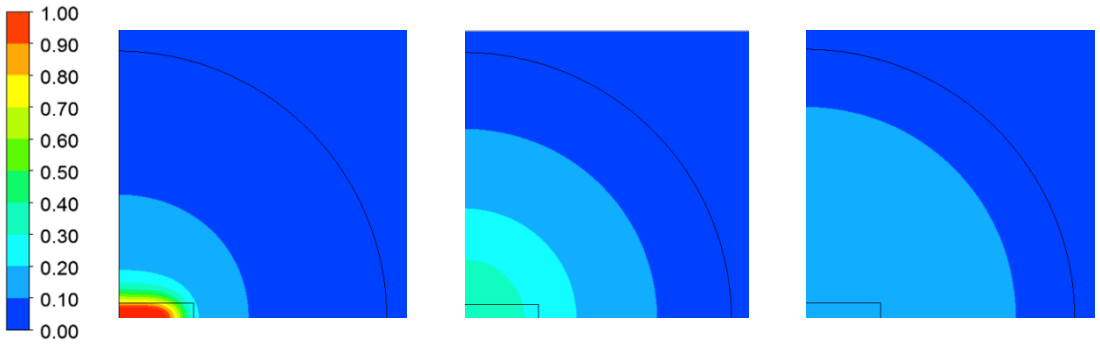

1 *x*/*b* 10 *x*/*b* 35 *x*/*b*

(c) Re = 600, aspect ratio of 5, 20% blockage

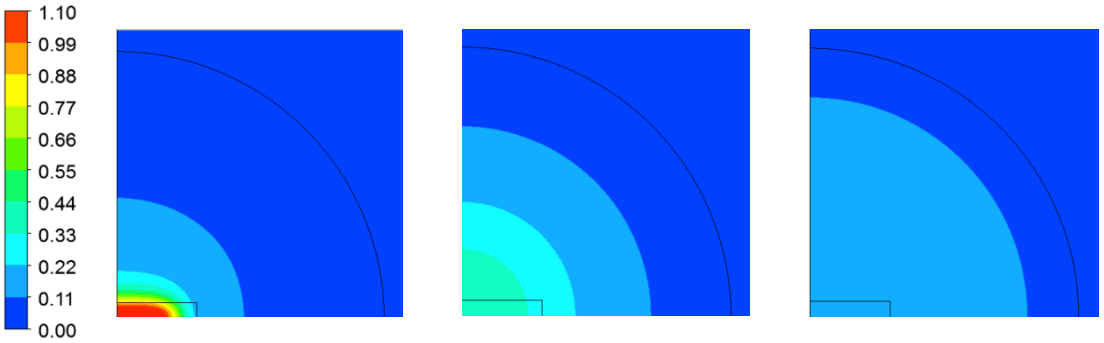

1 *x*/*b* 10 *x*/*b* 35 *x*/*b*

(d) Re = 600, aspect ratio of 5, 30% blockage

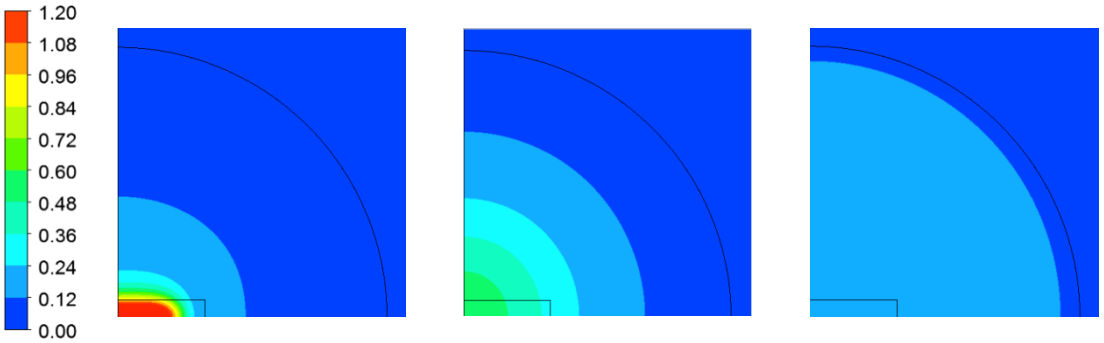

1 *x*/*b* 10 *x*/*b* 35 *x*/*b*

(e) Re = 600, aspect ratio of 5, 40% blockage

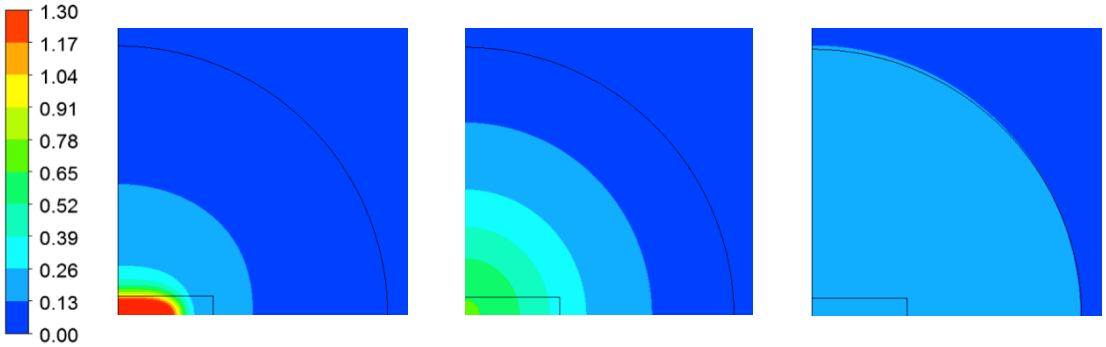

1 *x*/*b* 10 *x*/*b* 35 *x*/*b*

(f) Re = 600, aspect ratio of 5, 50% blockage

Fig. 3.5. Evolving jet cross sections for the case Re = 600 and aspect ratio = 5. Each horizontal strip of images corresponds to a given blockage ratio, with zero blockage for the first strip and 50% blockage for the last strip.

3.4.2.2 Case 2: Evolving velocity field

Information similar to that conveyed in Fig. 3.5 is presented in Fig. 3.6 for the case of Re = 1200 and an aspect ratio of 5. The results for the various blockage ratios from 0 to 50% are shown respectively in the (a)-(f) parts of the figure.

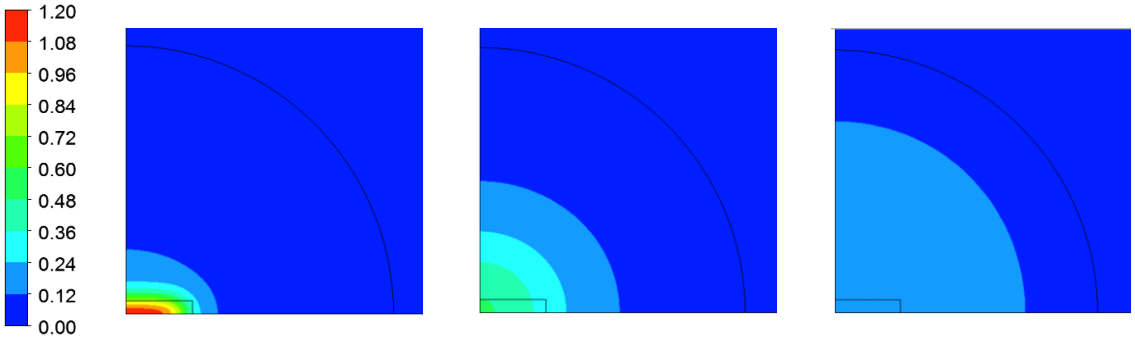

1 *x*/*b* 10 *x*/*b* 35 *x*/*b*

(a) Re = 1200, aspect ratio of 5, 0% blockage

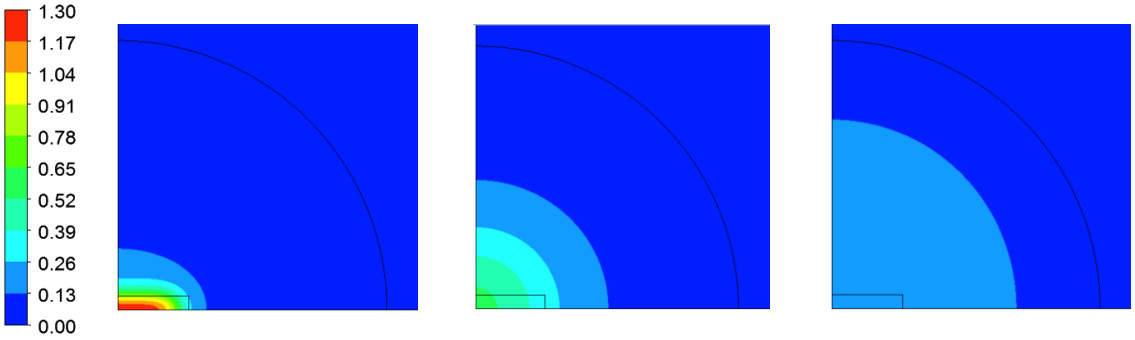

1 *x*/*b* 10 *x*/*b* 35 *x*/*b*

(b) Re = 1200, aspect ratio of 5, 10% blockage

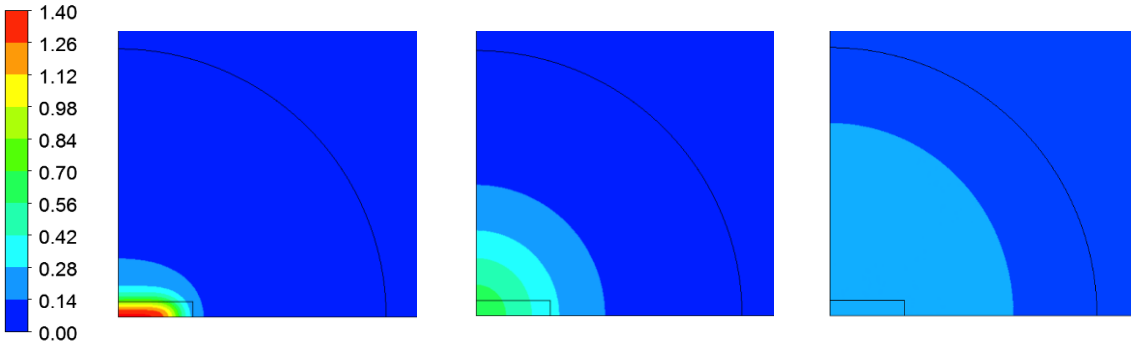

1 *x*/*b* 10 *x*/*b* 35 *x*/*b*

(c) Re = 1200, aspect ratio of 5, 20% blockage

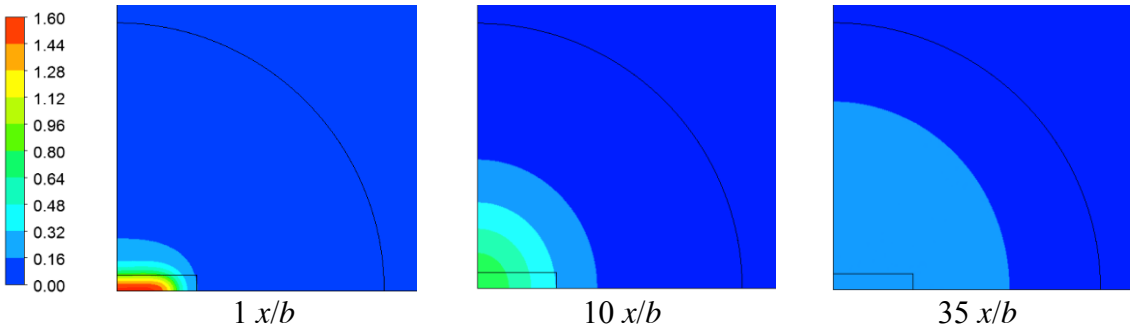

1 *x*/*b* 10 *x*/*b* 35 *x*/*b*

(d) Re = 1200, aspect ratio of 5, 30% blockage

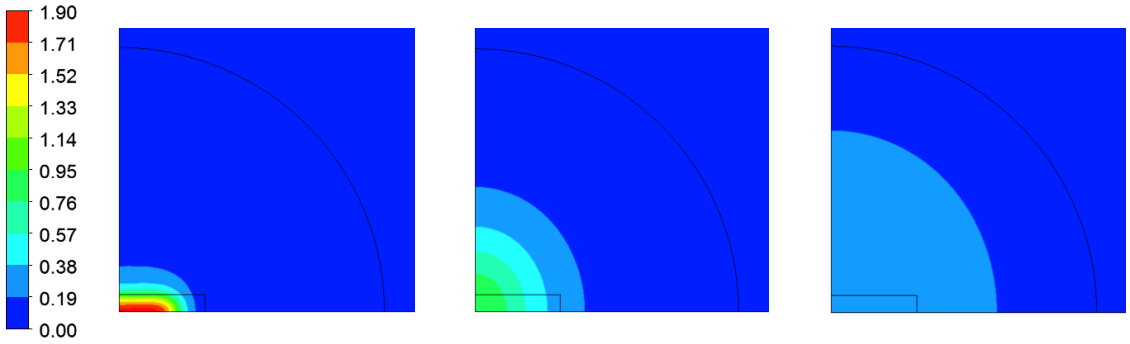

1 *x*/*b* 10 *x*/*b* 35 *x*/*b*

(e) Re = 1200, aspect ratio of 5, 40% blockage

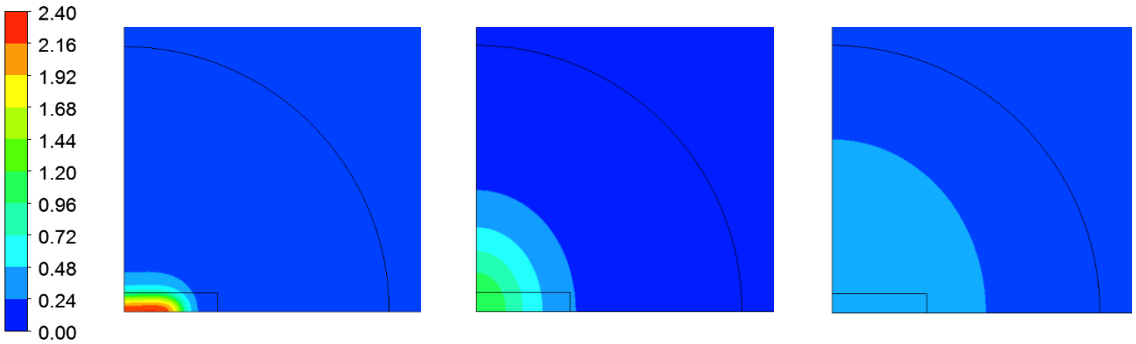

1 *x*/*b* 10 *x*/*b* 35 *x*/*b*

(f) Re = 1200, aspect ratio of 5, 50% blockage

Fig. 3.6. Evolving jet cross sections for the case Re = 1200 and aspect ratio = 5. Each horizontal strip of images corresponds to a given blockage ratio, with zero blockage for the first strip and 50% blockage for the last strip.

An overall view of Fig. 3.6 suggests a switching pattern similar to that previously displayed in Fig. 3.5. Closer inspection, however, reveals minor differences in detail. For the larger blockage ratios displayed in Fig. 3.6(e) and (f), there is a tendency for a non-circular cross sectional pattern which did not appear in Fig. 3.5.

3.4.2.3 Case 3: Evolving velocity field

The next presentation, which follows the ordering in Table 3.1, is the case of Re = 550 and an aspect ratio of 10. These results are displayed in Fig. 3.7(a)-(f). The 10:1 slot aspect

ratio which characterizes these results more strongly affects the developmental and switching pattern of the jets than did the 5:1 aspect ratio. It can be seen that at the 10 *x/b* displacement from the jet exit, a true circular cross section is not achieved until the 50% blockage ratio is attained. On the other hand, at the larger downstream displacement, *x/b* = 35, an opposite trend is encountered. For the blockage ratio of zero, the jet cross section is a perfect circle. As the blockage ratio increases, there is a progressive departure from circularity.

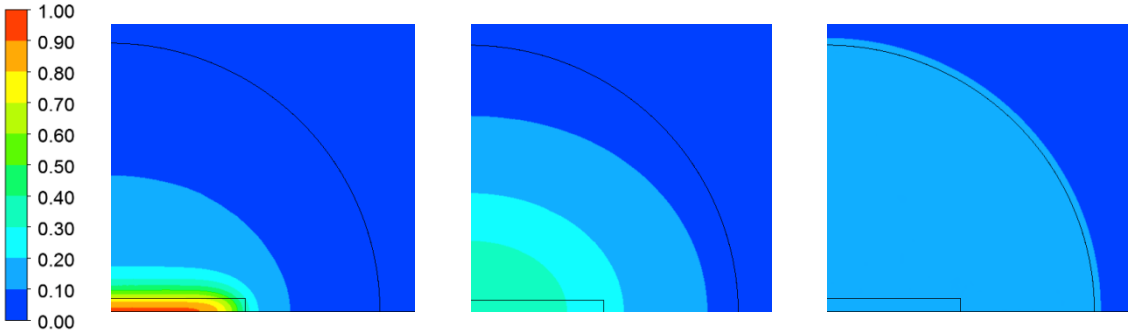

1 *x/b* 10 *x/b* 35 *x/b*

(a) Re = 550, aspect ratio of 10, 0% blockage

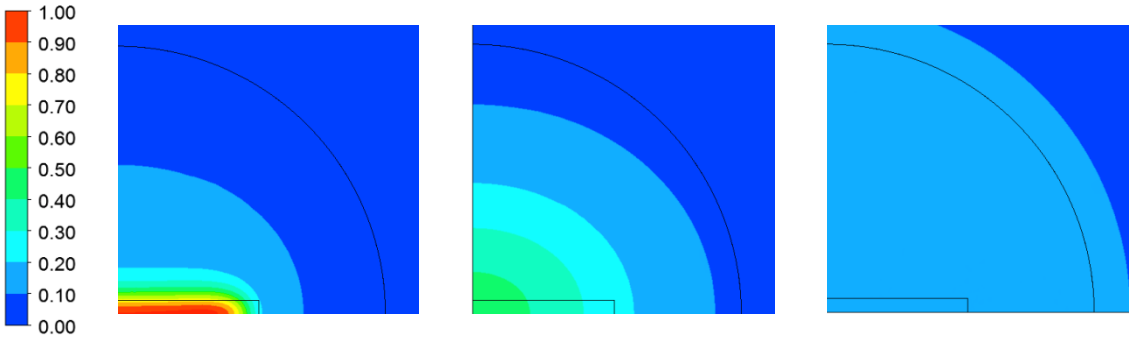

1 *x/b* 10 *x/b* 35 *x/b*

(b) Re = 550, aspect ratio of 10, 10% blockage

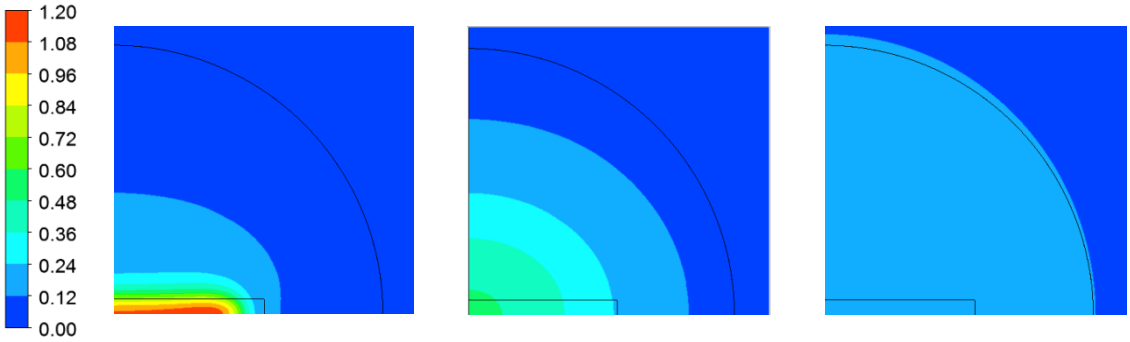

1 *x*/*b* 10 *x*/*b* 35 *x*/*b*

(c) Re = 550, aspect ratio of 10, 20% blockage

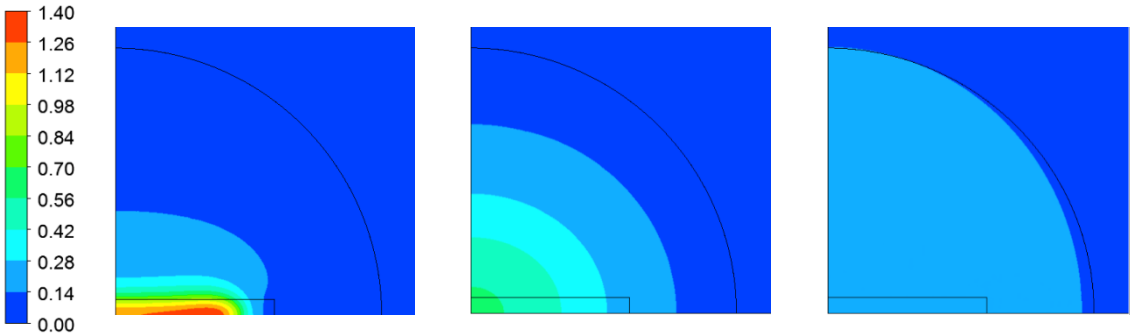

1 *x*/*b* 10 *x*/*b* 35 *x*/*b*

(d) Re = 550, aspect ratio of 10, 30% blockage

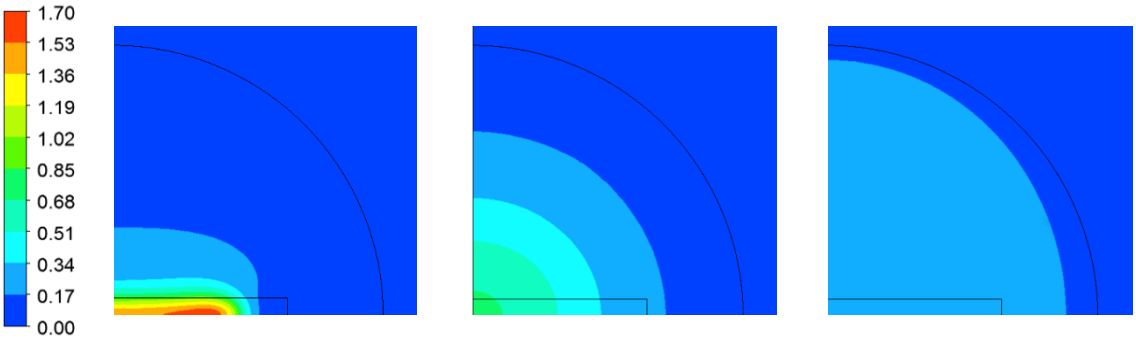

1 *x*/*b* 10 *x*/*b* 35 *x*/*b*

(e) Re = 550, aspect ratio of 10, 40% blockage

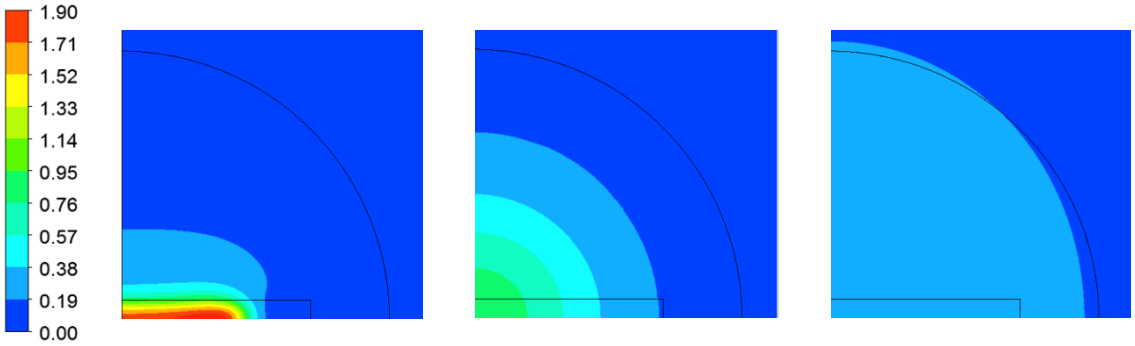

1 *x/b* 10 *x/b* 35 *x/b*

(f) Re = 550, aspect ratio of 10, 50% blockage

Fig. 3.7. Evolving jet cross sections for the case Re = 550 and aspect ratio = 10. Each horizontal strip of images corresponds to a given blockage ratio, with zero blockage for the first strip and 50% blockage for the last strip.

3.4.2.4 Case 4: Evolving velocity field

The last case of the current series, according to Table 3.1, is characterized by a Reynolds number of 1100 and a slot aspect ratio of 10. The axis-switching phenomenon is more pronounced for this case then for its predecessors because of its relatively high Reynolds number and larger slot aspect ratio. This presentation is identical in form to the foregoing displays and is exhibited in Fig. 3.8.

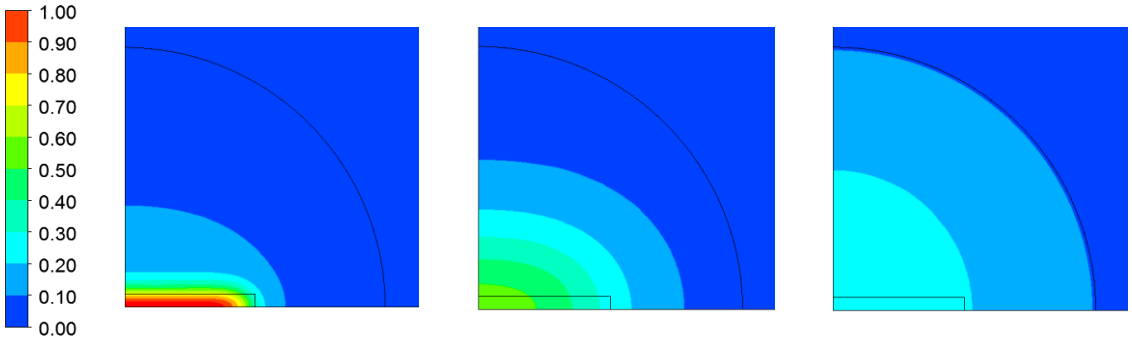

1 *x/b* 10 *x/b* 35 *x/b*

(a) Re = 1100, slot aspect ratio of 10, 0% blockage

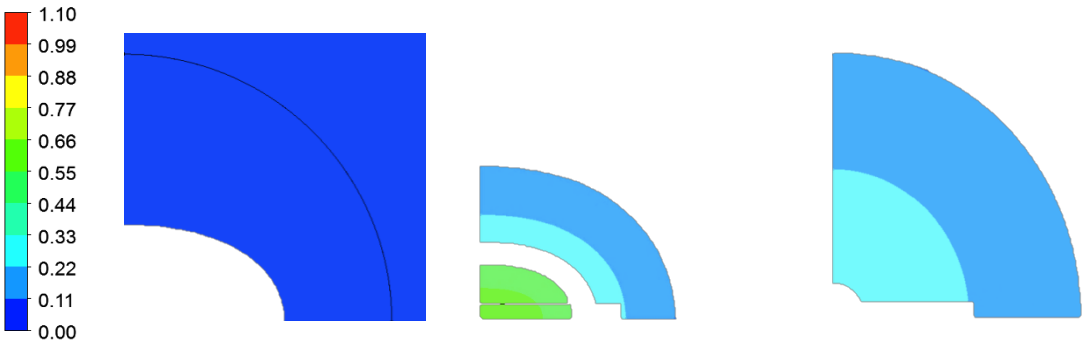

1 *x*/*b* 10 *x*/*b* 35 *x*/*b*

(b) Re = 1100, slot aspect ratio of 10, 10% blockage

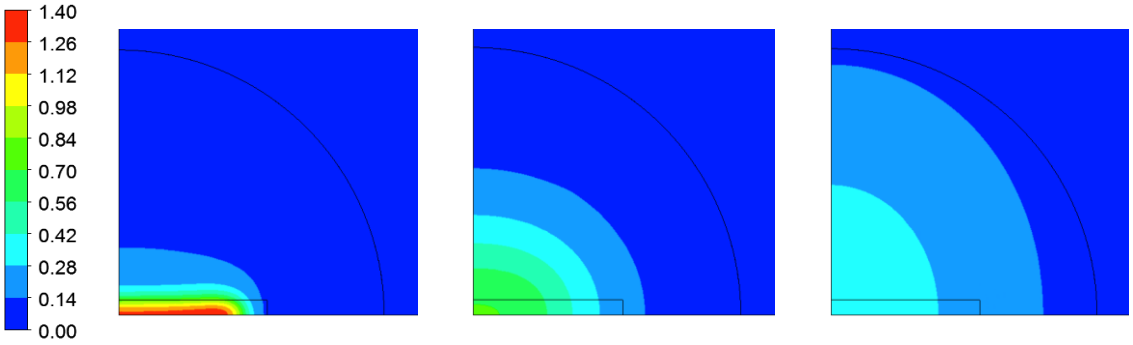

1 *x*/*b* 10 *x*/*b* 35 *x*/*b*

(c) Re = 1100, slot aspect ratio of 10, 20% blockage

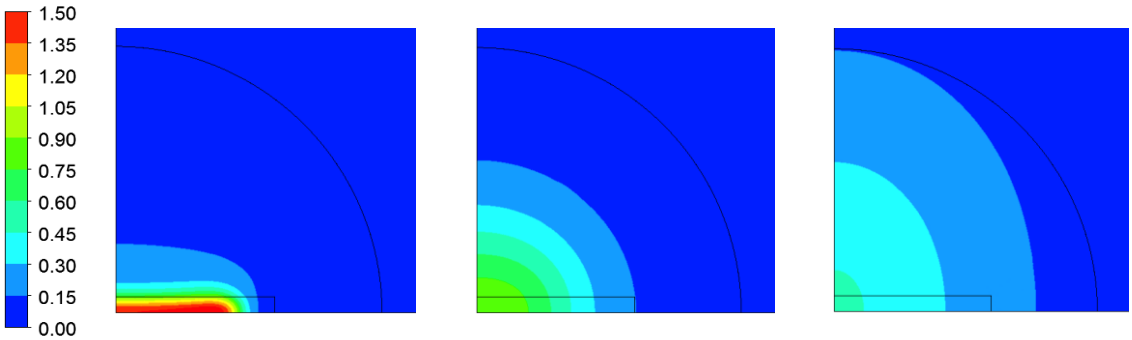

1 *x*/*b* 10 *x*/*b* 35 *x*/*b*

(d) Re = 1100, slot aspect ratio of 10, 30% blockage

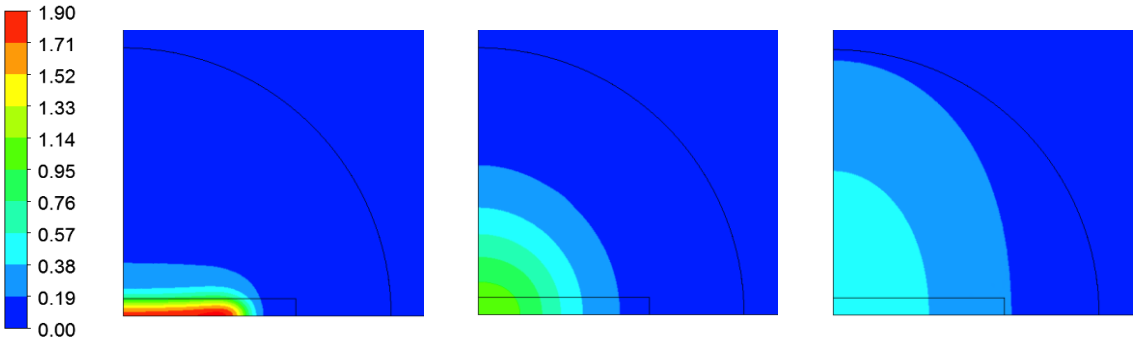

1 *x*/*b* 10 *x*/*b* 35 *x*/*b*

(e) Re = 1100, slot aspect ratio of 10, 40% blockage

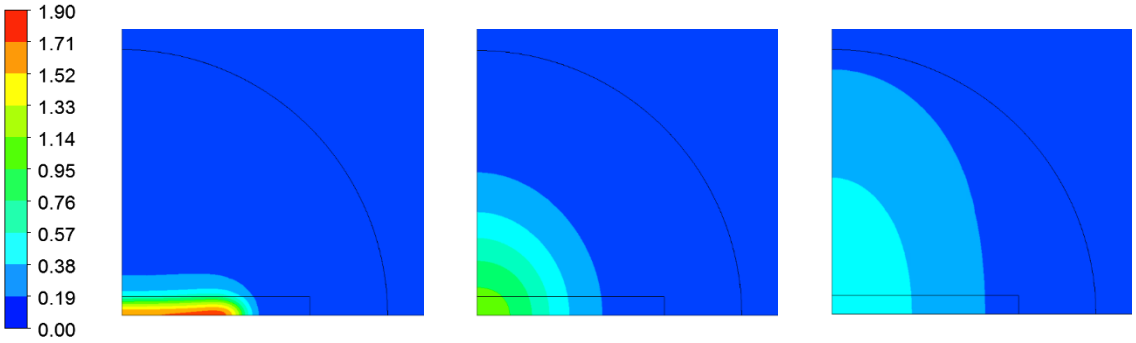

1 *x*/*b* 10 *x*/*b* 35 *x*/*b*

(f) Re = 1100, slot aspect ratio of 10, 50% blockage

Fig. 3.8. Evolving jet cross sections for the case Re = 1100 and aspect ratio = 10. Each horizontal strip of images corresponds to a given blockage ratio, with zero blockage for the first strip and 50% blockage for the last strip.

More intense axis switching is evident from an examination of Fig. 3.8 relative to what was displayed in the earlier figures. If focus is first directed to the results at x/b = 10, starting at the blockage ratio of zero and proceeding to larger blockages, it is seen that the first results reflect the horizontal skewness of the original jet while the later results switch to a elongation in the vertical direction. At the 35 x/b location, the vertical elongation is already seen for the no-blockage case and is accentuated as the blockage increases.

3.4.2.5 Axis-switching phenomena

A quantitative metric of axis switching is provided by an appropriately defined *velocity field aspect ratio*. This quantity is the ratio of the size of the velocity field in the *y*-direction to the size of the velocity field in the *z*-direction (horizontal to vertical directions in terms of Fig. 3.2). This ratio is presented in Fig. 3.9 where it is plotted as a function of the distance downstream of the duct exit. The results displayed in this figure correspond to a slot aspect ratio of 10, a Reynolds of 1100, and blockage ratios of 0, 30, and 50%. The figure is subdivided into a main portion which spans the range of *x*/*b* where axis switching occurs and an inset which magnifies the results for *x*/*b* values located immediately downstream of the duct exit.

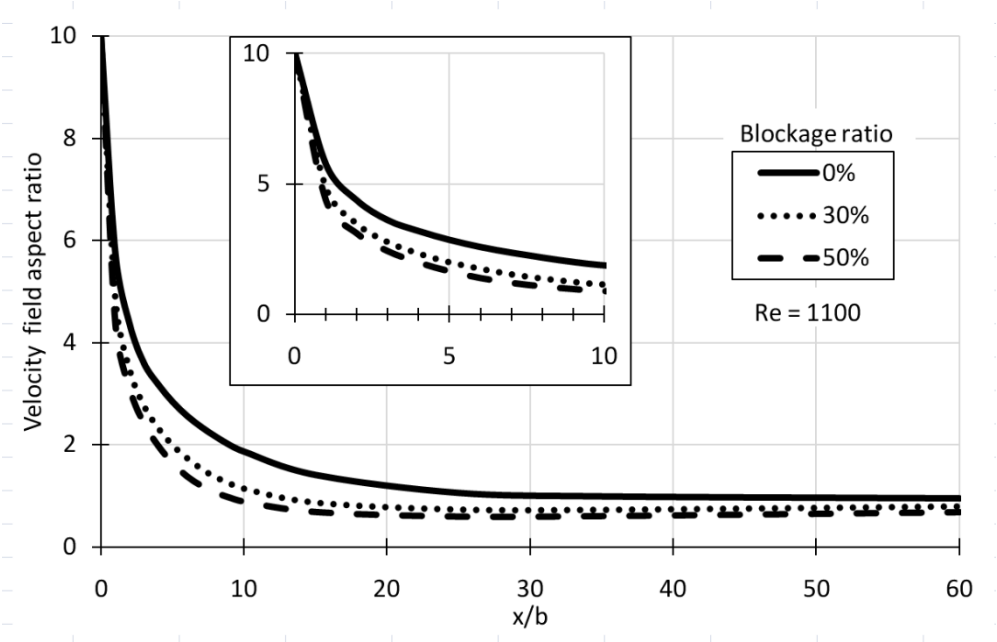

Fig. 3.9. Demonstration of axis-switching phenomenon. Slot aspect ratio of 10:1.

It can be seen from the figure that the initial velocity field deployment (predominately horizontal in the present coordinates) experiences a very rapid change in axis orientation. This reorientation can readily be recognized by noting that at *x*/*b* ~ 10, the 30 and 50% blockage cases appear to have lost their memories of their initial velocity field aspect ratios and have become circular. Only for the zero percent blockage case, for which the aspect ratio is two at *x*/*b* = 10, is there a lingering memory of the original 10:1 aspect ratio.

An alternative viewpoint of the results of Fig. 3.9 is conveyed in Fig. 3.10. In the latter, the velocity field aspect ratio is plotted as a function of the blockage ratio for two specific downstream locations, x/b = 10 and 35. From the information displayed in Fig. 3.9, only a minor variation of the velocity field aspect ratio is to be expected between these two downstream locations. Therefore, the true focus of Fig. 3.10 is to present the sensitivity of the results to quantities such as blockage ratio, Reynolds number, and initial slot aspect ratio. The figure contains both upper and lower parts, respectively for slot aspect ratios of 10:1 and 5:1. An overall inspection of the figure indicates that the effect of varying blockage ratio is accentuated for the 10:1 slot aspect ratio.

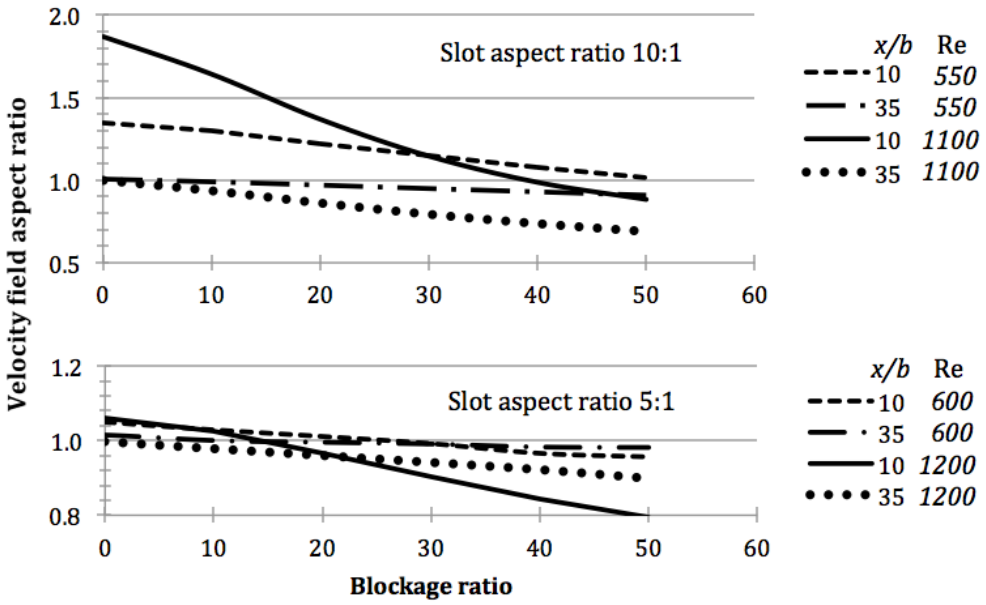

Fig. 3.10. Variation of the velocity field aspect ratio with the blockage ratio, slot aspect ratio, Reynolds number, and downstream distance.

Of particular interest with regard to the results presented in Fig. 3.11 is the extent to which the velocity field aspect ratios differ from their initial values of 5:1 and 10:1. For the most part, the velocity field aspect ratios take on values in the neighborhood of one, which are indicative of a circular velocity field. The cases which were initiated with a 10:1 aspect ratio slot have a somewhat keener memory of their origins when viewed at x/b = 10. These

same cases have experienced amnesia by x/b = 35. The velocity-field aspect ratio results that correspond to the cases initiated from a 5:1 aspect ratio slot show little relationship to their original shape.

3.4.2.6 A detailed display of velocity field evolution

Attention will now be turned to a more complete presentation of the evolving velocity field for the highest blockage case. This display conveys all details of the morphing shape of the velocity field. Here, the greatest tendency for axis switching is in evidence and as is the vertical skewness. For locations up to x/b = 9, the legacy of the initial jet cross section persists. Beyond that point, there is a greater and greater tendency toward vertical skewness. For x/b = 45, 55, and 65, the jet cross section appears to have achieved a terminal value.

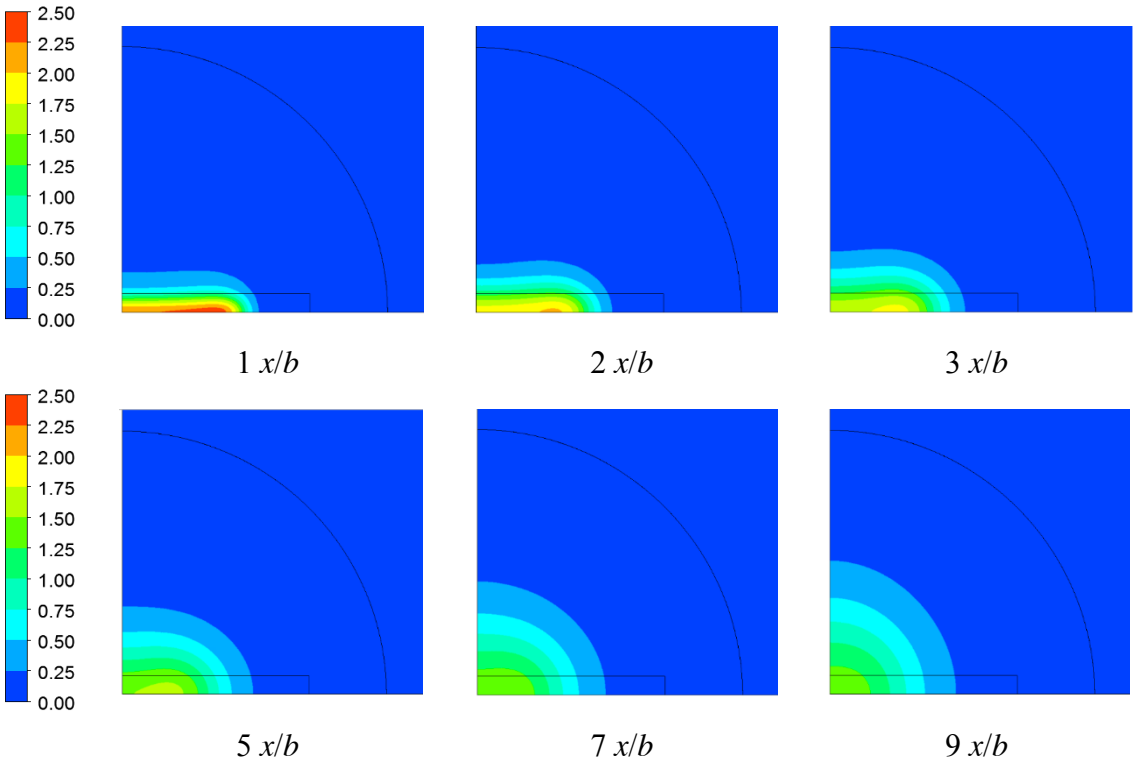

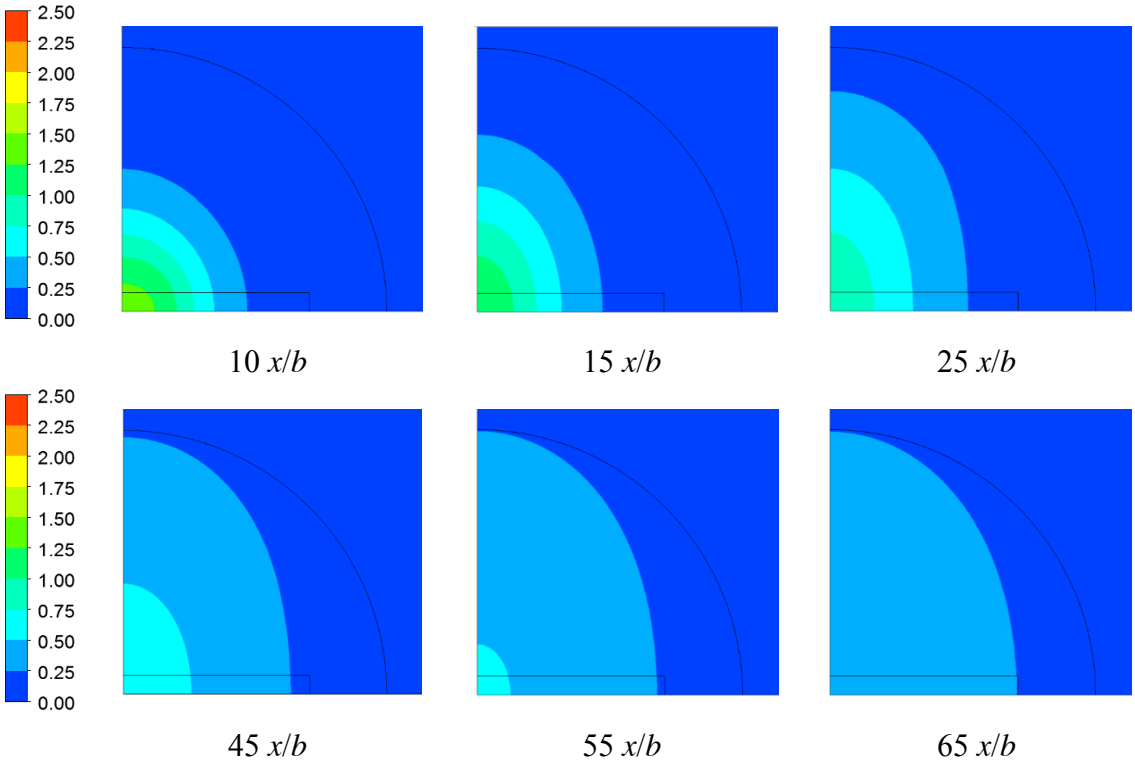

Fig. 3.11. Detailed presentation of evolving jet cross sections for the case Re = 1100 and aspect ratio = 10 and a blockage of 50%.

3.5 HEAT TRANSFER RESULTS AND DISCUSSION

The presentation of the heat transfer results will be separated into two categories. The first category encompasses heat transfer magnitudes which can be used directly for design. The second includes color contour diagrams demonstrating the magnitudes of the heat fluxes distributed over the surfaces of the impinged plates.

The average heat transfer coefficients were evaluated from the definition

$$\bar{h} = \frac{Q}{\Delta T(ab)} \tag{3.17}$$

where Q is the rate of heat transfer on the impingement surface, ΔT is the temperature difference between the impinging fluid and the plate surface, and the quantity (ab) is the cross-sectional area of the aperture in the orifice plate. In other situations, the area used in the definition of the average heat transfer coefficient is that of the surface through which heat is flowing. In the case of the impinging jet, the jet cross section varies with the distance of the impingement plate from the duct exit, as does the impingement surface area for heat transfer. Since the latter depends on the dynamics of the situation, its value is not known *a priori* and, therefore, it is not suitable for use in the definition of $\bar{h}$. On the other hand, since the jet cross section at the orifice aperture is a known quantity, its use in the definition of $\bar{h}$ was deemed suitable.

The results for the average heat transfer coefficient are presented in terms of a Nusselt number $\bar{h}b/k$. All of the numerical information corresponds to a Prandtl number Pr = 0.7. The variation of the Nusselt number as a function of the downstream location of the impingement plate is presented in Figs. 3.12 and 2.13, respectively for the original slot jet aspect ratios of 5:1 and 10:1. Each figure contains a pair of curve clusters, each distinguished by line weight, that correspond respectively to the Reynolds numbers in the legends. Both figures indicate that the Nusselt numbers increase with increasing distance of the impingement plate from the jet origin, regardless of the Reynolds number. This outcome is the result of two competing factors. With increasing downstream distance, the velocity magnitude necessarily decreases. On the other hand, the size of the jet impingement zone on the heat transfer plate increases as the downstream distance increases. Between these diverging effects, the impingement zone size proves to be of greater importance.

The figures also show that the blockage ratio plays a significant role with respect to the value of the Nusselt number, giving rise to significant increases with greater blockages. As expected, the higher the Reynolds number, the higher is the Nusselt number.

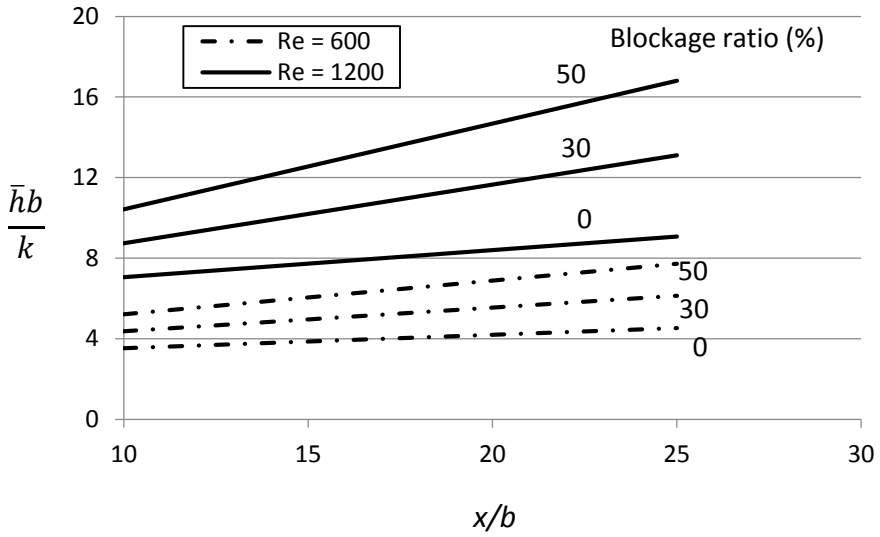

Fig. 3.12. Dependence of the average heat transfer coefficients on the distance of the heat transfer plate from the jet origin, on the blockage ratio, and on the Reynolds number. The slot aspect ratio at the jet origin is 5:1.

The trends outlined in the foregoing apply to both Figs. 3.7 and 3.8. It may appear from a comparison of the two figures that the original 5:1 jet-aspect-ratio case gives rise to higher Nusselt numbers than does the original 10:1 aspect ratio. This observation must be regarded with caution in view of the definition of $\bar{h}$ (Eq. (3.10)). As discussed in the foregoing, the choice of (*ab*) in the definition departs from the standard practice, but is deemed to be the most rational choice. The use of the area (*ab*) in the definition of the heat transfer coefficient is believed to be the reason for the ordering of the results for the 5:1 and 10:1 aspect ratios.

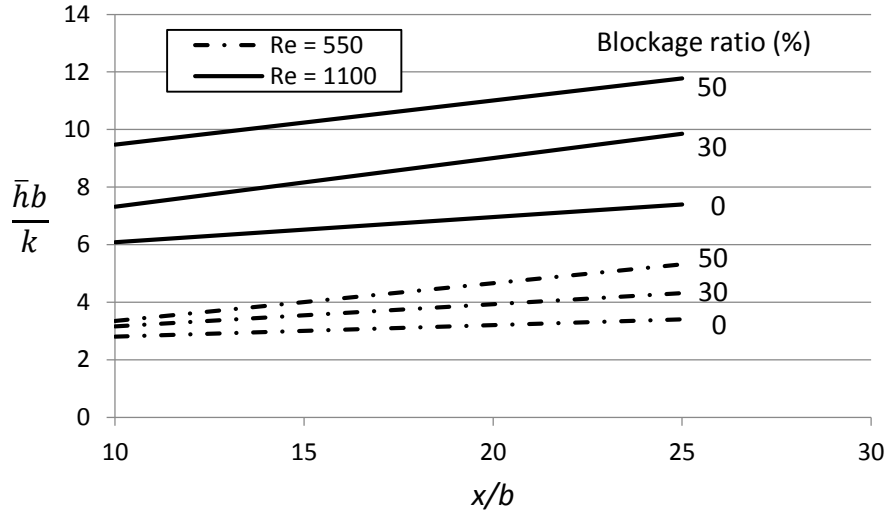

Fig. 3.13. Dependence of the average heat transfer coefficients on the distance of the heat transfer plate from the jet origin, on the blockage ratio, and on the Reynolds number. The slot aspect ratio at the jet origin is 10:1.

An alternative presentation of the average Nusselt number results featuring the effect of blockage ratio is made in Figs. 3.14 and 3.15, respectively for original jet aspect ratios of 5:1 and 10:1. Both figures concur in showing that larger blockage ratios give rise to higher values of the average Nusselt number. The figures also confirm that higher Reynolds numbers correspond to higher Nusselt numbers. A figure-to-figure comparison suggests that the 5:1 aspect ratio results are higher in magnitude than those for the 10:1 aspect ratio. This observation was previously made in connection with Figs. 3.12 and 3.13, where it was cautioned that the ordering of the results could be attributed to the area that was used in the definition of $\bar{h}$.

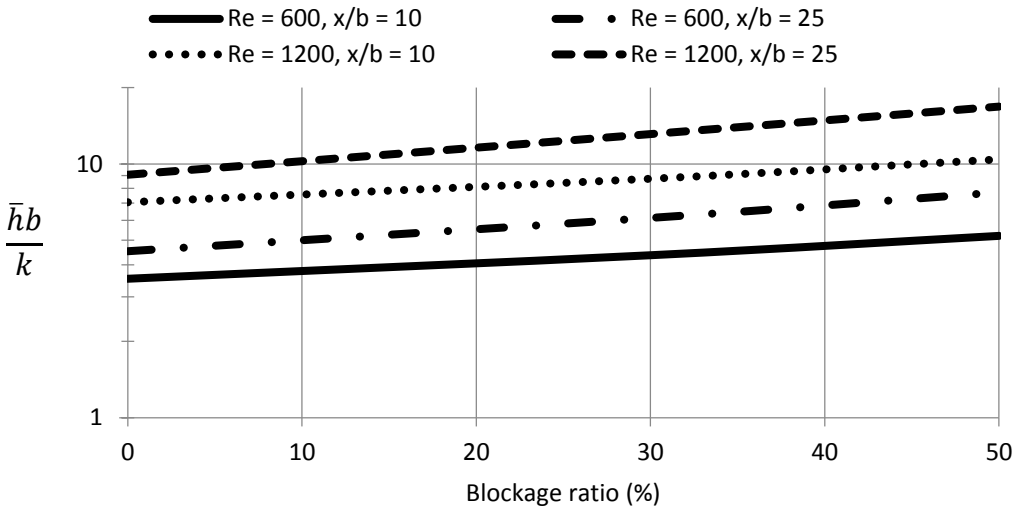

Fig. 3.14. Average Nusselt number results as a function of blockage ratio for the case of the initial jet aspect ratio of 5:1.

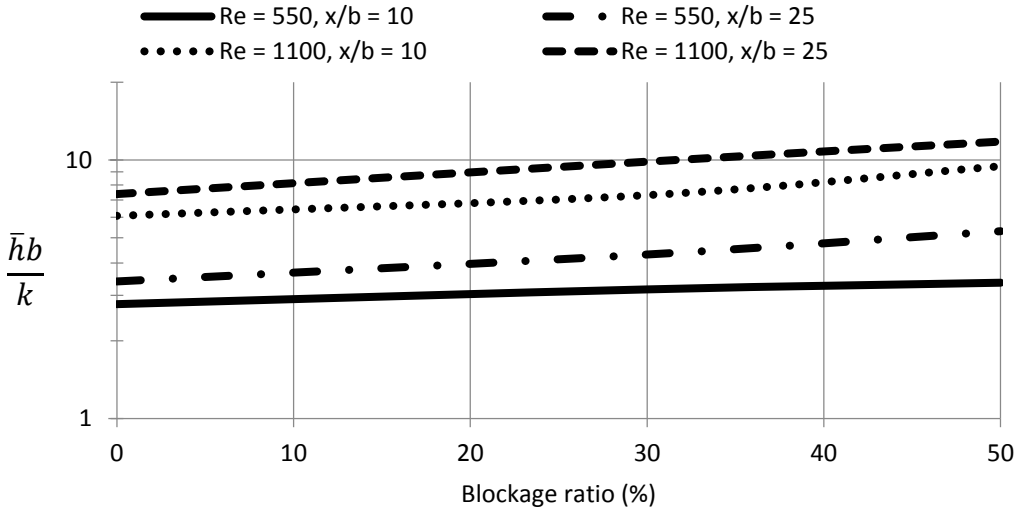

Fig. 3.15. Average Nusselt number results as a function of blockage ratio for the case of the initial jet aspect ratio of 10:1.

3.5.1 Local heat transfer coefficients

Representative results for the local jet-impingement Nusselt number are presented in Fig. 3.16. The figure consists of four vertically-stacked horizontal strips. Each strip corresponds to a fixed Reynolds number and to a fixed distance of the impingement plate

from the jet origin. The three panels in each strip show results for blockage ratios of 0, 30, and 50%, arranged from left to right. The figure as a whole corresponds to an initial slot jet aspect ratio of 10:1. A color legend positioned to the left of each strip is keyed to the colors in the individual panels. The numerical values indicated in the color strips correspond to local Nusselt numbers hb/k, where h is defined as the ratio of the local heat flux divided by the fluid-to-plate temperature difference.

It can be seen from the figure that for a fixed Reynolds number and a fixed downstream location of the impingement plate, the size of the impingement zone increases with increasing blockage ratio. The size of the impingement zone also increases with increasing downstream distance of the impingement plate for fixed values of the Reynolds number and the blockage ratio. With respect to the role of the Reynolds number, there is only a moderate effect on the size of the impingement zone but higher velocities have a direct effect on the magnitudes of the local heat transfer coefficients.

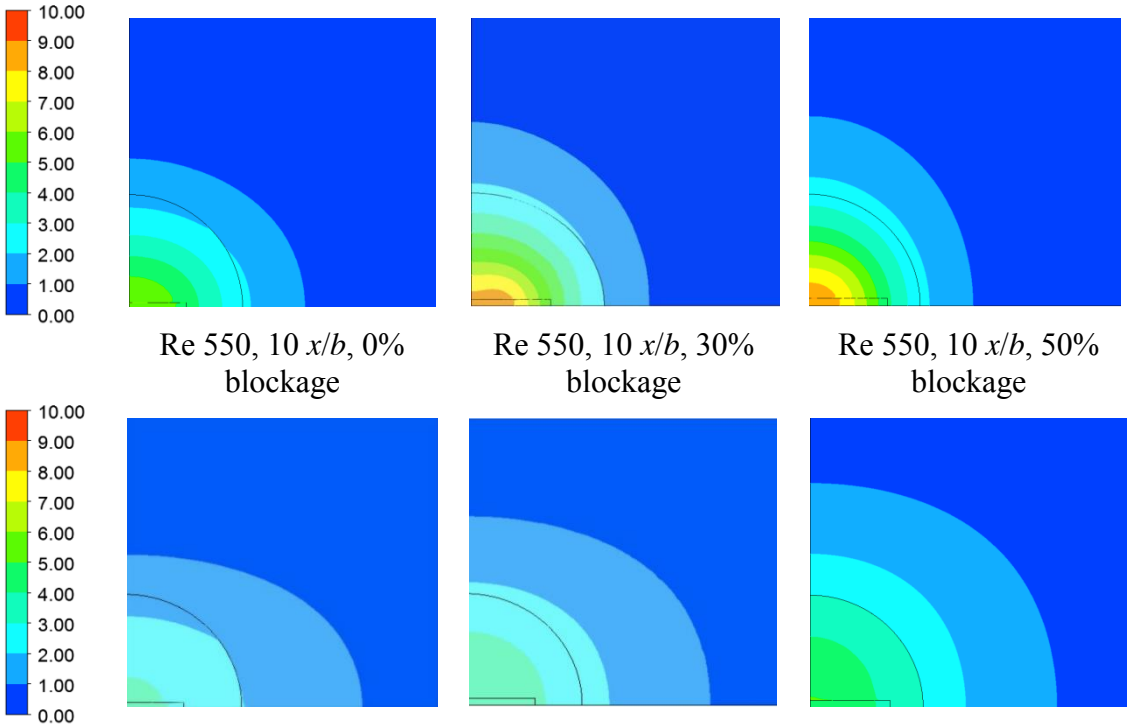

Re 550, 10 *x*/*b*, 0% blockage | Re 550, 10 *x*/*b*, 30% blockage | Re 550, 10 *x*/*b*, 50% blockage

Re 550, 25 *x*/*b*, 0% blockage | Re 550, 25 *x*/*b*, 30% blockage | Re 550, 25 *x*/*b*, 50% blockage

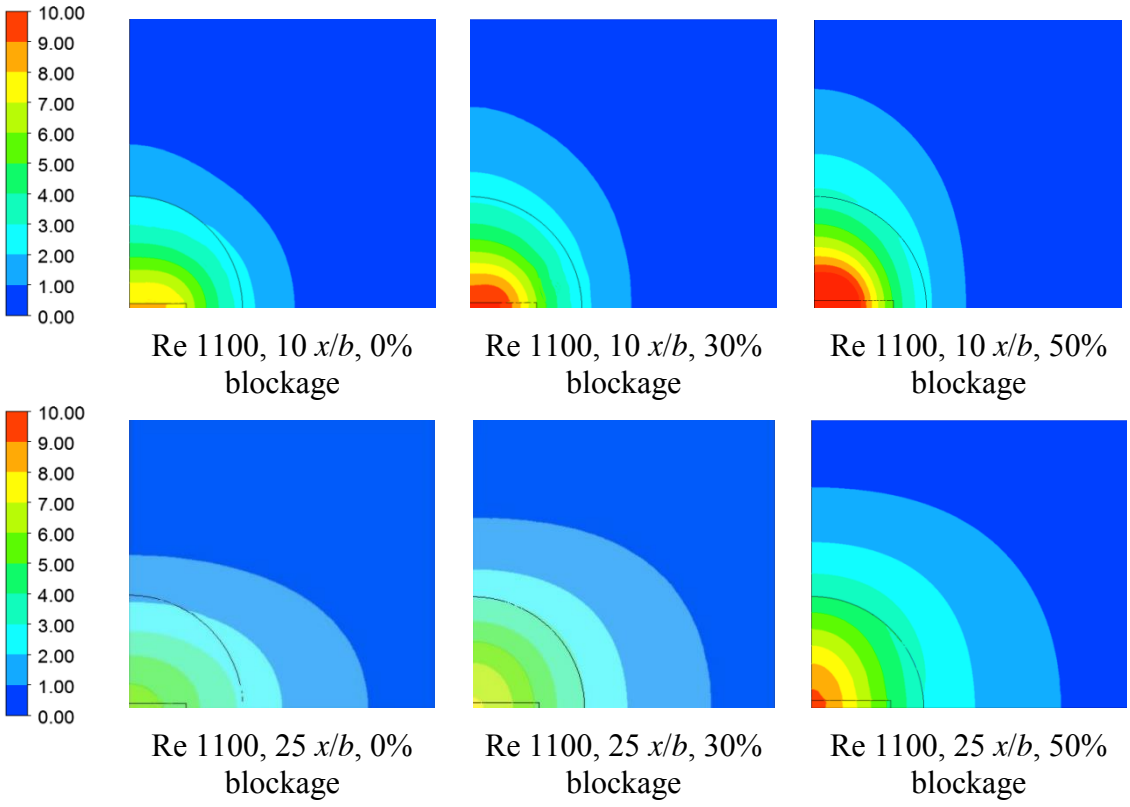

Fig. 3.16. Contour diagrams showing the magnitude and the spatial distribution of the local Nusselt number *hb*/*k* on the impingement plates.

3.6 RETROSPECTIVE FOR CHAPTER 3

Axis switching of jets issuing from large-aspect-ratio rectangular slots were investigated by numerical simulation with the goal of identifying the engineering impacts of that phenomenon. The limited previous work on the subject had focused on the vertical mechanisms that are inherent in the switching process. However, to the best knowledge of the writer, the engineering implications have not been explored. A unique focus of the work is the characterization of the effect of jet-axis switching on heat transfer. This topic has never been investigated in the past, perhaps because slot jet impingement has been universally modeled as a two-dimensional process. The special motivation for considering

heat transfer is the potential that the jet-axis switching process might serve as a heretofore undiscovered means of heat transfer enhancement.

The physical system consisted of rectangular ducts having aspect ratios that are the same as those of the rectangular slots at the duct exit. However, aside from a baseline case, the slot cross sections are smaller than those of the duct proper. The effect of the partial blockage of the flow due to the contraction imposed by the slot was explored in detail because its impact on the degree of axis switching and on the concomitant heat transfer enhancement. The flow within the duct proper was laminar but the emerging jet evolved from its laminar origins as witnessed by ratios of the turbulent viscosity to the laminar viscosity far exceeding one.

Chapter 4

PARTICLE TRANSPORT AND HEAT TRANSFER IN THE PRESENCE OF JET-AXIS SWITCHING

4.1 INTRODUCTION

In the preceding chapter, the phenomenon of jet-axis switching was set forth and applied to the fluid mechanics of slot jets and to the concomitant heat transfer. The impressive power of that phenomenon in transforming otherwise simple entrainment-based jet spreading into a metamorphosis of the jet cross section was quantified graphically for the first time. That extraordinary transformation of the fluid mechanics gave rise to an equally profound change in the convective heat transfer characteristics of the jet.

Here, attention is turned to the effect of jet-axis switching on solid-particle-laden fluid flow and heat transfer in the continuum regime. The initial motivation for this focus is the use of slot jets to distribute uniform particles to form coatings on surfaces on which the jet impinges [43-46]. To the best knowledge of the writer, researchers in that intensely active field appear not to be aware of jet-axis switching and its importance in their field.

In another field of study, particle impactors, it also appears the published literature is devoid of the effects of jet-axis switching on solid-particle-laden fluid flow in terms of particle collection. Many, if not all, of the numerical analyses for rectangular-jet-based particle impactors have been performed using two-dimensional models which necessarily precludes the effects of jet-axis switching [47-50].

Still another field that is relevant to the current research foci is the effect of jet-axis switching on jet impingement heat transfer in the case of non-circular jets. There is an extensive literature on this subject, but the literature survey set forth here will be limited to publications that relate to the phenomena of current interest and to rectangular slot jet impingement. A theme that has run though the rectangular slot-jet literature since 1968 is the presence of off-axis peaks in the value of the heat transfer coefficient. Off-axis peaks

are local maxima that are encountered at locations away from the center of the initial slot jet shape. Various attributions for the existence of these peaks have been a preoccupation of the literature. The discovery of such peaks is documented in [51]. Others who have either rediscovered these peaks or offered conjectures about them include [52-58]. An additional unexplained phenomenon is the discovery of multiple flow patterns [59].

The investigation to be described here will deal with a number of critical facets of particle transport including fluid-particle interactions, particle-particle interactions, particle collection, effects of gravity, and convective heat transfer impacts due to fluid flow responses to the presence of particles. It will be shown that these phenomena are majorly affected by jet-axis switching. It appears that the literature is mute on these subjects, so that the work to be presented is not able to be linked with any foregoing research.

A comparison with more traditional experimental results from the literature will be made in Section 4.7. Those experimental results for particle collection have several deviations from the current work. For example, the jet-exit to impingement plate distance is shorter than the presently investigated impingement plate locations.

The specific parametric variations that were undertaken during the course of the investigation are as follows:

(a) Distance between the jet orifice and the impingement plate
(b) Particle size (Stokes number)
(c) Per-particle density
(d) Particle mass flowrate
(e) One-way fluid-particle interactions
(f) Two-way fluid-particle interactions with or without particle-particle collisions
(g) Inter-particle friction models
(h) Reynolds number variations
(i) Gravity effects (Richardson number)
(j) Heat transfer response to fluid-mechanic response to particle presence

4.2 PHYSICAL MODEL

The geometry of the physical model is nominally the same as that conveyed in Figs. 3.1 and 3.2 of Chapter 3. Those figures are repeated here for the convenience of the reader. The particle focus of this chapter is implemented by having a specified stream of particles entering the system at the duct inlet. Those specifications include particle size, per-particle density, and particle mass flowrate. The problem is formulated in dimensionless form, so that the particle size is made dimensionless by the slot height *b* that is pictured in Fig. 4.2. The aspect ratio of the slot a/b is held consistent at a value of 10 to ensure that the desired initial flatness of the slot jet is well established.

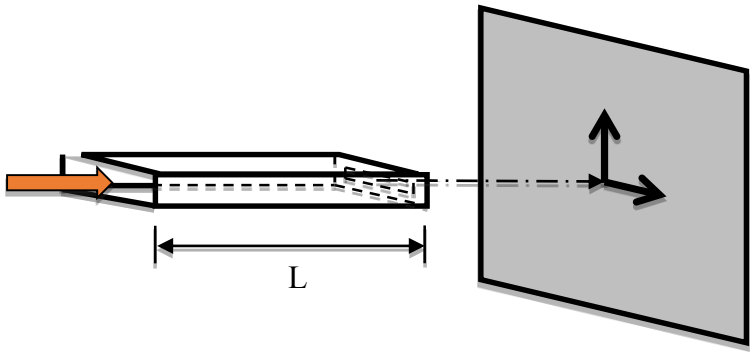

Fig. 4.1. Pictorial view of the physical situation.

The location of the impaction plate is expressed by the value of x/b, where the origin of x is centered in the plane of the jet exit as shown in Fig. 4.2. For the numerical simulations, the impingement plane was situated at $x/b = 10$. This single location is selected in deference to the need to vary several other parameters, all of which are related to fundamental physical phenomena.

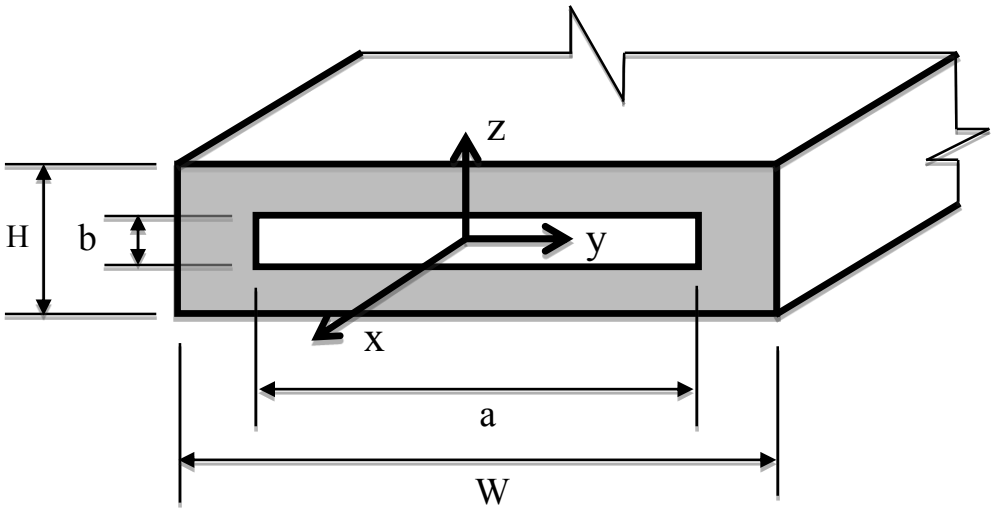

Fig. 4.2. Details of the exit plane of the duct.

4.3 PHENOMENOLOGICAL MODELS

The complex phenomena to be investigated requires that appropriate models be used for their description. For some of the investigated situations, the model is included in the governing differential equations alone; in other cases, the novel features of the model may be embedded in the boundary conditions; and in still other cases, part of the model is included in the governing differential equations and the other part in the boundary conditions.

The baseline case is that which does not involve the presence of particles. Since the fluid flow is turbulent, it is necessary to select a suitable turbulence model. The RANS (Reynolds-Average-Navier-Stokes) equations formed the starting point of the turbulence model. These equations make use of a turbulent viscosity μ_{turb} which, when added to the molecular viscosity μ, forms the effective viscosity μ_{eff}. There are a number of turbulence models in the literature which provide means for determining μ_{turb}. The writer has had extensive experience with many of these models and has found that the Shear Stress Transport model yields favorable results with respect to those of experiment. That model is a blending of two other turbulence models, respectively the k-ω and k-ε models. The

former has been shown to provide results of high accuracy in the near-wall region whereas the latter gives good results far from the wall.

The foregoing fluid flow model must be augmented by a statement of the conservation of mass. When heat transfer is involved, the First Law of Thermodynamics must be coupled to the velocity field equations.

When fluid-particle interactions are to be considered, different physical models are appropriate depending on whether the interactions are one-way or two-way. A one-way interaction occurs when the fluid flow controls the particle motion without in any way affecting the fluid. In contrast, in a two-way interaction, both the fluid and the particles are mutually affected. In the one-way case, the RANS equations remain as they were for pure fluid flow. In the case of two-way interactions, source terms must be appended to the RANS equation to account for the fluid-solid force interactions.

For both types of interactions. The particle motions are governed by Newton's Second Law for a fixed mass. As will be detailed shortly, the forces taken into account are friction and buoyancy. Virtual mass had been considered and found negligible.

4.4 GOVERNING EQUATIONS

For the baseline cases of turbulent flow and heat transfer without particles, the governing equations are the same as those already set forth in the Governing Equations Section of Chapter 3. Those equations encompass Eqs. (3.1) through (3.8) and the nomenclature set forth there. For the particle flow cases with one-way fluid-particle interactions, the same governing equations are applicable for the fluid flow and heat transfer.

When there are two-way, fluid-particle interactions, there are both momentum and energy interchanges between the media. The quantification of these interactions requires the

appending of additional terms to both the RANS and First Law equations. The thus-generalized RANS equations become

$$\rho\left(u_i\frac{\partial u_j}{\partial x_i}\right) = -\frac{\partial p}{\partial x_j} + \frac{\partial}{\partial x_i}\left((\mu + \mu_{turb})\frac{\partial u_j}{\partial x_i}\right) + S_{P,j} \quad i = 1,2,3 \;\; j = 1,2,3 \tag{4.1}$$

where $S_{p,\,j}$ is a D'Alembert-force source term that represents particle contributions to the fluid's momentum in the case of two-way coupling. A corresponding source term is added to the First Law to quantify the energy interactions between the fluid and the solid particles. The energy equation with the added source term is

$$\rho c_p \frac{\partial(u_i T)}{\partial x_i} = \frac{\partial}{\partial x_i}\left[(k + k_{turb})\frac{\partial T}{\partial x_i}\right] + S_E \tag{4.2}$$

in which S_E is an energy source term coupling fluid and particles.

4.4.1 Governing Equations for Particle Tracking

The foregoing governing equations for fluid flow and heat transfer are based on the application of the conservation laws to a control volume fixed in space. That approach is designated as Eulerian. In contrast, the tracking of specific particles is termed Lagrangian. The tracking is carried out by forming a set of ordinary differential equations for each particle. The set includes equations for position, velocity, mass, and temperature. These equations are then integrated to determine the behavior of the particles as they pass through the solution domain.

Each particle is tracked from its starting location (inlet) until it either is collected on the impingement plate or leaves the solution domain. The source terms which have been appended to Eqs. (4.1) and (4.2) to quantify the interactions between the fluid and the particles are obtained from an average taken over all the particles being tracked.

The particle position is given by

$$x_p^{new} = x_p^{old} + U_p^{old}\delta t \tag{4.3}$$

where x_p^{old} is the instantaneous particle location at time *t*, and U_p^{old} is the particle velocity at that time. The step size for the evolving time is δt, and x_p^{new} is the new particle position at the end of that time step.

Since the tracked particle has a fixed mass, Newton's Second Law is applicable to describe its motion.

$$m_p \frac{d\boldsymbol{U_p}}{dt} = \boldsymbol{F_D} + \boldsymbol{F_B} \tag{4.4}$$

where m_p is the mass of the particle, and $\boldsymbol{F_D}$ and $\boldsymbol{F_B}$ are, respectively, the drag force and the buoyancy force that act on the particle.

The drag force $\boldsymbol{F_D}$ experienced by the particle is given by

$$\boldsymbol{F_D} = \frac{1}{2} C_d \rho A_{eff} \left|\boldsymbol{U_f} - \boldsymbol{U_p}\right| \left(\boldsymbol{U_f} - \boldsymbol{U_p}\right) \tag{4.5}$$

where C_d is the drag coefficient. In Eq. (4.5), A_{eff} is the particle cross section, $\boldsymbol{U_f}$ is the local mean fluid velocity, and ρ is the density of the fluid. To calculate C_d, the following modified form of the Schiller-Naumann [60] drag model was used

$$C_d = max\left[\frac{24}{Re_p}\left(1 + 0.15 Re_p^{0.687}\right), 0.44\right] \tag{4.6}$$

in which Re_p is the Reynolds number based on particle diameter d_p and is defined as

$$Re_p = \frac{\rho|U_p - U_f|d_p}{\mu} \tag{4.7}$$

The buoyant force on a particle $\boldsymbol{F_B}$ is quantified by

$$\boldsymbol{F_B} = (m_p - m_f)\boldsymbol{g} = \frac{\pi}{6} d_p^3 (\rho_p - \rho)\boldsymbol{g} \tag{4.8}$$

where m_p is the particle mass, m_f is the mass of the fluid displaced by the particle, $\boldsymbol{g}$ is the gravity vector, ρ is the fluid density, and ρ_p is the density of the particle. Since the buoyancy forces that act on the particle do not directly affect the particle momentum exchange with the fluid, the fluid momentum source term $S_{p,j}$ in Eq. (4.1) is found from

$$\frac{dS_{p,j}}{dt} = -F_{D,j} \tag{4.9}$$

In situations where heat transfer occurs between the particles and the fluid, the energy balance for the particle is

$$(mc_p)_p \frac{dT_p}{dt} = Q_{convection} = hA(T_f - T_p) \tag{4.10}$$

where h is the surface-average convective heat transfer coefficient between the fluid and the particle. The quantity A is the surface area of the particle, T_p is its temperature, and T_f is the fluid temperature. Equation (4.10) contains the implicit assumption that the particle temperature is spatially uniform. This assumption is supported by the very small value of the Biot number.

In order to obtain suitable values of the heat transfer coefficient h, the well-established Nusselt number equation for heat transfer between a sphere and a flowing fluid is used [61]. Note that in the limit of zero Reynolds number, heat conduction prevails as witnessed

by the relation $hD_p/k = 2$, where k is the thermal conductivity of the fluid. The complete Nusselt number equation is

$$Nu_p = \frac{hd_p}{k} = 2 + 0.6Re_p^{\frac{1}{2}}Pr^{\frac{1}{3}} \tag{4.11}$$

in which Pr denotes the Prandtl number, which is a fluid property. The corresponding energy source term S_E which appears in Eq. (4.2) is then determined by

$$\frac{dS_E}{dt} = -Q_{convection} \tag{4.12}$$

4.4.2 Particle-Particle Collision Model

For the cases in which particle-particle collisions were taken into account, Sommerfeld's stochastic collision model was used [62, 63]. This model saves computational resources by making use of virtual collision partners and collision probability. In order to calculate the momentum transfer after a virtual particle-particle collision, it is necessary to specify the coefficients of restitution and the static and kinetic friction coefficients for the particles. With regard to the physical interpretation of the coefficient of restitution, a value of one would equate to a completely elastic collision and a value of zero would be entirely inelastic.

4.5 RESULTS FOR FLUID FLOW AND PARTICLE TRANSPORT

The breadth and depth of the results to be presented here is displayed in Table 4.1 along with the values of the fluid-based Reynolds number for which the results were obtained. The Reynolds number is defined as $Re = Ub/v$, where U is the mean velocity of the air in the duct upstream of the jet orifice plate, b is the smaller dimension of aperture in the orifice plate, and v is the kinematic viscosity of the air. For all of the situations considered here, certain parameters where held constant: (a) the aspect ratio (ratio of the larger dimension to the smaller dimension of the aperture in the orifice plate) is 10, (b) the contraction

experienced by the flow passing from the upstream duct through the aperture (i.e., the blockage ratio) was fixed at 50%, and (c) the smaller dimension of the aperture, $b = 5$ mm.

Table 4.1 Listing of investigated interactions and phenomena

Interactions and phenomena	**Reynolds number**			
	1,100	**8,000**	**11,000**	**15,000**
2D vs. 3D	x			
Effect of gravity	x	x	x	x
Effect of impingement plate location			x	
Effect of particle density			x	
Effect of particle size	x	x	x	x
Effect of particle quantity			x	
One-way vs. two-way momentum transfer			x	
Effect of particle-particle collisions			x	
Effect of particles on heat transfer			x	

The first of the results to be presented is, in actuality, an extension of those of Chapter 3. In that chapter, the participating Reynolds numbers were in the 500-1000 range whereas here larger Reynolds numbers are being considered. The motivation for the presentation conveyed in Fig. 4.3 is to demonstrate the response of the jet-axis switching phenomenon to higher fluid velocities. The new results correspond to a fluid Reynolds number of 11,000. There is an impingement plate at $x/b = 35$.

Inspection of Fig. 4.3, together with retrospective remembrance of the results of Chapter 3, immediately reveals a major effect of the fluid velocity on the nature of the jet-axis switching. The major impacts of the high velocity are the rapidity in which the switching asserts itself and the markedly enlarged reversal in shape experienced by the jet.

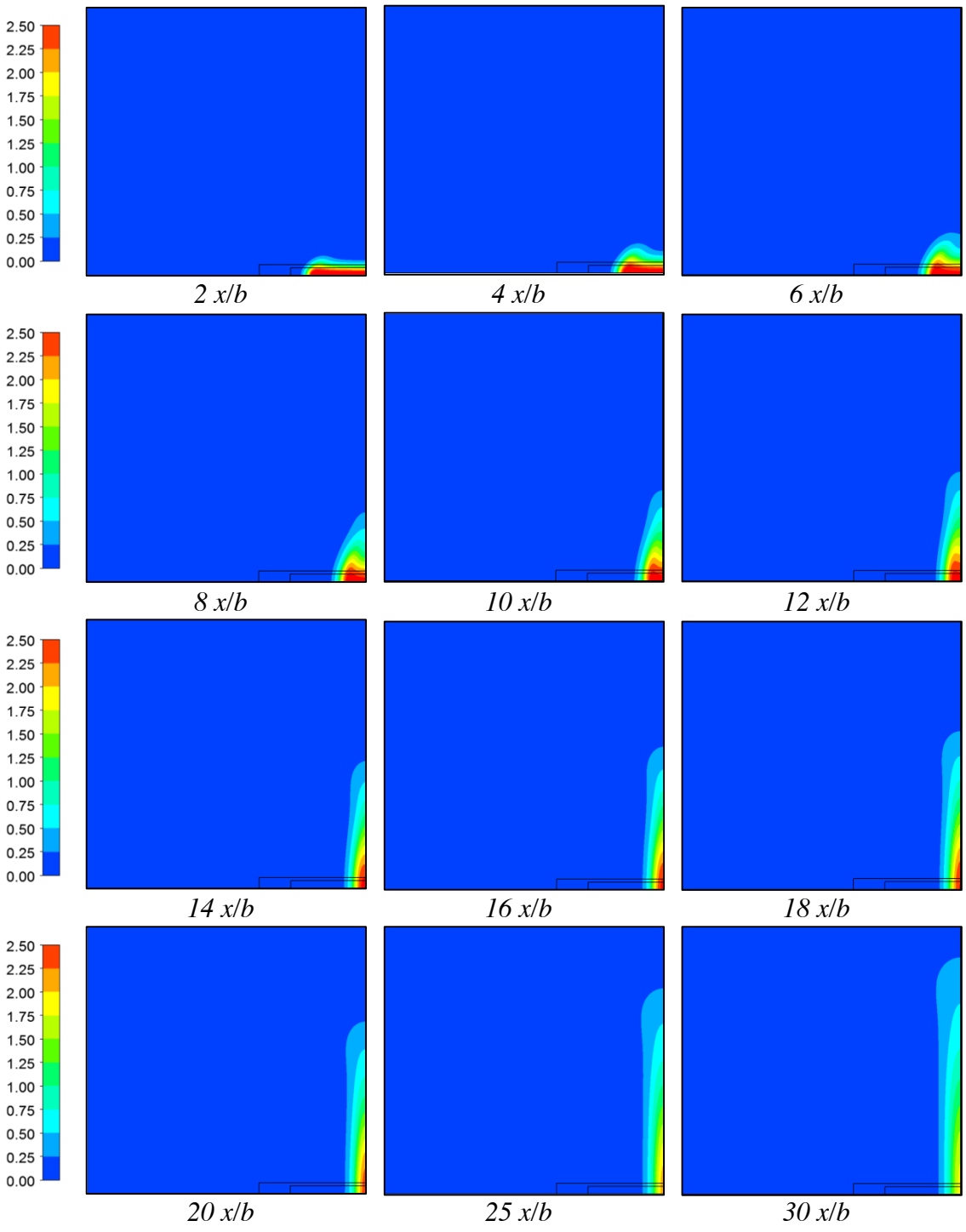

Fig. 4.3. Evolution of the initial slot-jet shape with increasing downstream distance from the jet-orifice for a Reynolds number of 11,000. An impingement plate is situated at x/b = 35.

The next figure, Fig. 4.4, is focused on comparing the results of the current three-dimensional model with those of a two-dimension model of the problem. To achieve a two-dimensional model, the jet aspect ratio has to be regarded as infinity. The particular motivation of addressing the two-dimensional case is the fact that the literature on particle transport is strongly two-dimensional. Another feature of Fig. 4.4 is the assessment of the effect of gravity. The dimensionless parameter which is used to quantify the gravity effect is the Richardson number Ri which is defined as gb/U^2. Note that the appearance of the velocity in the definition of the Richardson number can play an important role in its magnitude.

The ordinate and abscissa variables are worthy of elucidation. The *collection efficiency* which is plotted on the ordinate is a ratio defined as

$$Collection\ efficiency = \frac{number\ of\ particle\ collected}{total\ number\ of\ particles} \tag{4.13}$$

The abscissa variable is the square root of the Stokes number. For fixed particle density, fluid velocity and viscosity, and fixed orifice height, the magnitude of the Stokes number can be regarded as a measure of the particle diameter. Its basic definition is

$$St = \frac{\rho_p d_p^2 U C_c}{18\mu b} \tag{4.14}$$

The quantity C_c is the Cunningham correction factor given by

$$C_c = 1 + Kn\left(1.257 + 0.4e^{-1.1/Kn}\right) \tag{4.15}$$

in which *Kn* is the Knudsen number which is taken as a means of comparing the molecular mean free path to a typical dimension for the problem under consideration. Its definition is

$$Kn = \frac{k_B T}{\sqrt{2}\pi d_p^2 p b} \tag{4.16}$$

The quantities k_B, T, and p that appear in Eq. (4.16) are the Boltzmann constant, the temperature, and the total pressure respectively. For all of the investigated cases, T = 300 K and p = 1 atm.

The focus of this work is on particle transport in the continuum regime. It is important to note that the jet-exit to impingement-plate locations are larger than those found in traditional impactors. As a result, the range of presented Stokes numbers for each set of results will likely differ from traditional impactors.

With these definitions in hand, consideration will now be directed to Fig. 4.4. The figure contains three curves, two of which are for the three-dimensional model while the third is for the two-dimensional model. For the conditions that were applied (see figure caption) in obtaining the results shown in the figure, the abscissa can be regarded as a measure of particle diameter.

The first comparison to be made involves the two- and three- dimensional models for the no-gravity case (Ri = 0). It can be seen from the figure that the results for these cases do not bear any relationship with each other. This outcome indicates that two-dimensional models do not provide results of any actual relevance to reality. In particular, it is seen that there is a large range of particle diameters which are not collected according to the predictions of the two-dimensional model but which are collected according to the predictions of the three-dimensional model.

For the three-dimensional case, a comparison may be made between the with-gravity and the without-gravity situations. The figure shows that the accounting of gravity increases the range of particle diameters that are subject to collection.

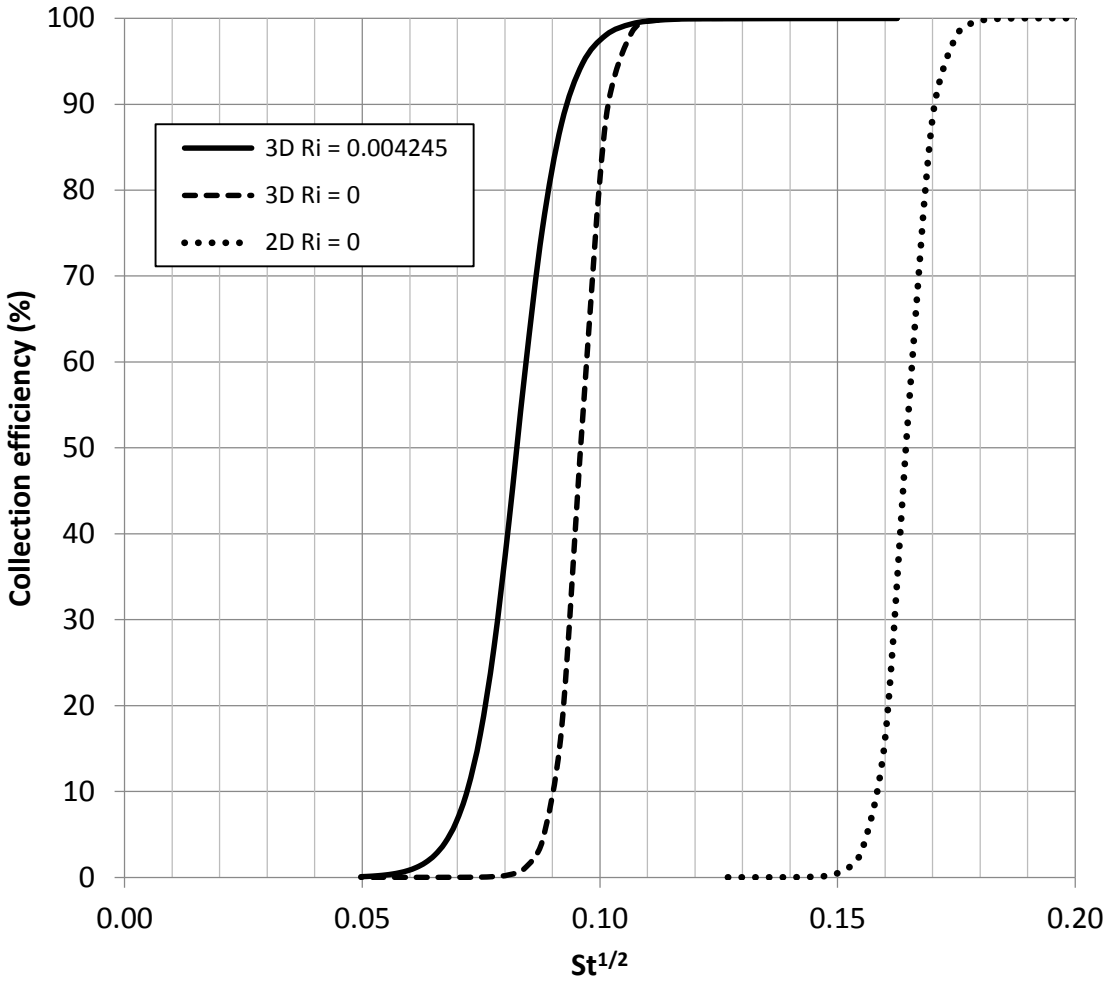

Fig. 4.4. Dependence of the collection efficiency on the particle size. Results are given for both two-dimensional and three-dimensional models of the particle-laden fluid flow. The fluid-particle interactions are one-way, and there are no particle-particle interactions considered. Results are also displayed for the effect of gravity on particle collection efficiency by means parametric values of the Richardson number Ri. The other parametric values that relate to the results are: Re = 1,100, ρ_p/ρ_f = 2000, impingement plate at x/b =10, and coefficients of restitution = 0.

The next focus is to illustrate the role of particle density, and Fig. 4.5 has been prepared for this purpose. To facilitate the display of the effect of particle density, two values of particle density are considered, ρ_p/ρ_f = 2000 and 8930. These values correspond to approximately aluminum and silver particles, respectively.

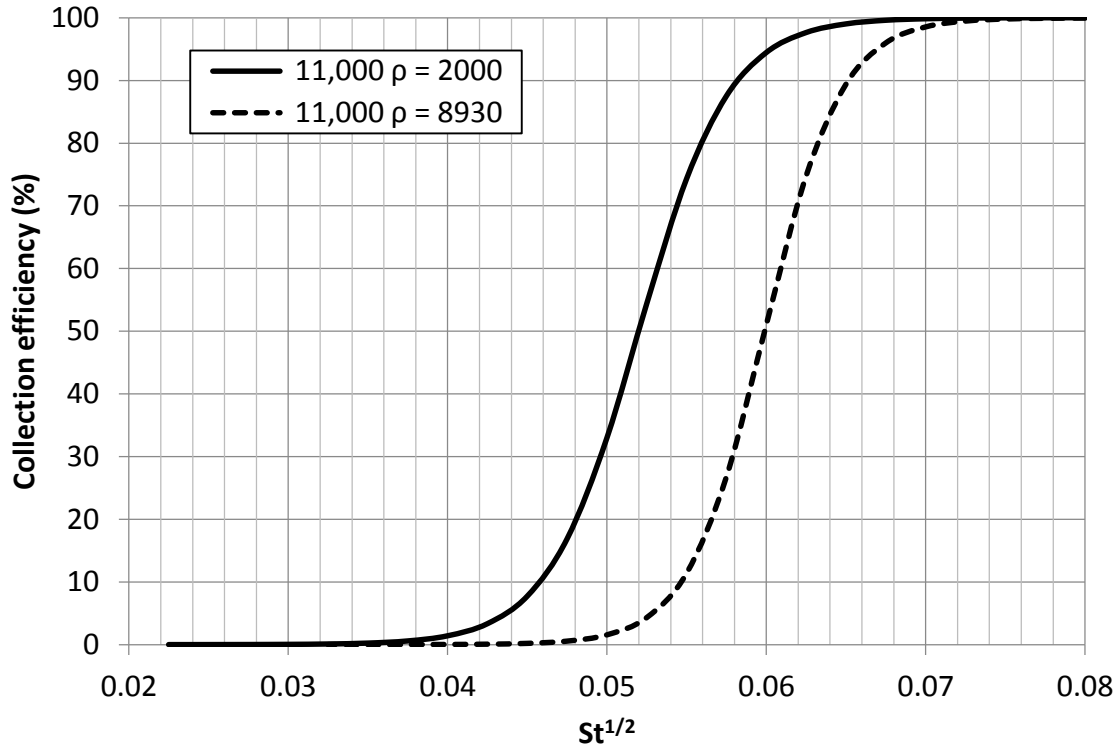

Fig. 4.5. Dependence of the collection efficiency on the magnitude of the Stokes number. Results are given for two values of the particle density, ρ_p/ρ_f = 2000 and 8930. The fluid-particle interactions are one-way, and there are no particle-particle interactions considered. The other parametric values that relate to the results are: Re = 11,000, Ri = 0.00004245, impingement plate at x/b =10, and coefficients of restitution = 0.

The extraction of useful information from this figure will now be described. It is assumed that the collection efficiency is to be determined for given values of the particle density ρ_p and diameter d_p; the air density ρ_f, viscosity μ_f, total pressure p, and absolute temperature T; the Reynolds number Re (dimensionless fluid velocity); and the smaller dimension b of the jet-formation slot. These quantities can be used to evaluate the square root of the Stokes number $St^{1/2}$, thereby defining the abscissa parameter of Fig. 4.5. This information allows the determination of the collection efficiency for either ρ_p/ρ_f = 2000 or 8930.

The next focus is the determination of the collection efficiency on the air flow-based Reynolds number over the range from 1,100 to 15,000. This information is conveyed in Fig. 4.6 where the efficiency is plotted as a function of $St^{1/2}$ for parametric values of the Reynolds number. A general observation that flows from the results is that for low

Reynolds number flows, the range of $St^{1/2}$ that result in particle collection is much reduced compared to the ranges that correspond to higher Reynolds numbers. The use of Fig. 4.6 to extract collection efficiencies is based on specifying the particle diameter d_p and using the other known parameters that are indicated in the figure caption to calculate the value of $St^{1/2}$. Although it is not shown in the figure, the high Reynolds number results are completely independent of the value of the Richardson number.

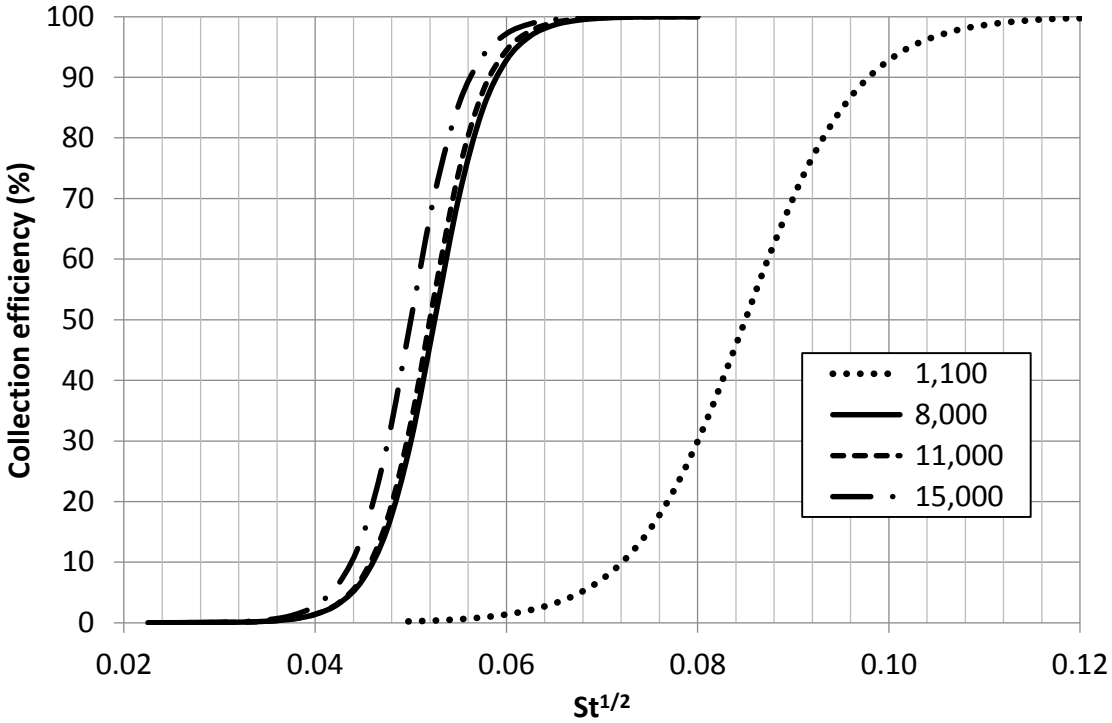

Fig. 4.6. Dependence of the collection efficiency on the magnitude of the Stokes number. Results are given for four values of the fluid based Reynolds number. The fluid-particle interactions are one-way, and there are no particle-particle interactions considered. The other parametric values that relate to the results are: $\rho_p/\rho_f = 2000$, impingement plate at $x/b = 10$, coefficients of restitution = 0, total pressure of the air and absolute temperature of the air. The Richardson number for the separate curves is determined from $5136/Re^2$.

The nature of the presentation will now be refocused to convey more qualitative information. Figure 4.7 conveys a sequence of panels which display impingement patterns. The panels are parameterized by dimensionless particle size ranging from $b/20$ to $b/400$, where b is the smaller dimension of the jet-forming slot. Inspection of the successive panels starting with that for $b/20$ and ending at $b/400$ indicates a very strong effect of jet-axis

switching on the pattern of particle collection. As the particle size diminishes, the effect of switching becomes more and more significant.

In interpreting the displayed information, it is important to recognize that the degree to which the particles follow the fluid's streamlines is greater with decreasing with particle size. For the larger particles, the trajectories do depart from those of the streamlines. It is believed that the particle trajectories for the *b*/20 and *b*/50 particles differ from the streamline's trajectories. However, it is expected that the smaller particles, *b*/300 and *b*/400, have trajectories that are similar to those of the streamlines. Evidence for these conjectures is afforded by the change of particle distribution from the horizontal to the vertical.

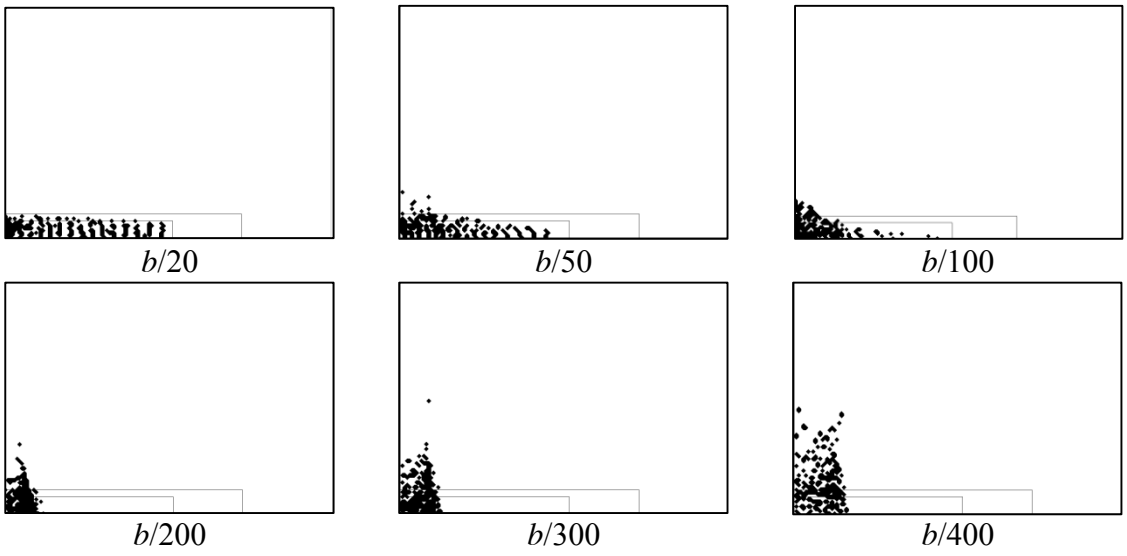

Fig. 4.7. Particle impingement patterns on a plate situated at $x/b = 10$ for a range of particle sizes between *b*/20 and *b*/400. The results correspond to a value of the fluid based Reynolds number of 11,000 and to a particle density $\rho_p/\rho_f = 8930$. The fluid-particle interactions are one-way, and there are no particle-particle interactions considered. The other parametric values that relate to the results are: coefficients of restitution = 0 and total pressure of the air and absolute temperature of the air. The Richardson number is from $5136/\mathrm{Re}^2$.

A more encompassing display of particle collection patterns is conveyed in Fig. 4.8. The primary independent parameter is the distance *x*/*b* of the impingement plate from the jet exit, ranging from $x/b = 5$ to 35. Other parametric variations that are included in the figure

are particle sizes $b/50$ and $b/100$, and particle densities ρ_p/ρ_f of 2000 and 8930. The Reynolds number is held fixed at 11,000. To conveniently extract particle size information from the figure, it is appropriate, at each plate location x/b, to compare the first and second columns. On the other hand, to extract particle density information, the second and third columns should be compared. Finally, to identify the effect of impingement plate location, it is most efficient to select a particular column and read downward from top to bottom.

Attention will first be focused on the results for the particle density defined by $\rho_p/\rho_f = 8930$. For plate locations up to approximately $x/b = 25$, the smaller particles are more responsive to jet-axis switching. At larger distances of the impingement plate from the jet orifice, an opposite trend is in evidence. The lower density particles ($\rho_p/\rho_f = 2000$) are clearly more responsive to jet-axis switching than are the higher density particles. This trend is valid at all of the x/b plate locations.

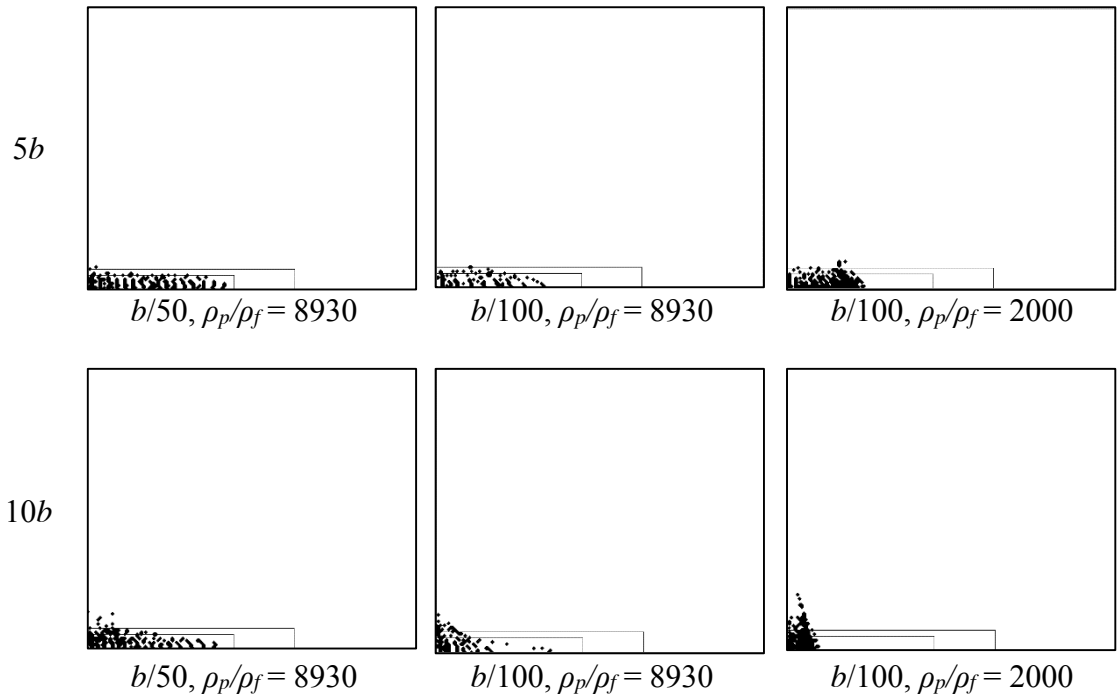

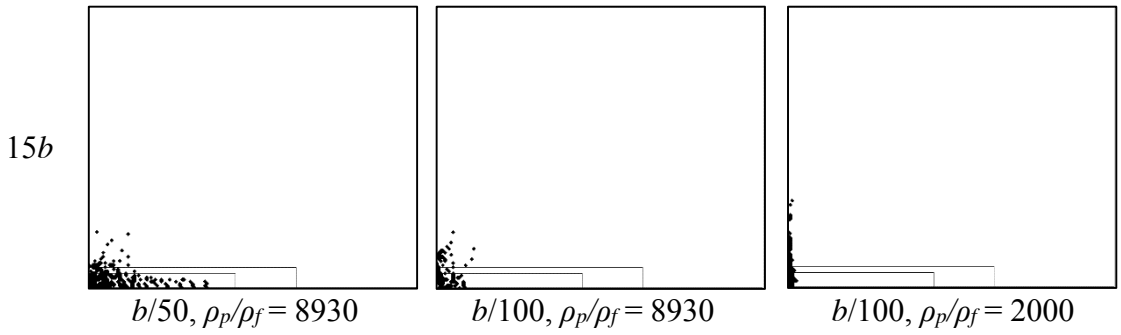

15*b*

b/50, $\rho_p/\rho_f = 8930$ *b*/100, $\rho_p/\rho_f = 8930$ *b*/100, $\rho_p/\rho_f = 2000$

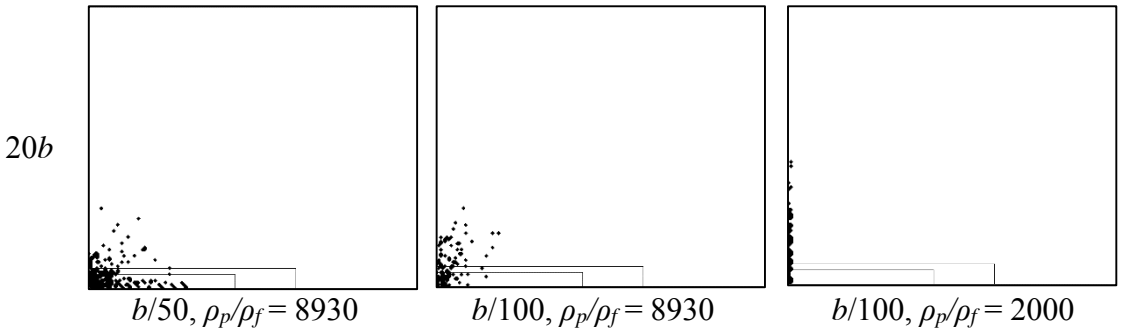

20*b*

b/50, $\rho_p/\rho_f = 8930$ *b*/100, $\rho_p/\rho_f = 8930$ *b*/100, $\rho_p/\rho_f = 2000$

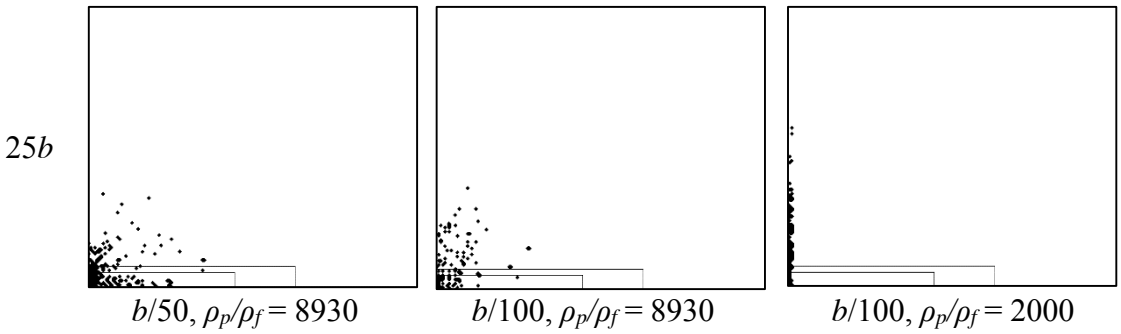

25*b*

b/50, $\rho_p/\rho_f = 8930$ *b*/100, $\rho_p/\rho_f = 8930$ *b*/100, $\rho_p/\rho_f = 2000$

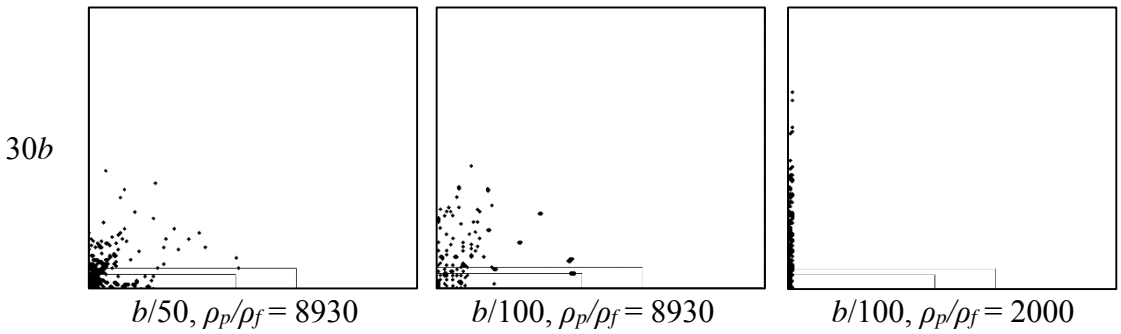

30*b*

b/50, $\rho_p/\rho_f = 8930$ *b*/100, $\rho_p/\rho_f = 8930$ *b*/100, $\rho_p/\rho_f = 2000$

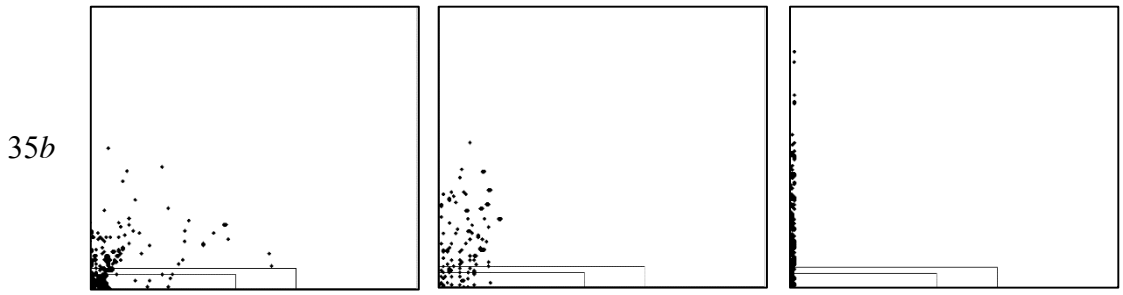

Fig. 4.8 Particle impingement patterns on plates situated at x/b = 5, 10,…, 35 for particle sizes between $b/50$ and $b/100$. The results correspond to a value of the fluid-based Reynolds number of 11,000. Two particle densities ρ_p/ρ_f = 2000 and 8930 were investigated. The fluid-particle interactions are one-way, and there are no particle-particle interactions considered. The other parametric values that relate to the results are: coefficients of restitution = 0 and total pressure of the air and absolute temperature of the air. The Richardson number is from $5136/\mathrm{Re}^2$.

One of the special accomplishments of the present research is the determination of the modifications of the fluid motion when two-way fluid-particle interactions and particle-particle interactions occur simultaneously. The first issue in this connection is particle collection efficiency, and this information is conveyed in Table 4.2. The table demonstrates that conditions under which the two-way and particle-particle interactions become significant. The major independent variable in the table is the number of participating particles. The respective collection efficiencies corresponding to one-way and to two-way interactions are the important results.

Table 4.2. Particle collection efficiencies for different interaction situations. The impingement plate is situated at x/b = 10, Re = 11,000, $\mathrm{St}^{1/2}$ = 0.052, ρ_p/ρ_f = 2000, coefficients of restitutions = 0, total pressure and absolute temperature are 1 atm and 300 K, and the Richardson number is from $5136/\mathrm{Re}^2$.

Number of Particles	One-way Interaction Collection Efficiency %	Two-way Interaction Collection Efficiency %
800	60.9	60.0
80,000	60.9	61.3
800,000	60.9	63.7
8,000,000	60.9	69.3

Not unexpectedly, the collection efficiency corresponding to one-way fluid-particle interactions is independent of the number of particles. On the other hand, the efficiency increases monotonically with increasing particle numbers when two-way and particle-particle interactions occur. The first significant deviation between the one-way and two-way results occurs for a particle number of 800,000. When the particle number is increased to 8,000,000, the two-way collection efficiency is 15% larger than the one-way collection efficiency.

Detailed information on how the pattern of fluid flow is differently affected by one-way interactions and two-way interactions with particle-particle collisions. This information is conveyed in Fig. 4.9, which is a collection of individual panels each of which corresponds to a different plane of observation parameterized by x/b. The impingement plate is situated at $x/b = 10$. The figure is arranged such that the left- and right- hand panels correspond to the same observation location but differ by the nature of the interactions. The colors displayed in the figure relate to a dimensionless velocity which is the ratio of the local velocity at any point relative to the average velocity in the upstream delivery duct.

Inspection of the figure shows that the type of interaction does not lead to significant differences at small values of x/b. Differences begin to emerge at $x/b = 3$ in that the upward protrusions for the two interaction conditions show a difference of size. The larger protrusion corresponds to the two-way situation. As the protrusions grow larger with increasing x/b, the protrusion size differences also enlarges. Both profiles tend to narrow as x/b increases. Clearly, what started as a strongly horizontal jet has morphed to a strongly vertical jet, with the two-way interaction case being more affected by the jet-axis switching.

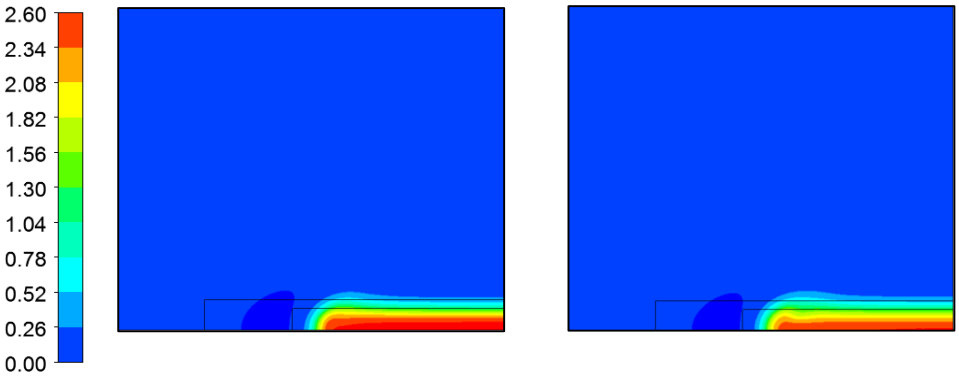

1 *x/b one-way* 1 *x/b two-way*

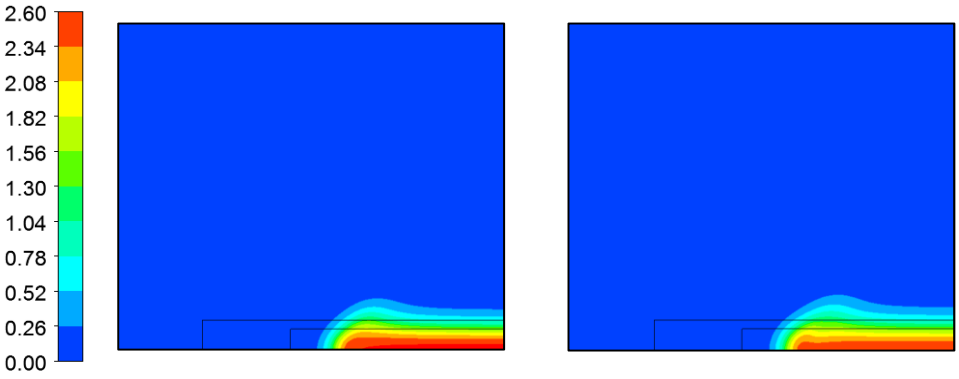

2 *x/b one-way* 2 *x/b two-way*

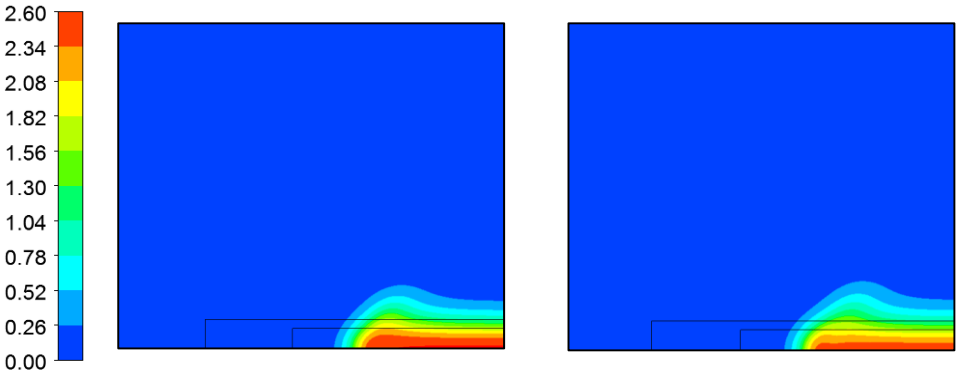

3 *x/b one-way* 3 *x/b two-way*

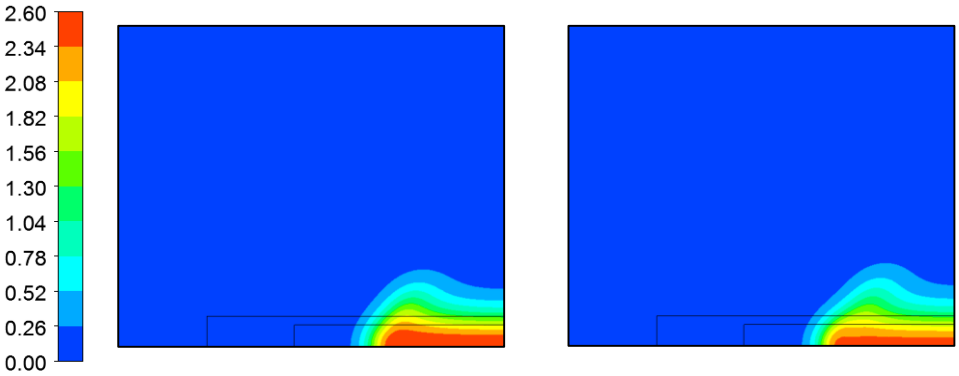

4 *x/b one-way* 4 *x/b two-way*

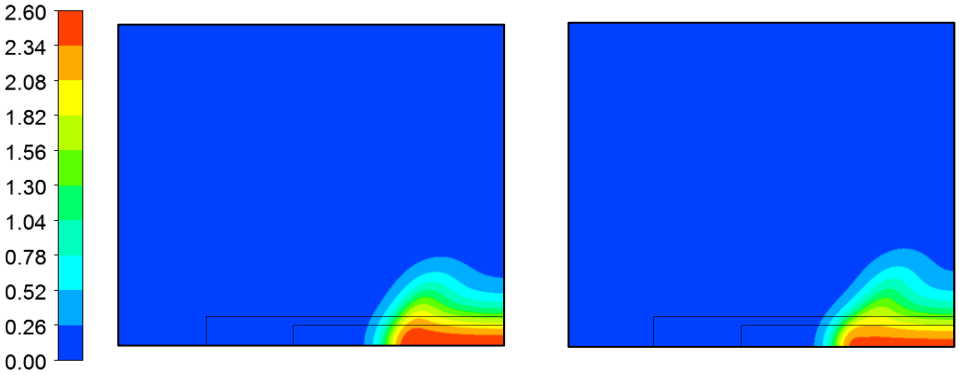

5 *x/b one-way* 5 *x/b two-way*

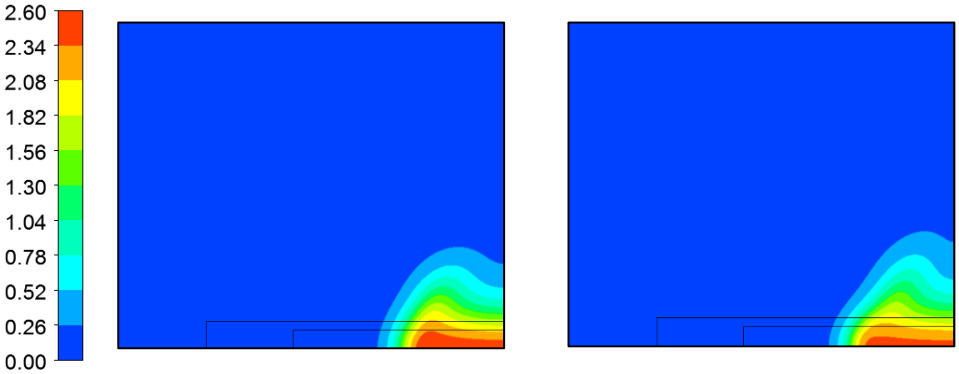

6 *x/b one-way* 6 *x/b two-way*

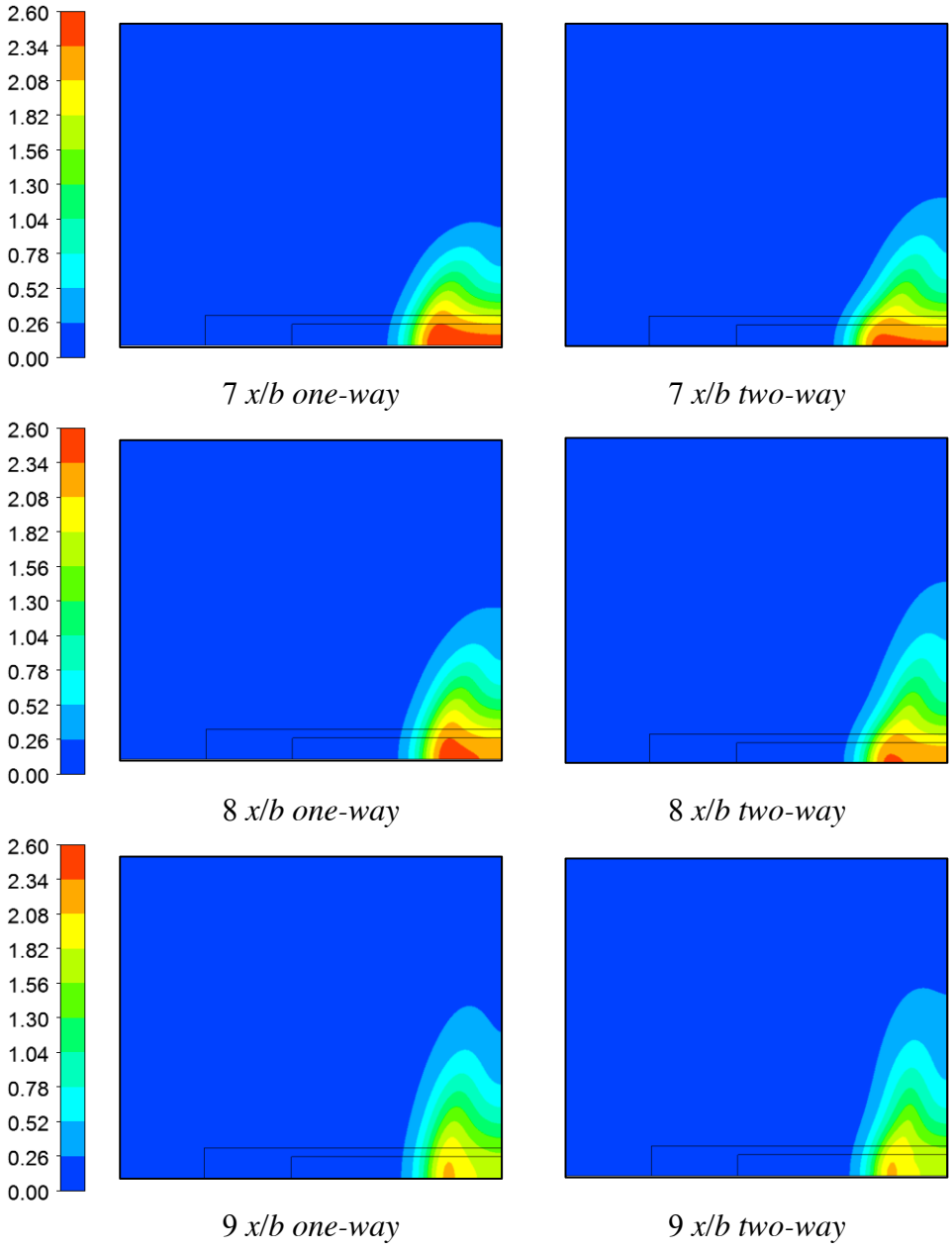

Fig. 4.9. Jet-axis switching in the presence of one-way fluid-particle interactions and in the presence of two-way fluid-particle interactions along with particle-particle interactions. The operating conditions for this figure are those of Table 4.2, except that the figure corresponds to a single number of particles = 8,000,000.

The possible effect of other independent variables on particle collection efficiency is set forth in Table 4.3. That table is based on variations of the coefficient of restitution for particle-particle interactions and on variations of the static and kinetic friction for the same

interactions. It can be seen from the table that neither of the newly introduced independent variables have a material effect on the collection efficiency.

Table 4.3 Effect of coefficient of restitution and of static and kinetic friction for particle-particle interactions on collection efficiency. The operating conditions are the same as for Table 4.2, except that the results correspond to a single number of particles = 8,000,000.

Particle-Particle Coefficient of Restitution	Particle-Particle Static and Kinetic Friction	Collection Efficiency %
1	0	70.6
1	0.2	70.4
1	0.5	70.4
0	0	70.0
0	0.2	69.9
0	0.5	69.9

4.6 RESULTS FOR HEAT TRANSFER IN THE PRESENCE OF A PARTICLE LADEN FLUID

The final focus of this chapter is to convey heat transfer results for various categories of interactions involving particles. These results are intended to complement those of Chapter 3 where axis-switching prevailed in the absence of particles. The definitions of the relevant heat transfer quantities are: (a) average heat transfer coefficient = $\bar{h} = Q/[ab(T_{plate} - T_{fluid})]$ and (b) average Nusselt number $\bar{h}b/k$. The quantity Q is the rate of heat transfer leaving the plate surface.

Three categories of interactions will be evaluated. One of the categories is: one-way fluid-particle interactions without particle heat transfer. In this situation, the presence of the particles does not affect the fluid motion. Furthermore, heat transfer between the fluid and the particles is suppressed, as is heat transfer between the particles and the plate. The bottom line is that the heat transfer situation is similar to that of Chapter 3. However, the Reynold number of the present results is much greater than those from Chapter 3.

The second category is: two-way fluid-particle interactions, including particle-particle interactions but without particle heat transfer. In the present context, the heat transfer between the fluid and the particles is suppressed, as is heat transfer between the particles and the plate. The issue being exposed is the effect of the presence of the particles on changes in the pattern of fluid flow and the possible effect of those changes on convective heat transfer between the fluid and the impingement plate.

The third of the categories is: two-way fluid-particle interactions including particle-particle interactions and with particle heat transfer. The heat transfer may occur between the fluid and the particles and between the particles and the impingement plate, as well as the conventional convective heat transfer between the fluid and the plate.

Table 4.4. Average Nusselt numbers for several modes of interaction as listed. The operating conditions are the same as for Table 4.2, except that the results correspond to a single number of particles = 8,000,000.

	One-way fluid-particle interactions, w/o particle heat transfer	Two-way fluid-particle interactions, w/o particle heat transfer	Two-way fluid-particle interactions, with particle heat transfer
$\frac{\bar{h}b}{k}$	6.32	6.40	126

The first two operating conditions respectively represent fluid flow undisturbed by the presence of particles and fluid flow possibly disturbed by the particles. Comparison of the corresponding Nusselt numbers suggest that any effect of the presence of the particles on the fluid flow is of no consequence. The last column includes possible heat transfer between the particles and the fluid and between the particles and the impingement plate. It also includes the impact of the presence of the particles on the fluid, but this effect has just been proven to be irrelevant.

It is clear that when direct heat transfer from the particles is allowed, there is an enormous impact on the Nusselt number by a factor of about 20. Since the initial temperatures of the particles and the fluid are the same, it may be expected that the particle-fluid heat transfer is of secondary importance and that the dominate reason for the great increase in the Nusselt number is due to particle-plate heat transfer.

As a companion to the average Nusselt number results of Table 4.4, local Nusselt numbers are presented in Fig. 4.10 for the same three operating conditions as were conveyed in the table. Not unexpectedly, the local Nusselt numbers, conveyed in the first two panels, are distributed more or less the same for the first two of the designated operating conditions. Furthermore, the color scale at the left of the first two panels is the same. In sharp contrast, the distribution of the Nusselt number for the third operating condition is drastically different from the others. Significant heat transfer occurs over a much larger portion of the impingement surface than in the preceding situations. Furthermore, the color strip indicates magnitudes that are much greater. It may be noted that the ratios of the local Nusselt number for the third operating condition to those of the first and second condition are smaller than the ratio of the average Nusselt number. This outcome may be attributed to the greater spreading of the heat transfer over the impingement plate.

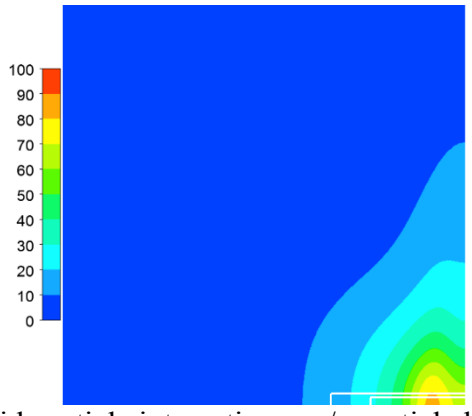

One-way fluid-particle interactions, w/o particle heat transfer

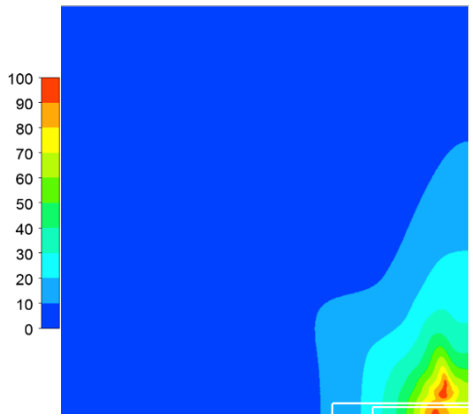

Two-way fluid-particle interactions, w/o particle heat transfer

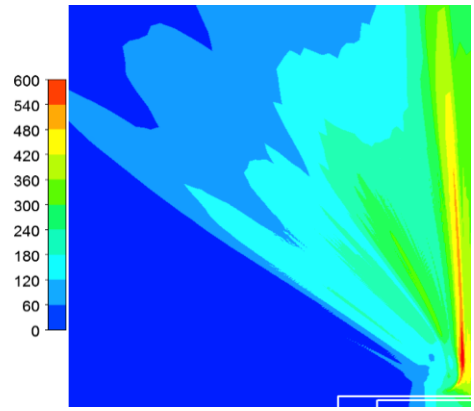

Two-way fluid-particle interactions, with particle heat transfer

Fig. 4.10. Local Nusselt number distribution on the impingement plate for three modes of interaction and for the operating conditions indicated in Table 4.4.

4.7 EXPERIMENTAL VERIFICATION OF HEAT TRANSFER AND PARTICLE COLLECTION WITH PUBLISHED LITERATURE

In order to verify the results of numerical simulations that are presented in the current chapter, it is appropriate to compare selected cases with experimental data available in the published literature. This was done by selecting two categories of results to be compared; stagnation-point heat transfer Nusselt numbers Nu_o and particle collection efficiency. First, attention will be directed to the stagnation-point Nusselt number results and comparison.

4.7.1 Stagnation Nusselt Number Results And Comparison

The stagnation Nusselt number Nu_o is defined as

$$Nu_o = \frac{h_o b}{k} \tag{4.17}$$

where h_o is the heat transfer coefficient at the jet stagnation point.

For the purpose of comparison, a paper by Gardon and Akfirat [51] was chosen since their experimental data provide results for a similar range of Reynolds as was used to parameterize the numerical simulations of Chapters 3 and 4. The focus of [51] was on air-jet impingement heat transfer on a heated plate using rectangular nozzles with aspect ratios of 24, 48, and 96. In that paper, the authors experimentally compared stagnation-point heat transfer results for air emerging from a slot nozzle by fixing both the aspect ratio and jet-nozzle-exit Reynolds number and then varying the distance *G* (see Fig. 3.3a) between the jet exit and the impingement plate.

The data from [51] shows that under certain conditions (aspect ratios between 24 and 96, nozzle-to-plate distances greater than or equal to $x/b = 10$, and Reynolds numbers equal to or less than 11,000), the stagnation-point Nusselt number did not vary with slot aspect ratio. A portion of the data curves from Fig. 2 of [51] have been reproduced here in Fig. 4.11 for the relevant range of Reynolds numbers (Re = 450, 550, 950, and 11,000). In addition, data points from cases that were numerically investigated in Chapters 3 and 4 for an aspect ratio of 10, without particle-laden flow, have been plotted in Fig. 4.11. The details of the selected data points have been identified in Table 4.5. The table relates each data point to its corresponding aspect ratio, Reynolds number, plate location, and Nu_o value.

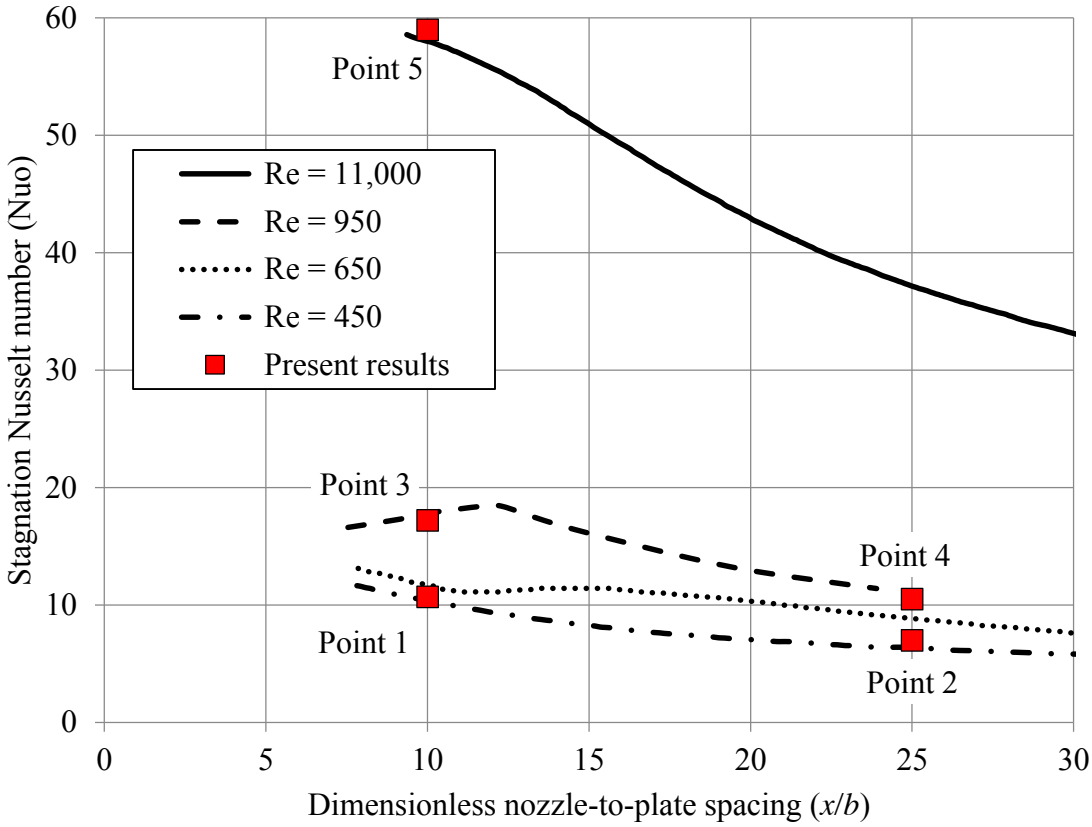

Fig. 4.11. Comparison of stagnation Nusselt number results versus nozzle-to-plate spacing for experiment-based data curves from [51] and selected points from the present investigation (see Table 4.5).

Table 4.5. Details of data points selected for comparison of stagnation-point Nusselt numbers in Fig. 4.11.

Point	**Aspect ratio**	**Re**	**Plate location *(x/b)***	**Nu_o**
1	10	550	10	11
2	10	550	25	7.0
3	10	1,100	10	17
4	10	1,100	25	10.5
5	10	11,000	10	59

From Fig. 4.11, it can be seen that the stagnation-point Nusselt numbers from the present numerical simulations are well within the range of values from the experiment-based data curves from [51]. Data points 1 and 2, corresponding to a Reynolds number of 550, are

situated in-between the corresponding experimental curves for Reynolds numbers of 450 and 650. Furthermore, data points 3 and 4, relating to Reynolds numbers of 1,100 are seen to be near the experimental-based curve for a Reynolds number in the range of 950. Since the authors of the experimental work did not report values closer to 1,100, it is uncertain how much variation in the values of Nu_o would exist for Reynolds numbers in that range. Finally, data point 5, corresponding to a Reynolds numbers of 11,000, is seen to be in virtual agreement with the experimental-based curve for 11,000. Overall, the presently-determined stagnation-point Nusselt numbers from the numerical simulations are well supported by the experimental data of [51].

4.7.2 Particle Collection Efficiency Comparison

Attention will now be directed to a comparison of the results from present approach of determining particle collection efficiency to the published experimental data related to rectangular-slot jet particle impactors. A publication reporting the experimental work of Mercer and Chow [49] was selected for comparison since their rectangular slot-jets were delivering solid spherical-particles using air as the carrier fluid in the continuum regime.

In order to effectuate the comparison, it was necessary to numerically simulate the physical experiment performed in [49]. The relevant parameters selected were: a slot width of b = 0.08 cm, a slot-jet aspect ratio of 15.875, an impingement plate at x/b = 1.0, a converging upstream nozzle section of length 34 b, and a nozzle-exit Reynolds number of 410. The impingement plate was 31.75 b by 47.63 b with the longer dimension of the plate aligned with the longer dimension of the slot-jet opening. The experimental results of the particle collection efficiencies from Fig. 7 of [49] have been reproduced here, along with the present numerical results, in Fig. 4.12. Each of the experimental datasets shown in the figure relates to different experimental methods used by the authors.

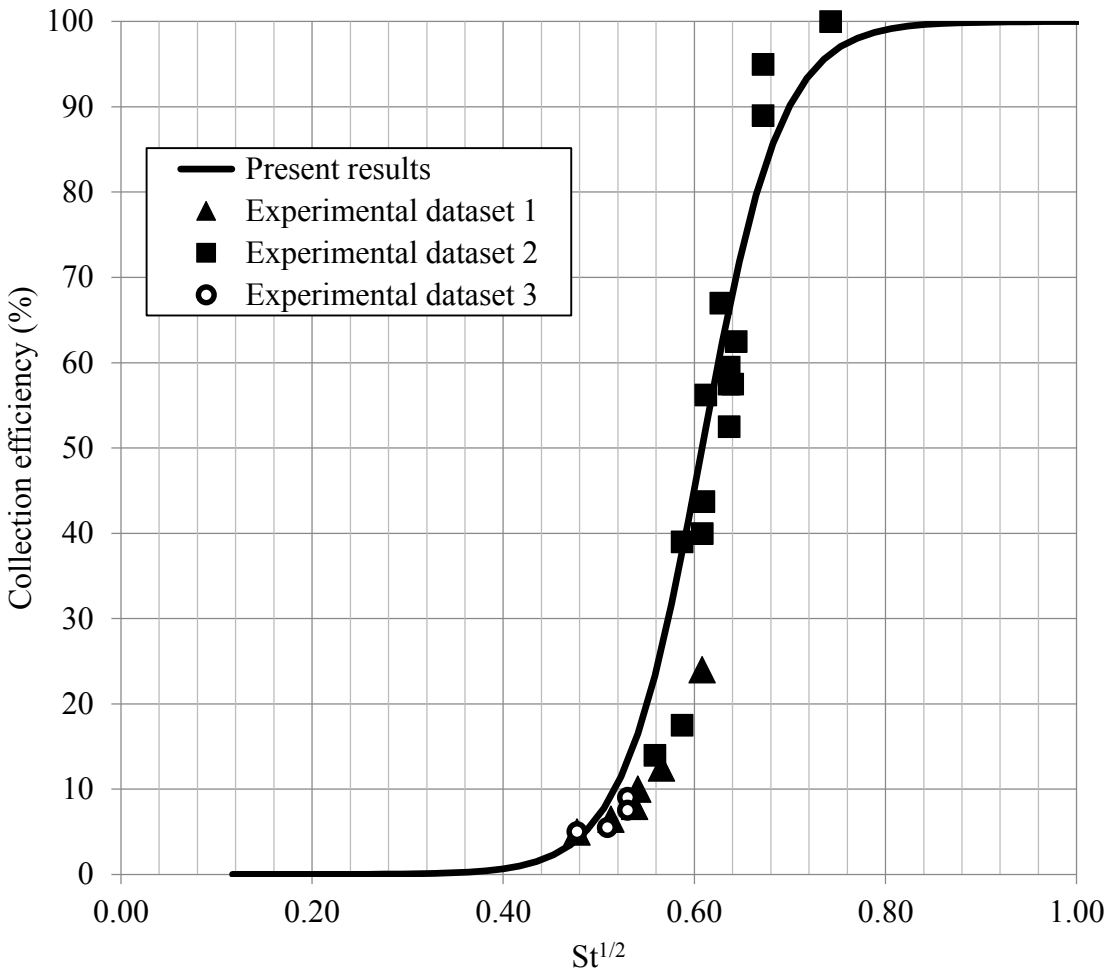

Fig. 4.12. Comparison of the present numerically-simulated particle collection efficiencies with experimental data obtained from Fig. 7 of [49]. The relevant parameters for the numerical model were: a slot width of b = 0.08 cm, a slot-jet aspect ratio of 15.875, an impingement plate situated at x/b =1.0, a converging nozzle section 34 b in length, and a nozzle-exit Reynolds number of 410.

Inspection of Fig. 4.12 reveals very good agreement between the present numerical results and the scatter of experimental data for particle collection efficiency. Possible variations in the experimental methods could be attributed to a number of causes; measurement errors could occur in finding the airflow velocity, particle size, impingement plate location, and number of collected particles on the plate. Other factors which may cause variation in the experimental results is the uniformity of the adhesive coating used to collect particles on the plate. It is also not known whether the adhesive coating spanned the entire plate in the

experiment. For the numerical simulation, it was assumed the entire plate had coefficients of restitution equal to zero, which means a particle impacting any portion of the plate would be collected and counted.

4.8 RETROSPECTIVE FOR CHAPTER 4

This chapter, in common with the preceding ones, deals with issues never before encountered in the published literature. Here, the focus is on the impact of jet-axis switching on particle-laden fluid flow and heat transfer. The physical model is pregnant with the many interactions that necessarily occur in the presence of multiple physical phenomena.

The considered interactions between the fluid and the particles include: one-way fluid—particle interactions, two-way fluid—particle interactions, and particle—particle interactions. In the first of these, the fluid flow may affect the trajectories of the particles, but the presence of the particles does not affect the fluid. In two-way interactions, the fluid and the particles mutually affect each other. The model employed for two-way interactions also includes particle—particle interactions.

Several heat transfer models were used with a view toward identifying the relative importance of various physical processes. One-way fluid—particle interactions have no effect on the heat transfer between the fluid and the impingement surface. For the case of two-way interactions, the relevant issue is whether the possible alteration of the pattern of fluid flow might affect the fluid-to-plate heat transfer; but this effect was found to be minimal. The major effect on the heat transferred to the impingement plate occurred when direct heat transfer between the impinging particles and the plate was allowed.

The effect of the jet-axis switching phenomenon on particle trajectories was found be highly significant. The extent of the effect depended on four factors: particle size, particle density, number of particles, and the velocity of the fluid flow.

Chapter 5
CONCLUDING REMARKS

The overarching theme of this thesis is to make use of fluid flow, heat transfer, and particle transport fundamentals to (a) demonstrate the inadequate and erroneous nature of traditional heat-transfer-analysis methodologies, (b) to create new phenomenological-based methodologies to replace those shown to be defunct, (c) to dramatically enlarge the underpinnings, outcomes, and practical utility of the jet-axis switching phenomenon with respect to fluid flow and heat transfer, and (d) to bring together the jet-axis switching phenomenon with particle transport, fluid flow, and heat transfer, taking full account of the numerous and complex interactions that are inherent to multidisciplinary processes. All of the substance developed in this thesis has no antecedents in the published literature. The topical descriptions conveyed in items (a), (b), and (c) correspond respectively to Chapters 2, 3, and 4 of the thesis.

With regard to the ongoing use of erroneous heat transfer methodologies, the major culprit is the flagrant misunderstanding and misuse of the nature of the fluid which underlies the convective heat transfer process. In a major part of the published literature, conveying heat transfer results for virtually all relevant applications, a flow rate or velocity is imposed without any recognition or concern whether that flow rate is consistent with the capabilities of the related fluid-moving device. In the unusual circumstance that the fluid mover is considered and a fan/blower curve is consulted, the information contained in that characteristic curve is misused. This misuse is attributable to the fact that the curve in question does not correspond to the actual output of the fluid mover. The data on which the curve is based is the result of measurements of a flow that is conditioned by screens or perforated plates that are situated downstream of the fluid-mover's exit cross section.

Aside from these fluid-flow-related aberrations, heat transfer analysis methodology very frequently is based on totally unrealistic models. Both of these causes of profound errors are dealt with in Chapter 2.

The scenario adopted in Chapter 2 is to identify two critical applications and evaluate their heat transfer characteristics from two standpoints. One approach is to frame a solution methodology using the best of the traditional but erroneous models. The other approach is to create a model that takes account of all aspects of reality and implements solutions by means of numerical simulation. Particular emphases is placed on the fluid-moving device. As modeled here, the actual moving parts of the fluid mover are taken into strict account, so that the fluid-flow output of the device is totally realistic.

A comparison of the contrasting patterns of fluid flow produced by the unrealistic and the realistic models reveals highly differing outcomes. For example, whereas the simplistic model predicts an outflow of fluid across a comically downstream face of a device, the actual flow direction is an inflow! Not unexpectedly, the heat transfer results are severely compromised by the erroneous fluid-flow field. Of particular note are the size of the errors encountered locally within the investigated heat transfer devices. In fact, the magnitudes of a local heat transfer errors exceed that for the overall rate of heat transfer. For the investigated heat transfer devices, errors in the average rate of heat transfer considerably greater than 50% were encountered.

The jet-axis switching phenomenon has been a happy hunting ground for theoretical fluid mechanitions with minutia issues dominating. No relationship to engineering can be found in the published literature. Here, the focus is engineering and is totally different from anything found in the literature.

The first engineering involvement of jet-axis switching is set forth in Chapter 3. In that chapter, that phenomenon is integrated with engineering fluid mechanics and heat transfer. Whereas the theoretical literature was limited to jet-axis switching in free space, attention was given here to impinging jets and to the concomitant heat transfer. It is well established that jet impingement is the most powerful convective heat transfer modality. Since jet-axis switching is an inevitable natural process for all non-circular jets, it is a highly relevant

practical phenomenon. The heat transfer coefficients determined here are the first that were obtained that take account of the switching process.

The writer attempted to create a baseline case in which jet-axis switching would be suppressed in order to provide a logical comparison of the magnitude of the switching. However, no means was found to suppress the switching process.

Particular focus was given to rectangular jets whose original cross section was of high aspect ratio. As the jet emerged from its creating orifice plate, the entrainment process acted differently on the long and short sides of the jet. The long side of the jet was more retarded while the short side was less so. This differential action caused the short side to actually outrun the long side and thereby caused the evolving change of the jet cross section. If, for example, the long side were initially horizontal, the evolution would create a near-circular cross section which, with further evolution, would morph into a rectangular jet whose long side is vertical. The panorama of this evolving metamorphosis had never before been illustrated because of the preoccupation of previous investigators with minutia.

The heat transfer literature is replete with experimental results for impinging non-circular jets. Despite the extent of that literature, the jet-axis switching process has never before been recognized.

The ascending interest in practical situations where jet-axis-switching fluid mechanics and heat transfer interact with the transport of discrete particles motivated Chapter 4 of this thesis. In a real sense, Chapter 4 is the *pièce de résistance* of the entire work. The participating physical phenomena are the most complex and their interactions more so. There are many interactions to be considered: (a) one-way fluid-particle interactions, (b) two-way fluid-particle interactions, (c) particle-particle interactions, (d) heat transfer responses to fluid flows deformed by fluid-particle interactions, and (e) heat transfer at an impingement surface due to both particle bombardment and fluid wash. Also included

whenever relevant is the effect of gravity since the nominal fluid and particle flow direction is vertically upward.

These phenomena and their interactions were quantified as a function of several dimensionless groups, including Reynolds numbers for the fluid and the particles, the Stokes number which relates to particle size, the Richardson number which gauges the importance of gravity, the Nusselt number which serves to quantify the magnitude of the heat transfer coefficient, the molecular Prandtl number which is the ratio of frictional diffusion to thermal diffusion, and the turbulent Prandtl number which is the same ratio but based on the turbulence mechanism. Other dimensionless parameters were used to characterize various aspect of the geometry. Also included among the independent variables was the number of particles and their density relative to air.

The particle collection efficiency was chosen as a point of interest with regard to parametric variations. In the presence of one-way fluid-particle interactions, the collection efficiency was independent of the number of particles. On the other hand, when two-way interactions were allowed, the particle collection efficiency increased with increasing numbers of particles. The greatest efficiency was attained in the presence of particle-particle interactions.

With regard to heat transfer, it was found that fluid flow alterations due to the presence of particles had an undetectable effect on the overall rate of heat transfer. In sharp contrast, when collisions of the particles and the plate surface were allowed, an enormous increase in the rate of heat transfer was observed.

Of particular interest was a special two-dimensional model of the three-dimensional phenomena and solutions that formed the heart of Chapter 4. The motivation for considering the two-dimensional case was the presence of a limited two-dimensional literature on related but different physical situations relative to that considered here. A two-dimensional model precludes jet-axis switching. In this light, it is to be expected that any

comparison of results between the two-dimensional and three-dimensional models would yield significant differences. The comparison which seemed most apt is the collection efficiency. Such a comparison showed that the two models could not be rationally be compared because their operating ranges were so very different. This outcome dampens any previous or future work based on a two-dimensional model.

Another comparison made in Chapter 4 between the presently employed method and published experiential results for heat transfer and particle collection showed excellent agreement.

Bibliography

[1] Iwasaki, H., and Ishizuka, M., Forced convection air cooling characteristics of plate fins for notebook personal computers. In Thermal and Thermomechanical Phenomena in Electronic Systems, 2000. ITHERM 2000. The Seventh Intersociety Conference on (Vol. 2, 21-26). IEEE.

[2] Famouri, M., Hooman, K., and Hooman, F., Effects of thermal boundary condition, fin size, spacing, tip clearance, and material on pressure drop, heat transfer, and entropy generation optimization for forced convection from a variable-height shrouded fin array. Heat Transfer Research, 40.3 (2009).

[3] Geb, D., and Catton, I., Nonlocal modeling and swarm-based design of heat sinks. Journal of Heat Transfer, 136.1 (2014): 011401.

[4] Zhou, F., DeMoulin, G. W., Geb, D. J., and Catton, I., (2011, January). Modeling of Pin Fin Heat Sinks Based on Volume Averaging Theory. In ASME-JSME-KSME 2011 Joint Fluids Engineering Conference (1357-1365). American Society of Mechanical Engineers.

[5] Kishimoto, T., and Saski, S., Cooling characteristics of diamond-shaped interrupted cooling fin for high-power LSI devices. Electronics Letters, 23.9 (1987): 456-457.

[6] Leon, O., De Mey, G., Dick, E., and Vierendeels, J., Comparison between the standard and staggered layout for cooling fins in forced convection cooling. Journal of Electronic Packaging, 125.3, (2003): 442-446.

[7] Xie, X. L., Tao, W. Q., and He, Y. L., Numerical study of turbulent heat transfer and pressure drop characteristics in a water-cooled minichannel heat sink. Journal of Electronic Packaging, 129.3 (2007): 247-255.

[8] Tan, H. J., and Abdullah, M. Z., Effects of horizontal/vertical fin tip gaps on microchannel heat sinks performance in electronic cooling. Isi Bilimi Ve Teknigi Dergisi-Journal of Thermal Science and Technology, 33.2 (2013): 23-34.

[9] Behnia, M., Copeland, D., and Soodphakdee, D., (1998, May). A comparison of heat sink geometries for laminar forced convection: Numerical simulation of periodically developed flow. In Thermal and Thermomechanical Phenomena in Electronic Systems, 1998. ITHERM'98. The Sixth Intersociety Conference on (310-315). IEEE.

[10] Cole, K. D., Tarawneh, C., and Wilson, B., Analysis of flux-base fins for estimation of heat transfer coefficient. International Journal of Heat and Mass Transfer, 52.1 (2009): 92-99.

[11] Park, K., Choi, D. H., and Lee, K. S., Numerical shape optimization for high performance of a heat sink with pin-fins. Numerical Heat Transfer, Part A: Applications, 46.9 (2004): 909-927.

[12] Agonafer, D., and Free, A., Conjugate Model of a Pin-Fin Heat Sink Using a Hybrid Conductance and CFD Model Within an Integrated MCAE Tool. Thermal Management of Electronic Systems II. Springer Netherlands, (1997): 53-62.

[13] Wirtz, R. A., Sohal, R., and Wang, H., Thermal performance of pin-fin fan-sink assemblies. Journal of Electronic Packaging, 119.1 (1997): 26-31.

[14] Wirtz, R. A., and Zheng, N., (1998, May). Methodology for predicting pin-fin fan-sink performance. In Thermal and Thermomechanical Phenomena in Electronic Systems, 1998. ITHERM'98. The Sixth Intersociety Conference on (303-309). IEEE.

[15] Zheng, N., and Wirtz, R. A., Cylindrical pin-fin fan-sink heat transfer and pressure drop correlations. Components and Packaging Technologies, IEEE Transactions on, 25.1 (2002): 15-22.

[16] Kim, D.-K., Kim, S. J., and Bae, J.-K., Comparison of thermal performances of plate-fin and pin-fin heat sinks subject to an impinging flow. International Journal of Heat and Mass Transfer, 52.15 (2009): 3510-3517.

[17] Ledezma, G., Morega, A. M., and Bejan, A., Optimal spacing between pin fins with impinging flow. Journal of Heat Transfer, 118.3 (1996): 570-577.

[18] Deshmukh, P. A., and Warkhedkar, R. M., Thermal performance of elliptical pin fin heat sink under combined natural and forced convection. Experimental Thermal and Fluid Science, 50 (2013): 61-68.

[19] Lin, S.-C., and Chou, C.-A., Blockage effect of axial-flow fans applied on heat sink assembly. Applied Thermal Engineering, 24.16 (2004): 2375-2389.

[20] Dogruoz, M. B., and Shankaran, G., (2012, November). Advances in Fan Modeling: Issues and Effects on Thermal Design of Electronics. In ASME 2012 International Mechanical Engineering Congress and Exposition (1515-1522). American Society of Mechanical Engineers.

[21] Jian-Hui, Z., and Chun-Xin, Y., Design and simulation of the cpu fan and heat sinks. Components and Packaging Technologies, IEEE Transactions, 31.4 (2008): 890-903.

[22] Liu, M., Liu, G., Joo, I., Song, L., and Wang, G., Development of in situ fan curve measurement for VAV AHU systems. Journal of Solar Energy Engineering, 127.2 (2005): 287-293.

[23] Zhang, L., Jin, Y., and Jin, Y., Effect of tip flange on tip leakage flow of small axial flow fans. Journal of Thermal Science, 23.1 (2014): 45-52.

[24] Menter, F. R., Two-equation eddy-viscosity turbulence models for engineering applications. AIAA Journal, 32 (1994): 1598-1605.

[26] Grinstein, F. F., Self-induced vortex ring dynamics in subsonic rectangular jets. Physics of Fluids, 7.10 (1995): 2519-2521.

[27] Yu, H., and Girimaji, S. S., Lattice Boltzmann equation simulation of rectangular jet (AR= 1.5) instability and axis-switching. Physica A, 362.1 (2006): 151-157.

[28] Yu, H., and Girimaji, S. S., Study of axis-switching and stability of laminar rectangular jets using Lattice Boltzmann method. Computers & Mathematics with Applications, 55.7 (2008): 1611-1619.

[29] Meslem, A., Dia, A., Beghein, C., Ammar, A., Nastase, I., and El Hassan, M., Numerical simulation of free cross-shaped jet. Mechanika, 18.4 (2012): 403-408.

[30] Akbarzadeh, M., Birouk, M., and Sarh, B., Numerical simulation of a turbulent free jet issuing from a rectangular nozzle. Computational Thermal Sciences, 4.1 (2012): 1-22.

[31] Manivannan, P., and Sridhar, B. T. N., Characteristic study of non-circular incompressible free jet. Thermal Science, 17.3 (2013): 787-800.

[32] Tipnis, T. J., Knowles, K., and Bray, D., Statistical modelling for prediction of axis-switching in rectangular jets. Proceedings of the Institution of Mechanical Engineers, Part G: Journal of Aerospace Engineering, 227.8 (2013): 1325-1337.

[33] Chen, N., and Yu, H., Mechanism of axis switching in low aspect-ratio rectangular jets. Computers & Mathematics with Applications, 67.2 (2014): 437-444.

[34] Martin, H., Heat and mass transfer between impinging gas jets and solid surfaces. Advances in Heat Transfer 13, Academic Press, Inc., New York, 1977, 1-60.

[35] Downs, S.J., and James, E.H., Jet impingement heat transfer—a literature survey, In ASME, AIChE, and ANS, 24th National Heat Transfer Conference and Exhibition, Vol. 1. 1987.

[36] Polat, S., Huang, B., Mujumdar, A. S., and Douglas, W. J. M., Numerical flow and heat transfer under impinging jets: a review. Annual Review of Heat Transfer, 2.2 (1989): 157-197.

[37] Jambunathan, K., Lai, E., Moss, M. A., and Button, B. L., A review of heat transfer data for single circular jet impingement. International Journal of Heat and Fluid Flow, 13.2 (1992) 106-115.

[38] Garimella, S.V., Heat transfer and flow fields in confined jet impingement. Annual Review of Heat Transfer, 11.11 (2000): 413-494.

[39] Weigand, B., and Spring, S., Multiple jet impingement− a review. Heat Transfer Research, 42.2 (2011): 101-142.

[40] Abramovich, G. N., On the deformation of the rectangular turbulent jet cross-section. International Journal of Heat and Mass Transfer, 25.12 (1982): 1885-1894.

[41] Hussain, F., and Husain, H. S., Elliptic jets. Part 1. Characteristics of unexcited and excited jets. Journal of Fluid Mechanics, 208 (1989): 257-320.

[42] Sparrow, E. M., Tong, J. C. K., and Abraham, J. P., Fluid flow in a system with separate laminar and turbulent zones. Numerical Heat Transfer, Part A: Applications, 53.4 (2008): 341-353.

[43] Davies, Owen R., et al. Applications of supercritical CO_2 in the fabrication of polymer systems for drug delivery and tissue engineering. Advanced Drug Delivery Reviews, 60.3 (2008): 373-387.

[44] Moussa, A., and Hatem K., A Review of Numerical Investigations Regarding the Supercritical Fluid Expansion in the RESS Process. International Journal of Emerging Multidisciplinary Fluid Sciences, 2.1 (2010): 45-58.

[45] Hatem, K., Comparative Study of Numerical Simulations of the RESS Process: The Supercritical Pure Fluid Expansion. International Journal of Chemical Reactor Engineering, 9.1 (2011).

[46] Huang, C.-H., and Tsai, C.-J., Effect of gravity on particle collection efficiency of inertial impactors. Journal of Aerosol Science, 32.3 (2001): 375-387.

[47] Middha, P., and Wexler, A. S., Design of a slot nanoparticle virtual impactor. Aerosol Science and Technology, 40.10 (2006): 737-743.

[48] Willeke, K., and Mcfeters, J. J., The influence of flow entry and collecting surface on the impaction efficiency of inertial impactors. Journal of Colloid and Interface Science, 53.1 (1975): 121-127.

[49] Mercer, T. T., and Chow, H. Y., Impaction from rectangular jets. Journal of Colloid and Interface Science, 27.1 (1968): 75-83.

[50] Marple, V. A., and Liu, B., Characteristics of laminar jet impactors. Environmental Science & Technology 8.7 (1974): 648-654.

[51] Gardon, R., and Akfirat, J. C., Heat transfer characteristics of impinging two-dimensional air jets. Journal of Heat Transfer, 88.1 (1966): 101-107.

[52] Dogruoz, M. B., Ortega, A., and Westphal, R. V., Measurements of skin friction and heat transfer beneath an impinging slot jet. Experimental Thermal and Fluid Science, 60 (2015): 213-222.

[53] Tu, C. V., and Wood, D. H., Wall pressure and shear stress measurements beneath an impinging jet. Experimental Thermal and Fluid Science, 13 (1996): 364–373.

[54] Guo, Y., and Wood, D. H., Measurements in the vicinity of a stagnation point Experimental Thermal and Fluid Science, 25 (2002): 605–614.

[55] Phares, D. J., Smedley, G. T., and Flagan, R. C., The wall shear stress produced by the normal impingement of a jet on a flat surface. Journal of Fluid Mechanics, 418 (2000): 351–375.

[56] Ortega, A., Westphal, R. V., and Wodrich, J., Skin friction and heat transfer in the impingement region of a slot jet, in: Proc. 7th Int. Symp. Fluid Control, Measurement Visualization, Flucome, Sorrento, Italy, 2003.

[57] Zhou, D. W., and Lee, S.-J., Forced convective heat transfer with impinging rectangular jets. International Journal of Heat and Mass Transfer, 50 (2007): 1916–1926.

[58] Nirmalkumar, M., Katti, V., and Prabhu, S.V., Local heat transfer distribution on a smooth flat plate impinged by a slot jet. International Journal of Heat and Mass Transfer, 54 (2011): 727–738.

[59] Li, X., Gaddis, J. L., and Wang, T., Multiple flow patterns and heat transfer in confined jet impingement. International Journal of Heat and Mass Transfer, 26.5 (2005): 746-754.

[60] Schiller, L. and Naumann, A., VDI Zeits, 77, p. 318, 1933.

[61] Ranz, W. E., and Marshall, W.R. Evaporation from drops. Chemical Engineering Progress, 48 (1952): 141-146.

[62] Sommerfeld, M., Modellierung und numerische Berechnung von partikel beladenen Strömungen mit Hilfe des Euler-Lagrange-Verfahrens, Habilitationsschrift, Shaker Verlag Aachen, 1996.

[63] Sommerfeld, M., Validation of a stochastic Lagrangian modeling approach for inter-particle collision in homogeneous isotropic turbulence. International Journal of Multiphase Flow, 27 (2001): 1829 – 1858.